A STUDY OF THE ELASTIC SCATTERING OF PROTONS BY B^{10}

Thesis by

Jack C. Overley

In Partial Fulfillment of the Requirements

For the Degree of

Doctor of Philosophy

California Institute of Technology

Pasadena, California

1961

ACKNOWLEDGMENTS

The author wishes to express his gratitude to the members of both the professional and technical staffs of the Kellogg Radiation Laboratory for their assistance and cooperation throughout the course of this work. In particular, he would like to thank Professor Ward Whaling for his guidance, aid and advice, and Professor R. F. Christy for several helpful theoretical discussions.

Thanks are also extended to the California Institute of Technology Division of Biology and Division of Engineering and the University of Southern California Chemistry Department for making their facilities available for some aspects of the work reported here.

ABSTRACT

Protons elastically scattered by B^{10} have been studied in the proton energy range from 0.15 to 3.0 Mev. Angular distributions have been measured at 42 energies in this interval and excitation functions have been measured at center of mass scattering angles near 90°, 125°16' and 160°. Subsidiary to these measurements, the atomic stopping cross section of boron for protons in the energy range from 0.10 to 3.0 Mev was determined with an absolute accuracy of 4%. The targets used in these experiments were produced through the thermal decomposition of diborane (B_2H_6).

Theoretical analysis of the angular distributions indicates that for proton energies below 0.90 Mev the scattering can be described by pure s-wave potential scattering processes. There is no indication of anomalous scattering due to the previously reported states in C^{11} at excitation energies of 8.98, 9.13 and 9.28 Mev. Between proton bombarding energies of 0.90 and 1.6 Mev the scattering can be explained qualitatively with a broad $J^{\pi} = 5/2^{+}$ level near 1.15 Mev, a $J^{\pi} = 7/2^{+}$ level near 1.5 Mev, and a negative parity state formed by p-wave protons near 1.36 Mev. Although a definitive analysis was not obtained in this energy region, the two previously reported states in C^{11} at excitations of 9.74 and 10.09 Mev were not sufficient to explain the scattering. Above a bombarding energy of 1.6 Mev the scattering angular distributions are compatible with a $J^{\pi} = 7/2^{-}$ state near 2.06 Mev with $\Gamma_p/\Gamma = 1$, and $\Gamma = 400$ kev, and a $J^{\pi} = 7/2^{+}$ state at some slightly higher energy. The analysis was not extended above 2.5 Mev.

TABLE OF CONTENTS

I. INTRODUCTION

One aspect of low energy nuclear physics which has received considerable attention in the past decade has been the description of energy levels in nuclei. Properties of these levels, such as their decay modes, excitation energies, spins, isotopic spins, and parities, have been investigated in an effort to discover systematic behaviors which might lead to an understanding of nuclear structure and properties of the specifically nuclear force. This study of nuclear systematics has been successful in some respects, resulting in descriptions of several types of collective nucleon motion, as well as descriptions of some of the properties of single nucleon-nucleon interactions. The hypothesis of the charge independence of nuclear forces, for example, is supported in part by the observation of a one-to-one correspondence of states of similar properties in the level structure of mirror nuclei.

The process of describing properties of nuclear states requires a vast amount of experimental and theoretical work, and existing information is quite obviously far from complete. The work reported here is directed toward enhancing and clarifying present information concerning the energy levels of the isotopic spin multiplet with A = 11. In comparison to other light nuclei (A < 20), the amount of information about the states of these nuclei is relatively small. In C^{11} especially, although many states have been found, none have been given conclusive spin and parity assignments, and at excitation energies above the threshold for proton emission some experimental results appear to be contradictory. A brief discussion of some of the experiments on C^{11}

will indicate the nature of these difficulties and contradictions and provide additional justification for this work.

When B^{10} is bombarded by protons in the energy range from 0.15 to 3.00 Mev, states in the compound nucleus C^{11} can be formed at excitation energies from 8.74 to 11.42 Mev. It is energetically possible for states formed in this manner to decay in any of the following ways:

$$B^{10} + p \rightarrow C^{11*} \rightarrow \begin{cases} C^{11} + \gamma & Q = 8.700 \text{ Mev.} \\ Be^{7} + \alpha_o & Q = 1.147 \text{ Mev.} \\ Be^{7*} + \alpha_1 & Q = 0.716 \text{ Mev.} \\ B^{10} + p \end{cases}$$

Most of the definitive work on C^{11} in this region of excitation has been done through the study of these processes. (1)

From studies of neutron groups from the reaction $B^{10} + d \rightarrow C^{11*} + n$, states in C^{11} near excitation energies of 10 Mev have been identified at excitation energies of 8.97, 9.74, 10.09, and 10.89 Mev. (2-4) If these states were formed by free protons, the corresponding proton bombarding energies would be 0.297, 1.144, 1.529, and 2.409 Mev. In addition, several weak neutron groups have been observed by some investigators which may be due to levels at excitations of 9.13 (2), 9.28 (3), 10,69 (3,4), and 11.26 (3) Mev, corresponding to free proton bombarding energies of 0.473, 0.638, 2.189, and 2.82 Mev. These energy levels are displayed in fig. 1.

The α_o-particle decay leading to the ground state of Be^{7} ($J^{\pi} = 3/2^{-}$) has been extensively studied for incident proton energies

from 50 kev to 1.7 Mev. At low proton energies (from 50 to 800 kev) the α_o yield increases smoothly with energy with no indication of anomalous behavior which might be associated with the states in C^{11} at excitations of 8.97, 9.13, and 9.28 Mev. (5,6)

The level at 9.74 Mev has tentatively been assigned a spin and parity of $3/2^-$. This state has been observed through both the α_o-particle decay (7), and the γ-transition to the ground state of C^{11}. (8) The α_o-particles are resonant at a proton bombarding energy of 1.17 Mev, and the cross section at this energy limits the spin J of the state to values of $J \geq 3/2$. The angular distribution of this α_o-particle group exhibits only a small anisotropy below proton energies of 1.2 Mev, which indicates that the state has possible spin and parity assignments of $7/2^+$, $5/2^+$, $3/2^-$, $5/2^-$, or $7/2^-$. The positive parity possibilities arise through s-wave proton formation of the state (since B^{10} has a ground state spin of 3, even parity), and the $3/2^-$ possibility arises through s-wave α_o-decay of the state. The $5/2^-$ and $7/2^-$ assignments are possible if the state is formed by a $p_{1/2}$ proton.

One criterion for choosing the preferred assignment from these alternatives lies in the necessity of explaining the lack of resonant behavior of the α_1-decay to the first excited state of Be^7($J^\pi = 1/2^-$). Unfortunately, there are no strong selection rules apparent which would make one of these assignments preferable. However, if one considers only the relative penetration factors for the two alpha decays, the $7/2^+$ and $5/2^-$ assignments are the least likely since the penetration factors will inhibit the α_1-particle decay a factor of three relative to the α_o-particle decay. For the $J = 3/2^-$ assignment this inhibition factor is approximately five, for the $J = 5/2^+$ assignment the inhibition is a factor

of sixteen, and for a $7/2^-$ assignment the α_1-particle decay is inhibited by a factor of approximately sixty.

Further limitations on the spin and parity assignment for this state can be derived from studies of the (p,γ) reaction which is resonant at a proton energy of about 1.15 Mev. The partial width for the gamma decay to the ground state of C^{11} is observed to be approximately 10 ev, which is compatible with a magnetic dipole transition. If the ground state of C^{11} is $3/2^-$ consistent with shell model predictions and the stripping pattern of the neutron group leaving C^{11} in its ground state (9), the preferred assignments for the 9.74 Mev level are $3/2^-$ or $5/2^-$.

Although the (p,γ) reaction serves to limit the choices of level parameters for this state, it also poses some problems. The total width of the state obtained from the (p,γ) reaction is near 500 kev, while it is approximately 300 kev from the (p,α_o) reaction. Also, the resonant energy obtained from these two processes is slightly different, 1.135 Mev and 1.17 Mev for the (p,γ) and (p,α_o) reactions respectively. The angular distribution of the ground state gamma radiation at a proton energy of 1.135 Mev is observed to be $W(\theta) = 1 + 0.50 \cos^2 \theta$. If the deexcitation is assumed to consist of a single, pure multipole transition, an assignment of $5/2^-$ is the only one which can explain the large anisotropy. With this assignment however, the gamma anisotropy is inconsistent with the α-particle isotropy.

The importance of these discrepancies cannot be accurately assessed. Most of the conclusions concerning this level have been obtained by assuming that the state is pure and that the energy dependence of the reaction excitation functions can be described by a Breit-Wigner single level formula over at least part of the resonance. The validity

of these assumptions is doubtful since interference effects have been observed in the (p, α_o) angular distributions. In addition, if s-wave or p-wave coulomb barrier penetration effects are removed from the γ yield curve, the resonance characteristics of the gamma decay are nearly eliminated. (fig. 52).

One source of this observed interference may be from the state at an excitation of 10.09 Mev. This state has been studied (7) through the alpha particle decay to both the ground state and first excited state of Be^7. Measurement of the total cross section for alpha decay at the resonant energy of 1.53 Mev implies that the spin of this state is greater than or equal to 5/2. Analysis of the angular distributions in terms of powers of cos θ shows that the coefficients of odd powers of cosθ are sharply peaked at a proton energy of 1.36 Mev. This is construed as an indication that the states at 9.74 and 10.09 Mev are of opposite parity. (7) Detailed theoretical fittings of the data show that the alpha particle angular distributions are inconsistent with assignments of $5/2^+$ and $5/2^-$ for the 9.74 and 10.09 Mev states respectively, leaving as most likely the assignments of $3/2^-$ and $7/2^+$. (7) The value $J^\pi=7/2^+$, arising through s-wave and d-wave proton formation of the state, is consistent with the failure to observe the ground state gamma transition and the roughly equal strengths of the α_o and α_1-decays.

The resonant behavior of the alpha particles and gamma radiation in this energy region appears to be superimposed upon a background which may be due to either of two causes; the existence of a broad unidentified level in C^{11}, or non-resonant effects.

Above proton energies of 1.7 Mev, only the (p, γ) (10) and (p, α, γ) (11) reactions have been studied. The yields of both of these reactions

increase monotonically with energy, but no evidence of resonant behavior has been discerned which might be attributed uniquely to a state at an excitation of 10.69, 10.89, or 11.26 Mev.

Throughout the preceding discussion of the reactions that have been studied, the elastic scattering of protons by B^{10} has not been mentioned. This experiment has been performed (12) in the limited energy range from 600 kev to 1.6 Mev, but the data was sufficient to determine only that anomalous scattering exists at proton energies near 1.5 Mev and perhaps near 1.15 Mev. Such an experiment is frequently capable, however, of yielding more information about the nucleus than the study of other reactions. Protons scattered by the nuclear potential will interfere with protons scattered by the coulomb field of the nucleus. Since the coulomb scattering amplitude is known, it is often possible to determine properties of the nuclear scattering amplitude such as its phase and magnitude. The parities of states can also often be determined by inspection because of the influence of these interference effects.

The investigation of the elastic scattering of protons by B^{10} reported in this paper was initially undertaken at low proton energies in order to clarify the situation concerning the states in C^{11} at excitation energies of 8.97, 9.13, and 9.28 Mev. After completion of this work, since most technical problems had been solved, it was logical to extend the scattering to higher energies to answer the following questions: what nuclear level parameters will adequately describe the states at excitations of 9.74 and 10.09 Mev;

what is the nature of the background underlying the resonant behavior of the reaction products from these states; and what is the nature of the previously reported levels at excitations of 10.69, 10.89, and 11.26 Mev?

II. EQUIPMENT

1. Description

Two electrostatic accelerators were utilized in this experiment. A 700 kv generator was used to accelerate protons in the energy range from 150 to 650 kev, and a 3.1 Mv generator was used in the energy range from 600 kev to 3.0 Mev. The description and operation of these two machines and their ancillary equipment are similar; the main difference between them is in their physical dimensions. Since they have been described in detail elsewhere (13, 14) their operation will be discussed only briefly here.

A hydrogen ion beam, containing H^+, HH^+, and HHH^+ ions was produced by an r-f ion source in the high voltage terminal of the machine. After acceleration, this beam was separated into its various mass components by a magnetic field perpendicular to the direction of motion of the beam, and the desired component selected by removing the other components with a slit system. (In this experiment only the H^+ component was used.) The resultant beam was then deflected through ninety degrees by an electrostatic analyzer. Slits at both the entrance and exit of the analyzer defined the particle orbit in such a way as to select a portion of the beam which was homogeneous in energy to the order of 0.1%. Fine regulation of the machine voltage was obtained by utilizing a feed-back system controlled by an error signal from the slits at the exit of the analyzer. Physical parameters which were used for each of the two electrostatic analyzers are displayed in Table I.

At the beginning of each experimental counting cycle, a solenoid

TABLE I. ANALYZING EQUIPMENT

Electrostatic Analyzers		
Properties	Energy range 150 to 660 kev	Energy range 600 kev to 3.0 Mev
Radius of curvature of particle orbit	30-1/4"	42-7/16"
Entrance slit separation	1/16"	1/16"
Exit slit separation (beam spot size)	1/32" x 1/32"	1/16" x 1/16"
Energy resolution $\frac{R}{\Delta R} \cong \frac{E}{\Delta E}$	5×10^2	7×10^2
Magnetic Spectrometers		
Radius of curvature of particle orbit	8"	16"
Exit slit separation	1/32"	1/16"
Solid angle	6×10^{-3} sterad.	6×10^{-3} sterad.
Momentum resolution $\frac{p}{\Delta p}$	8×10^2	10^3
Range of angles	$14.5^\circ \rightarrow 165.5^\circ$	$0^\circ \rightarrow 154^\circ$
Scattering geometry	Incident beam horizontal, scattered beam 15° below horizontal	Incident and scattered beam horizontal

operated beam shutter was opened and the analyzed beam allowed to enter the target chamber and strike the target. The amount of charge incident on the target was integrated by allowing the beam to charge a condenser to a predetermined voltage. When this voltage was attained, a trigger circuit was activated, the beam intercepted by the shutter, and the counting cycle ended.

When the beam strikes any surface, secondary electron emission will occur which can affect the accuracy of the beam current integration. These effects were minimized in two ways. An electron suppressor electrode, biased at 300 volts negative with respect to ground potential, was situated at the entrance to the target chamber to prevent electrons from the beam defining slits from reaching the target. The target itself was biased 300 volts positive to prevent secondary electrons from leaving it.

Both target chambers were equipped with liquid nitrogen cold traps to reduce the condensation of diffusion pump oil on the surface of the target. At low bombarding energies, where this surface contamination can be particularly serious, the target was heated electrically to further minimize these effects.

The reaction products, in this case elastically scattered protons, were analyzed by a high resolution, double focusing magnetic spectrometer. The resolution of this device was a variable which was determined by the size of an aperture in a slit system at the exit of the spectrometer (Table I).

After the scattered protons passed the slits at the exit of the spectrometer, they impinged upon a 0.010 inch thick, cesium iodide

(thallium activated) scintillation crystal, mounted directly on a Dumont 6291 photomultiplier tube. The resultant pulses were amplified by the usual preamplifier, amplifier arrangement and counted by a decade scaler which was turned on and off respectively at the beginning and end of the counting cycle by a signal from the beam current integrator.

2. Electrostatic Analyzer Calibrations

For a given geometry, the energy of the particles which traverse the electrostatic analyzer is proportional to the voltage between the plates of the analyzer. This voltage was determined indirectly by measuring a constant small fraction of the potential difference between the plates with a precision potentiometer. The relation between the potentiometer reading R, and the particle energy E_{10} is: (12)

$$E_{10} \tilde{=} C_e R\left(1 + \frac{E_{10}}{2M_1 c^2}\right) \qquad (1)$$

The factor C_e is a geometry dependent proportionality constant, and $M_1 c^2$ is the rest mass of the particle expressed in energy units. The second term in this expression is a relativistic correction which attained a maximum value of 0.15% in this experiment.

The constant C_e was determined by recording the potentiometer reading at which the particles (protons in this case) initiated a nuclear reaction which occurs, or is strongly resonant, at a well known energy. In the energy range between 100 kev and 650 kev, the calibration was performed by observing the gamma radiation from the reaction $F^{19}(p, \alpha\gamma)O^{16}$ which is resonant at 340.5 kev (15). The targets used

were aluminum fluoride, made by holding an aluminum foil over the mouth of a hydrofluoric acid bottle for several seconds. At 340 kev, the fluoride layer in these targets had an energy thickness of the same order of magnitude as the width of the resonance. It was necessary, therefore, to correct the observed γ-yield for the effects of target thickness before the potentiometer reading corresponding to the resonant energy could be determined. This was done by assuming that the observed resonance width was a simple sum of the target thickness and the actual width of the state, and that the state could be described by a Breit-Wigner single level formula.

At higher energies, from 650 kev to 3.0 Mev, the calibration was based on the $Al^{27}(p, \gamma)Si^{28}$ resonance at 992.4 kev (15), and the $Li^{7}(p, n)Be^{7}$ threshold at 1.8812 Mev (15). The targets were thick evaporated layers of aluminum and lithium, respectively.

3. Magnetic Spectrometer Calibrations

The momentum of the particles accepted by the magnetic spectrometer is a function of the magnetic field over the particle orbit. An average value of this field was measured by a fluxmeter, delicately suspended on jeweled bearings, which consisted primarily of a coil of wire wound on a non-magnetic form and a mechanical counter-weight. The coil was positioned near the particle orbit within the vacuum chamber of the spectrometer. A current was passed through this coil and adjusted until the torque produced by the interaction between the magnetic moment of the coil and the magnetic field was balanced by the restoring torque produced by the counter-weight. The current required

for the balanced condition was precisely measured by a potentiometer, in units of the voltage produced by the current in passing through a standard resistor. In terms of this current I, the energy E_{20} of the particles accepted by the spectrometer is given by the relation (12):

$$E_{20} \simeq \frac{C_m}{I^2} \left(1 - \frac{E_{20}}{2M_1c^2}\right) \qquad (2)$$

The proportionality constant C_m can be determined if a source of particles of known energy is available.

The calibration for these experiments was effected by studying the energy distribution of protons elastically scattered at a given angle from targets of known composition, utilizing the previously calibrated electrostatic analyzer as the energy scale. These distributions were investigated in two different ways, depending on which accelerator was being used. On the 700 kv generator, the spectrometer acceptance energy was held fixed and the scattered proton yield measured for variable incident proton energy, while on the 3.0 Mv generator, the incident energy was fixed and the spectrometer energy varied. These two methods are equivalent, the different procedures being dictated by the relative ease of changing the spectrometer field and electrostatic analyzer voltage. Examples of the resultant energy distributions, or target profiles, obtained by scattering protons from evaporated copper targets are shown in fig. 2.

The spectrometer calibration was obtained from these profiles in the following way. The protons scattered at an angle θ_L with respect to the incident beam from a nucleus of mass M_o have an energy

E_2 given by:

$$E_2 = \alpha E_1 \tag{3}$$

where E_1 is the proton energy immediately before scattering. α is determined from the kinematics of the scattering to be:

$$\alpha = \left| \frac{M_1 \cos \theta_L}{M_o + M_1} \pm \frac{(M_o^2 - M_1^2 \sin^2 \theta_L)^{1/2}}{M_o + M_1} \right|^2 \tag{4}$$

where M_1 is the proton mass. If the protons are scattered from the front surface of the target, so that they do not lose energy in traversing any target material, the energy E_1, in equation 3, becomes the energy E_{10} which is determined by the electrostatic analyzer, and E_2 becomes the spectrometer acceptance energy E_{20}. In a profile of the type shown in fig. 2, the fluxmeter current corresponding to the midpoint of the step in the yield curve represents the spectrometer energy E_{20}. By combining equations 2 and 3, the calibration constant can be determined.

These calibrations were performed throughout the data taking process by scattering protons from freshly evaporated copper targets and from the carbon which appeared as a surface contamination on the boron targets. A summary of the spectrometer calibration constant obtained over a wide range of energies and scattering angles is given in Table II. This table illustrates the consistency of the calibration constant for both the electrostatic analyzer and spectrometer as a function of energy and angle.

TABLE II. SPECTROMETER CALIBRATION CONSTANT

Target used	Scattering Angle θ in degrees	Incident Energy E_{10} in Mev	Fluxmeter Setting I in volts	Calibration Constant C_m in Mev-v^2
Copper	74°27'	1.100	0.6821	0.5008
	94°18'	1.100	0.6856	0.5013
	104°26'	1.100	0.6877	0.5008
	114°46'	1.100	0.6896	0.5011
	120°18'	2.500	0.4574	0.5001
	125°20'	1.100	0.6915	0.5008
	136°3'	1.100	0.6929	0.5007
	146°54'	1.100	0.6945	0.5004
	153°57'	1.301	0.6388	0.5007
Mean of 9 points $C_m = 0.5008 \pm 0.0002$				
Carbon	84°15'	0.600	0.9827	0.4989
	55°17'	1.100	0.6980	0.4994
	64°49'	1.100	0.7065	0.4994
	74°27'	1.100	0.7159	0.4994
	94°18'	1.100	0.7367	0.4995
	104°26'	1.100	0.7476	0.4995
	114°46'	1.100	0.7584	0.4997
	125°20'	1.100	0.7685	0.4996
	136°3'	1.100	0.7773	0.4992
	146°54'	1.100	0.7867	0.5013
	153°57'	1.301	0.7268	0.5011
	120°18'	2.500	0.5063	0.4996
	153°57'	3.000	0.4775	0.4995
	120°18'	3.000	0.4623	0.5001
Mean of 17 such points $C_m = 0.4997 \pm 0.0003$				

It will be noticed that the values of the constant C_m depend slightly on whether copper or carbon was used in the calibration. When copper was used, the step in the profile may have been shifted to slightly lower energies because of the buildup of a surface contamination of diffusion pump oil. This effect would tend to increase the measured value of the fluxmeter constant. When the carbon contamination peak was used in the calibration, this source of error was eliminated. It was difficult, however, to determine which point on the carbon peak corresponded to the energy E_{20} (fig. 3). If the carbon layer were infinitely thin, for example, the peak of the scattering yield would be used instead of the midpoint of the rise. Since the midpoint in the rise was used, an error was introduced which would tend to make the calibration constant too small.

The spectrometer calibration depends on the accuracy with which the scattering angle θ is measured, and will be especially sensitive to the scattering angle if a light target nucleus is used in the calibration. The scattering angle was calibrated in the same way for both magnetic spectrometers. Protons scattered by a target of high atomic number (e. g. tantalum) were required to pass through a small aperture before entering the spectrometer. The aperture consisted of a small hole, with a diameter of 0.060 inches, located in a tantalum mask. The mask was mounted on an arm two inches long so that it could be moved in a circle about the axis of rotation of the spectrometer. The angular position of the aperture with respect to some reference point was measured by a protractor. The reference point was obtained by adjusting

the height and angular position of the hole so that the incoming beam passed through the hole. This process determined the zero and 180 degree scattering directions. The mask was then rotated to cover the magnet entrance aperture, the target placed in position, and protons scattered through the hole were counted as a function of the angular position and height of the hole. In this way a series of profiles of the magnet apertures were obtained.

Since the magnet aperture covers a range of several degrees, the profiles were corrected for such effects as the angular dependence of the scattering cross section. These corrections are discussed more fully in the Appendix. From the corrected profiles, the mean effective scattering angle for this work was approximated by using the geometric center of the magnet aperture.

The results of this measurement are shown in fig. 4. These profiles have been presented in the form of an isometric projection, where the contour drawing represents lines of constant counting or collecting efficiency.

III. TARGETS

1. Target Requirements

Targets suitable for the experiments reported here should satisfy several requirements. Perhaps the most important of these is that the targets must be stable under bombardment. When struck by proton beams with intensities of the order of one micro-ampere per square millimeter and energies up to 3.0 Mev, the targets should not deteriorate in either composition or thickness.

Of nearly equal importance is the purity of the targets. Impurities may introduce errors in the determination of the stopping cross section which must be used in computing the elastic scattering cross section. Furthermore, contaminations of elements heavier than the element of interest are particularly undesirable since the elastic scattering yield from the light element may be masked by scattering from the heavier elements. Although the effects of these contaminations can be minimized if their relative concentrations are known, the accuracy of any measurements will be impaired. It is desirable, therefore, to keep contaminations as low as possible.

Additional properties are desirable for the experimental determination of the stopping cross section. The target should exist in a well defined layer, either as a layer on some sort of backing material, or in the form of a self supporting foil. Means should also exist for conveniently controlling the thickness of this layer.

It was necessary to develop a method of making boron targets which satisfied these requirements, since standard techniques failed in

one respect or another. Evaporated targets were found to be impure, either because of impurities in the boron used or because of the introduction of impurities due to the high temperatures required in the evaporation. Electromagnetically separated targets, which were produced by bombarding a backing with a boron ion beam, were unsuitable since the boron layer was not well defined. Layers of pressed amorphous boron were also tested and found unsatisfactory because the behavior of the layer under bombardment was unpredictable and because it was difficult to control the target thickness. The method which was found to be far superior to other types of target preparation was the deposition of boron through the thermal decomposition of diborane.

2. Properties of Diborane

Diborane (B_2H_6) is a compound which exists as an extremely reactive gas at standard conditions of temperature and pressure and which has a melting point of -162°C. and a boiling point of -92°C. Crude thermodynamic calculations (16) indicate that the gas should decompose into hydrogen, boron and boron hydrides at a temperature of about 230°C., and that the efficiency of the conversion of diborane into elemental hydrogen and boron is a strong function of pressure and temperature.

Because diborane is reactive, any gas handling system must be clean, moisture free, and air tight. The gas is toxic in such small quantities that odor is not an adequate detector. In addition to this danger, mixtures of oxygen and diborane can be explosive. The mixture can easily be ignited at room temperature and the combustion is spontaneous at temperatures of 40° to 50°C. Diborane, as well as other boron

hydrides, hydrolyze completely and rapidly.

Most of the previous methods of depositing boron layers by thermal decomposition of diborane have been continuous flow methods where a pressure controlled stream of gas is passed around a temperature controlled surface. (16-19) Through analyses of the residual gases and through chemical analyses of the boron layer, the efficiency of the cracking process as a function of temperature and pressure, and the purity of the boron deposits have been studied. Such experiments indicate that the spontaneous decomposition rate at room temperature and a pressure of one atmosphere is of the order of 10% per year with the decomposition products being elemental hydrogen and boron, tetraborane (B_4H_{10}), pentaborane (B_5H_9 and B_5H_{11}), decaborane ($B_{10}H_{14}$), and some nonvolatile hydrides (BH_x). At temperatures of about 150°C. the only volatile hydrides which appear are pentaborane and decaborane and the relative amounts of nonvolatile hydrides are increased. At 500°C. only the nonvolatile hydrides occur and these decay to elemental boron and hydrogen at temperatures above 700°C.

The efficiency of the cracking process is a function of pressure, but at pressures below the order of several centimeters of mercury and at temperatures above 700°C. the efficiency is close to 100%. For example, analysis of the results of depositing boron on quartz heated to 800°C. indicated that the process was 91% efficient and the deposit 100% pure.(16)

The results of these experiments indicate that the optimum temperature for the decomposition lies between 700°C. and 1000°C. If the

temperatures are too low, the boron deposits may contain contaminations of boron hydrides. When these deposits are exposed to air, the hydrides will hydrolyze and the deposit will subsequently flake from the deposition surface. If the temperatures are too high, several secondary changes are likely to occur: 1) the amorphous deposit tends to become crystalline, 2) the boron coating tends to diffuse into the backing material, and 3) borides of the backing may be formed.

3. Target Preparation

The method adopted for the preparation of boron targets differed slightly from the deposition methods reported in the literature. The apparatus used is shown schematically in fig. 5.

The diborane was produced by the Chemistry Department at the University of Southern California* from a complex, $CaF_2 \cdot BF_3$, which was obtained from the Oak Ridge National Laboratory. The boron content of the complex had been enriched to 96% B^{10}, and spectroscopic analysis of the boron indicated only traces of elements other than boron. The gas was stored in the pyrex containers (fig. 5) which had a volume of 50 cc. and was kept under refrigeration when not in use in order to retard spontaneous decomposition.

The decomposition was performed in a pyrex cylinder which was designed to contain the deposition surface. The target blank which served as the deposition surface was supported by a quartz tube and was

---

*Through the cooperation of Professor A. B. Burg and Mr. James Boone of the University of Southern California.

held away from the pyrex walls of the decomposition chamber by another quartz tube which surrounded the target blank and support tube. The target blank was heated inductively by placing the cracking chamber in the heating coil of an r-f spark-gap converter. The temperature of the target blank could be controlled by adjusting the power output and tuning of the converter.

A mercury manometer was used to measure the pressure of the diborane allowed in the cracking chamber, and also to determine the residual hydrogen pressure after the cracking process. Once the residual hydrogen pressure had been calibrated in terms of target thickness, this measurement provided a convenient means of controlling the target thickness.

Because of the activeness of diborane, care should be exercised in the choice of lubricants and vacuum sealing compounds for the stopcocks and demountable joints in the apparatus (fig. 5). Silicone vacuum grease, for example, was chemically attacked by the diborane, while "Apiezon T" stopcock grease was found satisfactory.

After investigating several substances, tungsten was selected as the material for target blanks. Tungsten discs 3/4 inches in diameter and 0.010 inches thick were mounted on brass blocks with black wax (plasticene) and were ground flat with successively finer grades of abrasives terminating with 600 grade emery paper. After this preliminary grinding, the discs were polished with 0-10 micron diamond dust by the Caltech Mettalurgy Department.* A high polish was required since

*With the cooperation and aid of Professor F. S. Buffington and Dr. Ronald Willens.

it has been demonstrated that reduced scattering yields can be obtained from rough or scratched surfaces. (20)

After they were polished, the blanks were thoroughly cleaned using alcohol, hot concentrated nitric acid and finally hot concentrated potassium hydroxide. When the final cleaning step was omitted, the boron layer deposited on the tungsten was found to flake off when the target was bombarded. Presumably the existence of a thin oxide layer on the tungsten adversely affects adherence of the layer to the tungsten.

Because the tungsten blanks were only 10 mils thick they were heated nonuniformly by the induction furnace. Since this uneven heating would result in boron layers of nonuniform thickness, the blanks were placed on copper slugs 1/16" thick and 3/4" in diameter. The tungsten was then heated more uniformly since the heating took place through conduction as well as induction. The increased heat capacity of the system due to the addition of the copper slug also enabled one to control the temperature more easily.

The actual deposition process consisted of the following steps which could be repeated to produce targets with thicknesses up to at least 1 milligram per square centimeter.

1. The apparatus was evacuated, and the diborane frozen by placing liquid nitrogen around the diborane container.

2. The target blank was heated to approximately 800°C., as measured by an optical pyrometer, in order to outgas the blank.

3. The cracking apparatus was then closed off from the vacuum

pumps and the stopcock to the diborane container was opened.

4. The liquid nitrogen was removed and the diborane allowed to evaporate and enter the cracking chamber where it decomposed on the hot target blank.

5. When the total pressure reached a value of 2-3 cm. of mercury, the liquid nitrogen was again placed around the diborane bottle and the diborane which had not decomposed was recondensed into the bottle.

6. The residual hydrogen pressure was noted and the system opened to the vacuum pumps to remove the hydrogen.

7. With the system still open to the vacuum pumps the blank was reheated to drive off any hydrogen which might have been in the deposit in the form of nonvolatile hydrides which might have formed because of the increase in pressure and decrease in temperature which occurred during the decomposition process.

8. This process was repeated to obtain a target of sufficient thickness as measured by the residual hydrogen pressure.

9. Upon completion of these steps, the blank was reheated and allowed to cool slowly by gradually reducing the power output of the induction heater. This annealing process improved the stability of the target under bombardment.

A profile of a typical target obtained through this thermal decomposition process is shown in fig. 3. The peaks of carbon, oxygen, and silicon were due to surface contaminations of diffusion pump oil which were deposited on the target during bombardment. The only un-

certainty in the purity of these targets was the hydrogen contamination which could not be conveniently measured through the study of target profiles. It is felt that this contamination was small (<1%) for several reasons. There was little or no deterioration of the targets when exposed to air for considerable lengths of time which indicated that very little hydrolysis of boron hydrides occurred. Boron hydrides react violently with nitric acid but these targets were stable when subjected to this treatment. Also, the small hydrogen contamination (<1%) in the boron deposits reported in the literature, which were made under essentially the same conditions of temperature and pressure as the targets used here, is an additional indication of the smallness of the contaminations in these targets.

IV. STOPPING CROSS SECTION MEASUREMENT

1. Introduction

Previous work on the reactions initiated when boron is bombarded by protons has been seriously hampered by the lack of measurements of the stopping cross section of boron for protons. It has been necessary to estimate this quantity from the known values of the stopping cross section of carbon and berylium. For this reason, since suitable targets had been prepared, the stopping cross section was measured in conjunction with this work.

The atomic stopping cross section ϵ is defined in terms of the differential energy loss dE experienced by a particle passing through a layer of the substance of interest as:

$$\epsilon = -\frac{1}{N}\frac{dE}{dx} \tag{5}$$

where N is the number of stopping atoms per unit volume and dx is the thickness of the stopping layer.

The rationale for the type of experiment employed here can be understood from the definition of the stopping cross section. Since stopping layers of finite thickness were utilized, equation 5 must be integrated. If this is done and the mean value theorem applied, one obtains:

$$\Delta E = \int dE = -\int N\epsilon\, dx = -N\Delta x\epsilon(E_x) \tag{6}$$

Since the number of stopping atoms per square centimeter of target $N\Delta x$ is a constant for a given stopping layer, the energy loss ΔE is proportional to the stopping cross section if the stopping cross section

is taken at some energy E_x between the energy of the particles incident on the target and the energy of the particles emergent from the stopping layer. The energy E_x can be computed from the incident and emergent particle energies if the energy dependence of the stopping cross section can be estimated in the limited energy interval between the incident and emergent energies. From this estimate the energy dependence of the stopping cross section can be ascertained for any large energy range without knowledge of specific properties of the stopping layer.

2. Relative Measurement

In this experiment a layer of boron was deposited on a tungsten blank. Profiles of the target were obtained at a series of energies between 100 kev and 3.0 Mev by observing protons scattered at backward angles. Since the elastic scattering cross section for tungsten is large compared to that for boron, it was possible from these profiles to determine the energy of the protons which had passed through the boron layer, had been scattered from the tungsten, and had passed again through the boron layer before emerging. By comparing this energy to the energy of protons scattered from a tungsten target with no surface layer, the energy loss ΔE could be determined. Examples of these profiles are shown in fig. 6.

The expression for the energy E_x was obtained by assuming that the stopping cross section varies linearly with the energy in the interval between the incident energy and the energy of the protons emerging from the boron layer. (21) Since the target profiles were measured in different

ways depending on which accelerator was being used, it was convenient to express E_x in terms of a different set of variables for each case. On the 700 kv generator, where the spectrometer energy E_{20} was held constant and the incident energy varied, it was desirable to express E_x in terms of the incident energy E_{10}:

$$E_x \cong \frac{E_{10} + E'_{10}}{1 + a} + \frac{E'_{10} - E_{10}}{2(1 + a)} \frac{(\eta - a)}{(\eta + a)} \qquad (7)$$

where $\eta = \frac{\cos \theta_1}{\cos \theta_2} \frac{\epsilon(E_{20})}{\epsilon(E_{10})}$; $a = \frac{E_2}{E_1}$ (for tungsten, eq. 4). In this expression E_{10} and E'_{10} are the electrostatic analyzer energies required for protons scattered from the tungsten in the bare tungsten and boron coated tungsten targets respectively, to enter the spectrometer with the same energy E_{20}. θ_1 and θ_2 are the angles between the incident and scattered beams, respectively, and the normal to the target surface. Since the second term in equation 7 had a maximum value of only 1% of the first term, the values of η were approximated by using the known values of the stopping cross section of carbon for protons.

On the 3.0 Mv generator the incident energy was held fixed and the spectrometer acceptance energy varied. For these conditions:

$$E_x \cong \frac{E_{20} + E'_{20}}{1 + a} + \frac{E_{20} - E'_{20}}{2(1 + a)} \frac{(\eta - a)}{(\eta + a)}$$

$$\eta = \frac{\cos \theta_1}{\cos \theta_2} \frac{\epsilon(E'_{20})}{\epsilon(E_{10})} \qquad (8)$$

E_{20} is the energy of the protons scattered from the bare tungsten target

and E'_{20} is the energy of the protons emergent from the boron layer, after scattering from the tungsten.

Because the protons must pass through the boron layer twice, and because the protons also lose energy on scattering from the tungsten, an effective thickness of the target must be defined. If the profiles are measured using the techniques of the 3.0 Mv generator, this thickness is given by:

$$\Delta x_{eff} = \frac{\Delta x}{\cos \theta_2} \left[1 + \alpha(W) \frac{\cos \theta_2}{\cos \theta_1} \right] \qquad (9)$$

Equation 6 then remains valid if the quantity $N\Delta x$ is replaced by $N\Delta x_{eff}$.

Effects of surface contaminations and the shift in the step in the target profiles that they would produce are minimized by bombarding both the bare tungsten target and the boron target with the same amount of charge at each energy. Surface contaminations should shift the profiles by nearly the same amount in each case, and the resultant energy thickness should be due to the boron layer alone. To further minimize the effects of the buildup of surface contaminations, target spots were changed frequently. The amounts of surface contaminations and contaminations in the boron targets were investigated by lowering the incident energy to such a point that the protons scattered from these contaminations had less energy than the protons scattered from the boron coated tungsten. In all cases the effects of these contaminations were small enough to be neglected since they contributed less than 1% to the

thickness of the boron layer.

Because target spots were changed frequently, the possibility of error was introduced through nonuniformities in the thickness of the boron layer. Therefore, whenever target spots were changed, adequate precautions were taken to normalize the thicknesses of these spots to the thickness at a given point on the target. The results of these measurements are shown in fig. 7, where different target spots have been normalized to a common target thickness, and the entire curve normalized to absolute values obtained by further experiment.

3. Absolute Measurement

It is possible to make an absolute determination of the stopping cross section with the above method if the number of stopping atoms per square centimeter of target surface is known. This quantity can be determined by weighing a deposit of known area. In terms of this weight W, the area of the deposit A, and its molecular weight M, the stopping cross section can be expressed as:

$$\epsilon(E_x) = (E_{20} - E'_{20}) \frac{MA \cos \theta_2}{WL\left[1 + c(W) \frac{\cos \theta_2}{\cos \theta_1}\right]} \qquad (10)$$

where the energy thickness of the layer, $E_{20} - E'_{20}$, is measured by varying the spectrometer acceptance energy for fixed incident energy. L denotes Avogadro's number, the number of atoms per mole.

The target used for this absolute measurement was again boron deposited on tungsten. The area of the deposit was sharply defined by tightly clamping the target blank in a copper holder which was designed

so that the tungsten was exposed to the diborane only through a carefully reamed hole. This copper holder served the secondary purpose of insuring even heating of the target blank. The hole in the deposit defining device was measured to be 1. 036 cm. in diameter. After a boron layer was deposited with the aid of this assembly, the target was examined under a microscope and found to consist of a sharply defined deposit surrounded by a small halo which was due to boron deposited under the area defining assembly. The diameters of both the main deposit and the halo were measured with a traveling microscope and found to be 1. 0456 $\pm$ 0. 001 cm. for the main deposit, and 1. 0627 $\pm$ 0. 004 cm. for the halo. The halo was quite obviously very thin since interference fringes were visible, and it probably contributed little to the weight of the deposit. The value of the diameter used in computing the area of the deposit was 1. 046 $\pm$ 0. 01 cm.

The weight of the boron deposit was determined with an Oertling optical level micro-balance.* The quoted accuracy of this balance was 0. 5 micrograms with a maximum load of 10 grams. This accuracy was not attained, however, since the balance was situated in a room which was neither temperature nor humidity controlled. This was evident through variations of the order of 10 micrograms in the rest point or zero reading of the balance. Because of these variations, zero point readings were recorded as a function of time and, interspersed with these readings, several weighings of the disc were made. The rest point was then assumed to vary smoothly with time in order to find the rest point at the time the disc was weighed.

*Available through the cooperation of the Biology Department.

The first step in the weighing process was to determine that the weight of the tungsten disc was independent of its thermal history. The disc was placed in its holder and inductively heated in vacuum to approximately 800°C, after which it was weighed. The weight of the disc after this heating was 0.375749 ± 0.000005 grams. The disc was then reheated and reweighed and found to have a weight of 0.375754 ± 0.000005 grams. Since these values agreed to within the estimated error of the measurements boron was deposited on the blank. The weight of the tungsten disc plus the boron deposit was 0.376654 ± 0.000005 grams, indicating that the weight of the boron deposit was 900 ± 7 micrograms.

Since the natural boron was not used in the absolute determination of the stopping cross section it was necessary to compute the molecular weight of the layer. A value of M = 10.05 ± 1% was obtained by assuming that the target was 95.96 ± 0.03% B^{10} and 4.04% ± 0.03% B^{11}, as given by the analysis of the complex from which the diborane and the target were made. The supplier estimates that the systematic error in this analysis was less than 1%.

The results of this absolute determination of the stopping cross section were: $\epsilon = 2.72 \times 10^{-15}$ ev. cm.^{2} at an energy of 1.805 Mev, and $\epsilon = 2.10 \times 10^{-15}$ ev. cm.^{2} at an energy of 2.642 Mev. The energy dependence of the stopping cross section, normalized to these values is shown in fig. 7.

4. Errors

In order for equation 10 to be valid there must be some assurance that the target is of uniform thickness. This was checked by measuring the position of the tungsten step as a function of position of the target.

Profiles were taken by bombarding target spots separated by 1/16" along a diameter of the target. These profiles are indicated in fig. 6. These measurements indicate that along a length of 0.375", the target thickness was uniform to within $\pm$ 2%.

Diffusion of the boron into the tungsten blank will tend to make the stopping cross section too small since it will increase the weight of the disc without adding to the effective thickness of the boron layer. If there is appreciable diffusion, the scattering yield from the tungsten will be reduced because of the increased stopping cross section per tungsten atom. The size of this error was estimated by reconstructing the rise in the profile due to the protons scattered from the tungsten by assuming that the rise would be symmetric about its midpoint if no diffusion were present. The departure of the observed yield from this reconstructed profile was used to estimate the concentration of the boron within the tungsten. This effect was found to contribute an error of less than 1%.

A summary of these and additional errors is given in Table III.

The values obtained here are in reasonable agreement with those obtained by extrapolation by Whaling. (22) At energies above several hundred kilovolts, the stopping cross section can be expressed by: (23, 24)

$$\epsilon = \frac{2\pi z^2 e^4}{E} \frac{M}{m_e} Z \left[\ln \left(\frac{E}{Z} \right) + A \right] \qquad (11)$$

where ze, M, and E are the charge, mass, and energy of the incident particle respectively; Z is the atomic number of the stopping material; and m_e is the mass of the electron. The quantity A depends on the

TABLE III. ERRORS IN STOPPING CROSS SECTION MEASUREMENT

Source of Error	Estimated Effect
Area Determination	± 2%
Weight of Deposit	± 1%
Molecular Weight of Enriched Boron	± 1%
Measurement of Target Thickness	± 2%
Target Uniformity	± 2%
Diffusion Effects	± 1%
Contamination Effects	< 1%
Measurement of θ_1 and θ_2	± 0.3%
Assumption of linearity of ϵ over a limited energy range	< 1%
Total probable error	± 4%

average ionization potential of the stopping material. By plotting the empirical values of A obtained from neighboring nuclei, Whaling extracts a value A = 5.07 for boron. This leads to a value of ϵ = 6.37×10^{-15} ev. cm.^{2} for the stopping cross section of boron for protons at 500 kev compared to a value of $\epsilon = 6.40 \times 10^{-15}$ ev. cm.^{2} at 500 kev obtained from this work.

The values reported here are also in good agreement with unpublished values recently obtained for the stopping cross section for alpha particles in boron at the Physikalisches Institut, Marburg/Lahn, Germany. (25) When these values are converted to atomic stopping cross sections for protons with proton energies between 0.125 kev and 1.0 Mev, they reproduce both the energy dependence and absolute values of the stopping cross section reported here to within 2%.

V. SCATTERING CROSS SECTION MEASUREMENT

1. Experimental Procedure

The differential scattering cross section $d\sigma(E_1)/d\Omega_L$ in the laboratory coordinate system can be determined from the thick target scattering yield N from the expression:

$$\frac{d\sigma(E_1)}{d\Omega_L} = \frac{KN}{E_{20}} \left(\epsilon(E_{10})\alpha + \epsilon(E_{20}) \frac{\cos\theta_1}{\cos\theta_2}\right) \tag{11}$$

where

$$K = \frac{ZeR\varphi}{2CV\Omega_L} \tag{12}$$

The scattering cross section obtained from these equations is the scattering cross section at the reaction energy E_1. In terms of the incident energy E_{10} and the spectrometer acceptance energy E_{20}, E_1 is given by:

$$E_1 = \frac{E_{20}\epsilon(E_{10})\cos\theta_2 + E_{10}\epsilon(E_{20})\cos\theta_1}{\alpha\epsilon(E_{10})\cos\theta_2 + \epsilon(E_{20})\cos\theta_1} \tag{13}$$

In this expression as in equation 11, θ_1 and θ_2 are the angles between the normal to the target surface and the directions of the incident and scattered beams respectively. α is determined by equation 4. The stopping cross sections used in these equations are the stopping cross sections per scattering nucleus. This can be written as:

$$\epsilon(E) = \frac{\sum_i n_i \epsilon_i(E)}{n_j} \tag{14}$$

where the n_i are the number of atoms of type i per unit volume of

target material and the ϵ_i are the atomic stopping cross sections associated with the substance i. n_j is the number of scattering atoms of interest per unit volume. In this experiment, the boron targets were assumed to be 96% B^{10} and 4% B^{11} so that the stopping cross section used was 1.042 times larger than the atomic stopping cross section for protons in boron.

The quantity K (equation 12) contains the number of protons incident on the target, expressed in terms of the charge Ze of the incident particle, the value C of the condenser used in the beam current integrator, and the voltage V across this condenser at which the current integrator ends the counting cycle. R is the momentum resolution $p/\Delta p$ of the magnetic spectrometer and Ω_L is the solid angle subtended by the spectrometer at the target. The reciprocal of the particle detection efficiency is given by φ. Values of φ different from unity can be obtained if, for example, counting rates are sufficiently high that electronic dead time effects are important or if a portion of the detecting crystal is inactive due to surface contaminations. Another contribution to φ arises from the charge exchange process in which a portion of the beam is neutralized by picking up electrons from residual gases in the vacuum system or from the target upon emergence from the target.

The only way in which the quantity K can depend on the type of target material is through the charge exchange ratio contained in φ. However, since the cross section for charge exchange is large (26), it is expected that the charge exchange ratio will be determined primarily by the surface contamination of diffusion pump oil on the target, and thus

be independent of the target material itself. There is some experimental evidence that this is the case (27). K can therefore be determined from equation 11 if a scattering experiment is performed on a scattering substance whose scattering cross section and stopping cross section are known.

The elastic scattering of protons by copper was used for this calibration. It was assumed that the scattering could be described by a pure Rutherford scattering cross section corrected for electron screening effects. The electron screening correction is given by Wenzel (13) as:

$$\frac{d\sigma}{dr} = \left(\frac{d\sigma}{dr}\right)_R \left(1 - \frac{34Z^{7/5}}{E_1}\right) \qquad (15)$$

where Z in this case is the atomic number of copper and E_1 is the proton energy expressed in ev. The results of this calibration at low energies are shown in fig. 8, where values of K are plotted as a function of spectrometer acceptance energy E_{20}. These values are normalized to a value of 1.01 at 400 kev obtained for the charge exchange ratio by Allison and Warshaw (27). For comparison, the energy dependence of the charge exchange ratio given by Allison and Warshaw is also shown. At higher energies, K is expected to be a constant. This was found to be true to within $\pm$ 1% for proton energies from 700 kev to 3.0 Mev.

These copper calibrations were run periodically while determining the scattering yield from B^{10} in order to minimize such effects as long time drifts in the beam current integrator firing voltage V. At all times, counting rates were maintained at such a level that electronic

dead time corrections were less than 1%.

Scattering excitation functions (cross section as a function of energy) were determined by measuring the proton scattering yield at energy intervals of approximately 1% of the incident energy and at three angles. In the energy interval from 150 kev to 650 kev where the 700 kv generator was used these angles were $91^{\circ}26'$, $126^{\circ}8'$ and $162^{\circ}28'$ in the center of mass system. From 600 kev to 3.0 Mev, the angles were 90°, $125^{\circ}16'$ and $160^{\circ}34'$. The two forward angles were chosen to be near the zeros of the first and second Legendre polynomials. Spectrometer settings I (in millivolts), and electrostatic analyzer settings R (in volts), were determined from a thick target momentum profile so that protons with an energy of approximately 1% less than that at the edge of the step were counted. These settings were used to determine the constant k in the expression

$$RI^2 = k\sigma(\theta) \tag{16}$$

From this expression, spectrometer settings could be determined for any electrostatic analyzer setting so that particles would be counted at the same relative point on the thick target profile. It is important that the point selected be neither too close to the edge of the profile nor too far back. If it is too close, reduced yields from the edge of the profile may be obtained, and if it is too far back, reduced yields due to multiple scattering and straggling may occur. Furthermore, if the following point is too far back, equation 11 for the cross section is not accurate since the stopping cross sections $\epsilon(E_{10})$ and $\epsilon(E_{20})$ should be

averaged over the energy interval from E_{10} to E_1 and from $E_2 = \alpha E_1$ to E_{20} respectively. For a following point 1% behind the edge of the step, neglect of this averaging introduced an error of less than 0. 2% in the scattering cross section.

The number of counts measured at the top of the step in the momentum profile (fig. 3), consisted of protons scattered by B^{10}, protons scattered by the B^{11} contamination in the target, α-particles primarily from the $B^{10}(p, \alpha)Be^7$ reactions and noise. In order to eliminate counts due to sources other than protons elastically scattered by B^{10}, an estimate of the background was obtained by setting the electrostatic analyzer and spectrometer to count particles from the top of the small B^{11} step in the target profile. This background was recorded at intervals of approximately 2% of the incident proton energy and assumed to vary smoothly with energy. It was possible to perform this background measurement at all angles except at center of mass scattering angles of 60 and 70 degrees, where the carbon surface contamination peak and the B^{11} step could not be resolved. The difference between the number of counts recorded at the top of the B^{10} step and the background was taken as the proton scattering yield N, to be inserted into equation 11.

Angular distributions (cross section as a function of scattering angle) were determined by measuring excitation functions every 10° in the center of mass system from 60 to 160 degrees. Points on these excitation curves were obtained at energy intervals of 25 to 150 kev, depending on whether the excitation functions showed any fine structure,

or whether energy levels had been previously reported in a particular energy region. Care must be taken in determining spectrometer and electrostatic analyzer settings for angular distributions since the proton scattering yield should be measured at the same reaction energy E_1 at each angle. Conditions can be derived from equation 13 to insure that this will be true. However, since no narrow energy levels were apparent in the excitation functions, this condition was relaxed and the scattering yields were measured at the same set of incident energies E_{10} at each angle. The spectrometer settings were computed from these incident energies using equation 16, where k was taken to be independent of angle and was chosen so that at any angle the yield was measured well behind the front of the step in the profile. The variation in reaction energy in the angular distributions which arose from the use of equation 16 amounted to $\pm$ 0.2% of the incident energy. The reaction energies used to describe the angular distributions were averages over this interval.

In comparing experimental results with theory it is convenient to express the results as a ratio between the observed cross sections and the calculated Rutherford cross sections. This was accomplished by converting the cross section computed from equation 11 to center of mass coordinates by multiplying the cross section by the ratio of the solid angle Ω_L in laboratory coordinates to the solid angle Ω_C in center of mass coordinates. This ratio is given by:

$$\frac{\Omega_L}{\Omega_C} = \frac{(1 - (M_1/M_o)^2 \sin^2\theta_L)^{1/2}}{[(1 - (M_1/M_o)^2 \sin^2\theta_L)^{1/2} + M_1/M_o \cos\theta_L]^2} \qquad (17)$$

for the case of elastic scattering of protons of mass M_1 from nuclei of mass M_o. The scattering angle in laboratory coordinates θ_L is related to the center of mass scattering angle θ_C by:

$$\sin(\theta_C - \theta_L) = \frac{M_1}{M_o} \sin\theta_L \qquad (18)$$

For protons scattered by copper, the expression used for the Rutherford scattering cross section in center of mass coordinates was:

$$\left(\frac{d\sigma}{d\Omega}\right)_R = \frac{1.125 \times 10^{-18} \csc^4(\theta_C/2)}{E_1^2} \text{ cm}^2/\text{ster.} \qquad (19)$$

For protons scattered by boron, the equivalent expression was:

$$\left(\frac{d\sigma}{d\Omega}\right)_R = \frac{3.920 \times 10^{-20} \csc^4(\theta_C/2)}{E_1^2} \text{ cm}^2/\text{ster.} \qquad (20)$$

where the scattering occurs at an energy E_1 expressed in Mev.

The excitation functions obtained using the above techniques are shown in fig. 9. The arrows along the abscissa of this graph indicate the energies at which angular distributions were measured. The angular distributions are shown in figs. 10 through 46.

2. Normalizations

There are several independent normalization procedures which, by comparison, provide a test of the consistency of the experimental results. At very low energies, the observed scattering cross section divided by the Rutherford value should approach unity since the

coulomb barrier will preclude nuclear events. Another normalization is derived naturally by using the absolute values of the stopping cross sections of boron and copper in equation 11.

An additional normalization can be obtained if a compound can be found which contains boron and some other element in definite proportions. A comparison of the scattering yields from the constituents of this compound will give a comparison of the scattering cross sections. This can be seen immediately from the definition of the cross section σ in terms of the thin target yield Y:

$$\sigma = \frac{Y}{n\,dx} \tag{21}$$

Here n is the number of scattering nuclei per unit volume of target material and dx is the target thickness. If the target is a compound of known composition, the number n is known for both constituents and the target thickness is the same for both elements. Thus by measuring the scattering yields from both components, their relative scattering cross sections can be determined.

A satisfactory compound for this method of normalization is B_2O_3. Since the elastic scattering cross section for oxygen is known at 1.250 Mev to within 1% (28), it is possible to obtain a value of the cross section for the elastic scattering of protons from B^{10} at this energy.

The targets were made from boric acid H_3BO_3 which had been enriched in boron content to 93% B^{10}. This compound was placed in a tantalum evaporating boat and heated under vacuum to drive off the water. When boric acid is heated above 500° C, H_3BO_3 and all sub-acids

are decomposed into B_2O_3 (29). Care was therefore taken to heat the sample to greater than 500°C. The boat containing the fused B_2O_3 was then placed in an evaporating furnace contained in the target chamber. Two polished berylium discs were placed in the target holder and the B_2O_3 was evaporated onto one of them. This evaporation process was repeated until a target of the desired thickness was obtained. The optimum thickness was a layer thick enough that it exceeded the resolution of the spectrometer, but thin enough that the protons scattered from the oxygen and boron could be resolved. Profiles of the target obtained are shown in fig. 47. On the same figure is a profile of the bare berylium blank.

The profiles for the bare berylium and the B_2O_3 targets were measured in exactly the same way, and each target was bombarded by the same amount of charge. This was done so that surface contaminations of oxygen and carbon would be the same on both targets. On the berylium target (fig. 48), it is seen that the yields from the oxygen and carbon surface contaminations are roughly the same. On the B_2O_3 target two carbon contaminations are visible, one on the surface of the berylium behind the B_2O_3 layer, and one on the surface of the B_2O_3. The oxygen surface contaminations unfortunately occur within the scattering peak due to the oxygen in the B_2O_3. The effects of the oxygen contamination were subtracted by assuming that they contributed the same yield as the carbon. The positions of the oxygen contamination peaks were determined from the kinematics of the scattering.

The target thickness was such that the protons scattered from the

B^{10} and B^{11} could not be resolved. It was assumed that the shape of the profile due to B^{11} was the same as that due to the B^{10} and that the B^{11} scattering yield was that occurring between the carbon contamination and the B^{10} step. The profile due to the B^{11} was then reconstructed and subtracted from the B^{10} scattering yield.

The scattering yields were obtained from these corrected target profiles by extrapolating the top of the profile to the energy corresponding to the midpoint of the step. This energy was selected as that for which the oxygen scattering cross section was known.

The calculation of the B^{10} scattering cross section from these yields is more complicated than indicated by equation 21. Since the thickness of the target exceeds the resolution of the equipment equation 11 must be used instead. An appropriate expression derived from equation 11 is given by:

$$\frac{(d\sigma_B/d\Omega)}{(d\sigma_O/d\Omega)} = \frac{N_B}{N_O} \frac{E_{20}(B)}{E_{20}(O)} \left(\frac{n_O}{n_{B^{10}}}\right) \frac{1 + \alpha(B^{10})^{\gamma-1}}{1 + \alpha(O)^{\gamma-1}} \qquad (22)$$

This relation is obtained by assuming that the stopping cross section for protons in B_2O_3 can be written as:

$$\epsilon = aE^{\gamma} \quad (a = \text{constant}) \qquad (23)$$

in the energy interval from 1.0 to 1.5 Mev. The exponent $\gamma = -0.246$ was evaluated from a logarithmic plot of the stopping cross section of B_2O_3 obtained from the atomic stopping cross sections of boron and oxygen:

$$\epsilon_{B_2O_3} = 2\epsilon_B + 3\epsilon_O \qquad (24)$$

N_O and N_B are the scattering yields for oxygen and boron respectively. $E_{20}(O)$ and $E_{20}(B)$ are the spectrometer acceptance energies at which the oxygen and boron scattering yields were measured, and $n_B = 2(0.93)$ and $n_O = 3$ are the relative concentrations of oxygen and B^{10} in the target. $d\sigma_O/d\Omega$ is the oxygen elastic proton scattering cross section which was taken as 0.1628 barns/ster. at an energy of 1.250 Mev and a scattering angle in the laboratory of $120^\circ 20'$. (28) From these values, the cross section for the elastic scattering of protons by B^{10} at a bombarding energy of 1.250 Mev and a scattering angle of $125^\circ 16'$ in center of mass coordinates was determined to be $(\frac{d\sigma}{d\Omega})/(\frac{d\sigma}{d\Omega})_R = 2.01$.

The results of these three normalizations appear on the excitation curve (fig. 9) for a scattering angle of $125^\circ 16'$. The data as presented in these curves is normalized to the Rutherford cross section at low energies, where the same normalization factor was used at all angles. Normalized in this way, the curve passes about 2% below the value obtained from the B_2O_3 normalization and about 3% above the values obtained by using the absolute values of the stopping cross section.

3. Errors

The probable errors attached to the experimental points will depend on the type of normalization utilized. For convenience, the errors are divided into two parts, one which depends explicitly on the normalization and one which is independent of the normalization. It is this latter relative error which is shown on the angular distributions. For a discussion of these errors it is convenient to rewrite equation 11 in terms of the quantities actually used in computing the scattering cross sections:

$$\left(\frac{d\sigma}{d\Omega}\right)/\left(\frac{d\sigma}{d\Omega}\right)_R = \frac{\sigma_{Cu}}{\sigma_B}\frac{N_B}{N_{Cu}}\frac{E_{20}(Cu)}{E_{20}(B)}\frac{\left(\epsilon_B(E_{10})\alpha(B)+\epsilon_B(E_{20})\frac{\cos\theta_1}{\cos\theta_2}\right)}{\left(\epsilon_{Cu}(E_{10})\alpha(Cu)+\epsilon_{Cu}(E_{20})\frac{\cos\theta_1}{\cos\theta_2}\right)} \quad (25)$$

In this expression, σ_{Cu} and σ_B are the coulomb scattering cross sections for copper and boron respectively, determined at the reaction energies at which the copper scattering yield N_{Cu}, and the B^{10} scattering yield N_B, were measured. $E_{20}(Cu)$ and $E_{20}(B)$ are the spectrometer energies used in these measurements for copper and boron respectively. Writing the expression in this way is justified because the copper calibration was performed periodically during measurements of the B^{10} scattering yield.

From equation 25 it can be seen that the determination of the B^{10} scattering cross section will not depend strongly on either energy or angle calibrations, since the coulomb scattering cross sections vary in nearly the same way for both boron and copper. A summary of the estimated probable errors due to various sources when the absolute stopping cross sections are utilized are shown in Table V.

When the normalization from the measurements on B_2O_3 is used, the large errors in the absolute determinations of the stopping cross sections are no longer involved since this normalization requires only the energy dependence of the stopping cross sections. Furthermore, contaminations in the target (as long as they are neither boron nor oxygen) and surface irregularities are not important since these effects will not affect the ratio of observed yields from boron and oxygen. The main

uncertainty in this measurement, which cannot be easily estimated, is in the relative concentrations of oxygen and boron in the target due to the possible presence of sub-oxides of boron. The estimated probable errors in this normalization are shown in Table VI.

It should be noted that the effects of systematic errors are probably small since the results on both generators overlap within the estimated relative error of 2% (fig. 9).

TABLE IV. ERRORS (STOPPING CROSS SECTION NORMALIZATION)

Source of Error	Amount
1. Normalization	
A. Copper stopping cross section	± 4%
B. Boron stopping cross section	± 4%
C. Target composition	± 1%
D. Angle calibration	< 1%
2. Relative Error	
A. Errors in copper scattering yield	
1. counting statistics	± 0.3%
2. current integrator reliability	± 0.3%
3. electronic dead time correction	± 1%
4. assumption copper scattering is Rutherford	?
B. Errors in boron scattering yield	
1. counting statistics	± 1%
2. background subtraction ($\theta_c > 70^\circ$) (at 60 and 70 degrees)	± 0.3% (± 4%)
3. current integrator reliability	± 0.3%
C. Errors in energies	
1. neglect of relativistic corrections	± 0.3%
2. determination of E_{20} (relative)	± 0.1%
3. variation of E_1 (angular distributions only)	(± 0.2%)
Estimated relative error ($\theta_c > 70^\circ$) (at 60 and 70 degrees)	± 2% (± 4%)
Total estimated probable error (at 60 and 70 degrees)	± 6% (± 7%)

TABLE V. ERRORS (B_2O_3 NORMALIZATION)

Source of error	Amount
1. Normalization	
A. Oxygen scattering yield	± 1%
B. Boron scattering yield	± 2%
C. Oxygen scattering cross section	± 1%
D. Target composition	?
E. Stopping cross section of B_2O_3	± 1%
2. Relative Errors	
A. Copper scattering yield (see Table IV)	± 1%
B. Boron scattering yield (see Table IV) (at 60 and 70 degrees)	± 1% (± 4%)
C. Errors in energies (see Table IV)	± 0.6%
D. Relative values of boron stopping cross section	± 1%
E. Relative values of copper stopping cross section	± 1%
Total probable error in normalization	± 3%
Total relative error	± 2%
Total estimated probable error	± 4%

VI. THEORY

1. General Discussion

The procedure followed in analyzing the data consists of determining parameters which, when inserted into theoretical expressions, duplicate the energy and angular dependence of the observed scattering cross sections. When such a set of parameters is obtained, which is also consistent with existing reaction data, it is assumed that the events occurring have been adequately described. The formalism which is used here has been described in great detail elsewhere, (20, 30) and therefore will be briefly reiterated here only as is necessary to understand the analysis performed.

The different scattering processes which can occur, such as coulomb scattering, nuclear resonant and non-resonant scattering and spin-flip scattering, are described in terms of scattering amplitudes. These many amplitudes are divided into groups such that amplitudes within a group will interfere coherently while amplitudes in different groups will add incoherently. The division is made on the basis of the channel spin configuration through which the scattering occurs. The channel spin is defined as the vector sum of the spin $\vec{I}$ of the target (or residual) nucleus and the intrinsic spin $\vec{s}$ of the incident (or emergent) particle:

$$\vec{J}_{ch} = \vec{I} + \vec{s} \qquad (26)$$

In the case of elastic scattering of protons by B^{10}, there are two possible channel spins $J_{ch} = 5/2$ and $J_{ch} = 7/2$. The term "channel spin

configuration" refers to the pair of numbers consisting of the channel spin and its z-component, (J_{ch}, m_{ch}). If unpolarized particles are involved, the scattering events which occur through one set of initial and final channel spin configurations will be incoherent with events which occur through a different set of initial and final channel spin configurations.

A convenient method of tabulating the various scattering amplitudes is to construct a matrix, the rows of which are described by the initial channel spin configurations and the columns described by the final channel spin configurations. For protons scattered by B^{10} this will be a 14 x 14 matrix. The elements of this matrix will consist of the sums of coherently interfering scattering amplitudes. The final expression for the scattering cross section will then be the sums of the squares of the matrix elements, divided by the number of initial states of the system, $(2I + 1)(2s + 1)$.

Such a method would appear to be infinitely complex since scattering events can occur for every orbital angular momentum ℓ of the incident particle, each event being described by a characteristic scattering amplitude which must be included in the channel spin matrix. This complexity is reduced to manageable proportions in several ways. Compound nuclear states which are formed must satisfy conditions of conservation of parity and angular momentum:

$$\vec{J}_{ch} + \vec{\ell} = \vec{J} = \vec{J}'_{ch} + \vec{\ell}' \tag{27}$$

$$m_{ch} = M = m'_{ch} + m' \tag{28}$$

where J and M are the angular momentum and z-component of angular momentum of the compound state, and where primed quantities refer to the angular momenta of the residual particles. Equation 28 has utilized the fact that the z-component of angular momentum of a plane wave travelling in the z-direction is zero. In addition to these restrictions, for protons with an energy of less than 2 Mev scattered by B^{10} one would expect only those protons with orbital angular momentum of less than $3\hbar$ to interact appreciably with the target nucleus to form compound states of the system. The probability of forming a compound state is related to the width Γ of the state. This width can be expressed as a product of a penetration factor and a reduced width γ^2 which is a function of nuclear parameters alone:

$$\Gamma = 2P_\ell \gamma^2 = \frac{2kR\gamma^2}{(F_\ell^2+G_\ell^2)_R} \tag{29}$$

where F_ℓ and G_ℓ are the regular and irregular coulomb wave functions respectively, evaluated at the nuclear radius R, and k is the wave number of the incident proton in the center of mass coordinate system. Employing the Wigner single particle limit (31), the reduced width can have a maximum value of the order:

$$\gamma^2 = \frac{3}{2}\,\frac{\hbar^2}{MR^2} \tag{30}$$

where M is the reduced mass of the system. At a bombarding energy of 2 Mev, these expressions place an upper limit of 40 kev on the proton width of the states formed by f-wave ($\ell = 3$) protons. Since no narrow anomalies are observed in the excitation functions, pure f-wave formation

of compound states probably need not be considered in the analysis.

2. Scattering Amplitudes

The scattering amplitude f_c for Rutherford scattering is given by:

$$f_c = \sqrt{R}\, e^{i\xi} \tag{31}$$

where

$$\xi = -\frac{z_o z_1 e^2}{\hbar v} \ln\left(\sin^2 \frac{\theta_c}{2}\right)$$

$z_o e$ and $z_1 e$ are the charges on the target nucleus and incident proton respectively. R is the expression for the Rutherford scattering cross section given by equation 20. This amplitude is a sum over all orbital angular momenta, but since the coherence of the scattering depends only on the channel spin configurations, the various angular momenta need not be considered explicitly. These amplitudes will occur as diagonal entries in the channel spin matrix since off-diagonal terms correspond to spin-flip scattering.

The nuclear scattering amplitude consists of the product of several factors:

$$C_{J_{ch}\ell}(J, M; m_{ch} O) C_{J'_{ch}\ell'}(J, M; m'_{ch}, m'_\ell) Y_{\ell'}^{m'}(\theta, \varphi) f^J_{J_{ch} J'_{ch}, \ell, \ell'} \tag{32}$$

One factor is a Clebsch-Gordan coefficient which describes the probability amplitude for forming a compound state with angular momentum J, z-component M, from a given channel spin configuration (J_{ch}, m_{ch}) and orbital angular momentum ℓ of the incident particle. Another Clebsch-Gordan coefficient gives the probability amplitude for the decay

of this state into a channel spin configuration (J'_{ch}, m'_{ch}) and orbital angular momentum ℓ' of the emergent particle. The angular dependence of the emergent particle is described by the normalized spherical harmonic $Y_{\ell'}^{m'}(\theta, \varphi)$. The final factor contains terms which describe specifically nuclear processes and is given by:

$$f^{J}_{J_{ch}, J'_{ch}, \ell, \ell'} = \frac{\sqrt{4\pi}\, i}{2k}\; i^{(\ell-\ell')}(2\ell+1)^{1/2} e^{i(\eta_\ell + \eta_{\ell'} - 2\eta_o)} f^{J}_{sc} \qquad (33)$$

where

$$\eta_\ell - \eta_o = \sum_{j=1}^{\ell} \tan^{-1}\left(\frac{z_o z_1 e^2}{jhv}\right)$$

The form of the factor f^{J}_{sc} as used here depends on the assumptions concerning the nature of the scattering processes. When only s-wave protons are involved, it is assumed that the processes which can occur are potential scattering, scattering due to the presence of non-resonant reactions, and scattering through a compound state. f^{J}_{sc} may then be written as (for s-waves only):

$$f^{J}_{sc} = f_J + ig_J - 1 = e^{2i\varphi_J}\frac{\Gamma_{pJ}}{\Gamma_J}\left(e^{2i\delta_J} - 1\right) + (1-C)e^{2i\varphi_J} - 1 \qquad (34)$$

In this expression, the quantity φ_J is the potential scattering phase shift, and δ_J is the resonant scattering phase shift for the formation of a state of spin J. Γ_{pJ} is the proton partial width of the state and Γ_J is the total width. C is related to the non-resonant reaction cross section.

For higher angular momentum protons, potential scattering and

non-resonant reactions are assumed to be small. The basis for this assumption is derived from a simple classical picture which states that for particles with angular momentum $\ell\hbar$ to interact with the nucleus, the inequality $kR \geq \ell$ must be satisfied. On this basis, a bombarding energy of more than 1 Mev is required before p-wave ($\ell = 1$) protons can interact appreciably with B^{10} if a nuclear radius of $R = (1.41 \times 10^{-13})(A_o^{1/3} + A_1^{1/3}) = 4.45 \times 10^{-13}$ cm. is assumed. Under the assumption that only compound state formation contributes appreciably to the cross section, the scattering amplitude f_{sc}^J has the same form for both pure elastic scattering and spin-flip scattering:

$$f_{sc}^J = (a_{J, J_{ch}}^{\ell})(a_{J, J_{ch}}^{\ell'}) \frac{(\Gamma_{pJ\ell}\Gamma_{pJ\ell'})^{1/2}}{\Gamma_J} (e^{2i\delta_J} - 1) \qquad (35)$$

The primed quantities in this expression refer to the angular momenta of the particles after scattering. $a_{J, J_{ch}}^{\ell}$ is the nuclear probability amplitude for the formation of a state with spin J from the channel spin J_{ch} and orbital angular momentum ℓ. From its definition, this channel spin mixing ratio must satisfy the condition:

$$(a_{J, 5/2}^{\ell})^2 + (a_{J, 7/2}^{\ell})^2 = 1 \qquad (36)$$

where the channel spins have been inserted for the scattering of protons by B^{10}.

When these amplitudes are inserted in the channel spin matrix, the matrix elements squared, and the sum of these squares divided by $(2I + 1)(2s + 1) = 14$, the following expressions for the cross section are

obtained.

1. Pure s-wave processes

$$\frac{d\sigma/d\Omega}{(d\sigma/d\Omega)_R} - 1 = \left[\frac{\sin\xi}{k\sqrt{R}} - \frac{1}{2k^2R}\right](X-1) - \frac{\cos\xi}{k\sqrt{R}}\,Y - \frac{U}{4k^2R} \qquad (37)$$

where

$$X = \frac{6}{14}f_{5/2} + \frac{8}{14}f_{7/2} = \sum_{J=5/2}^{7/2} \frac{2J+1}{(2I+1)(2s+1)}\left\{\cos 2\varphi_J\left[1 - C_J - \frac{2\Gamma_{pJ}}{\Gamma_J}\sin^2\delta_J\right] - \frac{2\Gamma_{pJ}}{\Gamma_J}\sin 2\varphi_J \sin\delta_J\cos\delta_J\right\}$$

$$Y = \frac{6}{14}g_{5/2} + \frac{8}{14}g_{7/2} = \sum_{J=5/2}^{7/2} \frac{2J+1}{(2I+1)(2s+1)}\left\{\sin 2\varphi_J\left[1 - C_J - \frac{2\Gamma_{pJ}}{\Gamma_J}\sin^2\delta_J\right] + \frac{2\Gamma_{pJ}}{\Gamma_J}\cos 2\varphi_J \sin\delta_J\cos\delta_J\right\}$$

$$U = 1 - \frac{6}{14}(f_{5/2}^2 + g_{5/2}^2) - \frac{8}{14}(f_{7/2}^2 + g_{7/2}^2) = \frac{\sigma_{\text{s-wave reaction}}}{\pi\lambda^2}$$

2. For pure p-wave formation of a state with spin J, plus s-wave background:

$$\frac{d\sigma/d\Omega}{(d\sigma/d\Omega)_R} - 1 = \text{Equation 37} - \frac{2(2J+1)}{14k\sqrt{R}}\,\frac{\Gamma_p}{\Gamma}\cos\theta\left\{A_J\cos\xi + B_J\sin\xi\right\}$$

$$+ \frac{(2J+1)}{14k^2R}\,\frac{\Gamma_p}{\Gamma}\cos\theta\left\{(a^1_{J,\,5/2})^2(A_J g_{5/2} + B_J(1-f_{5/2})) + (a^1_{J,\,7/2})^2(A_J g_{7/2} + B_J(1-f_{7/2}))\right\}$$

$$+ \frac{9}{14k^2R}\left(\frac{\Gamma_p}{\Gamma}\sin\delta^1_J\right)^2\left\{B_J + F_J(a^1_{J,\,7/2})^2\cos^2\theta\right\} \qquad (38)$$

where

$$A_J = \sin \delta_J^1 \cos(2\eta_1 - 2\eta_o + \delta_J^1)$$

$$B_J = \sin \delta_J^1 \sin(2\eta_1 - 2\eta_o + \delta_J^1)$$

$$D_J + F_J(a^1_{J,\,7/2})^2\cos^2\theta = \frac{4\pi}{3} \sum_{m,\,M,\,J_{ch},\,J'_{ch}} (a^1_{J,\,J_{ch}})^2(a^1_{J,\,J'_{ch}})^2$$

$$\times\ |Y_1^m(\theta,\varphi)|^2 |C_{J_{ch},\,1}(J,\,M;M,\,0)C_{J'_{ch},\,1}(J,\,M;M-m,\,m)|$$

Values of D_J and F_J are plotted in fig. 48 as a function of the channel spin mixing parameter for values of J which can be formed by p-wave protons. Equation 38 assumes that there is no overlapping of p-wave states, and equation 37 assumes that s-wave states of equal spin do not overlap. Because of the great complexity which occurs with the introduction of p-wave amplitudes, higher angular momenta amplitudes, which would further increase the complexity, were not considered.

3. Energy Dependence of the Scattering Amplitudes

The scattering parameters determined through the use of equation 37 or 38 must exhibit a reasonable energy dependence. This dependence may perhaps be best investigated by considering the influence of various types of scattering on the quantities f_J and g_J as defined by equation 34. When interpreted as points in the (f_J, g_J) plane, the values of f_J and g_J will describe a curve which must lie wholly within the unit circle $f_J^2 + g_J^2 = 1$. If only potential scattering is present, the points determined by f_J and g_J will move around the unit circle in a clockwise direction

as the energy is increased. This is easily seen by the reduction of equation 34 to:

$$f_J + ig_J = e^{2i\varphi_J} \tag{39}$$

where the potential scattering phase shift φ_J is a negative quantity which decreases monotonically with energy. Arguments using causality, which state essentially that the proton cannot be scattered before it reaches the scattering center, limit the energy variation of the phase shift to values such that: (32)

$$-\frac{d\varphi_J}{dk} < R \tag{40}$$

where R is the interaction radius. This is a hard sphere approximation and should be interpreted only as a crude limit on the phase shift.

If, in addition to pure potential scattering, non-resonant reactions are included, the points determined by f_J and g_J will still describe a clockwise rotation, but with a radius of curvature given by $(1 - C)$.

If only resonant scattering is present, equation 34 reduces to:

$$f_J + ig_J = \frac{\Gamma_{pJ}}{\Gamma_J}\left(e^{2i\delta_J} - 1\right) + 1 \tag{41}$$

where the resonant phase shift is defined in terms of the resonant energy E_r as:

$$\cot \delta_J = \frac{(E_R - E)}{\frac{1}{2}\Gamma_J} \tag{42}$$

As δ_J varies through 180°, equation 41 describes a counterclockwise

circle, tangent to the unit circle, with a radius given by $\frac{\Gamma_{pJ}}{\Gamma_J}$.

In general, all of these effects will be present, and the point (f_J, g_J) will trace out a complicated figure consisting of a superposition of the above rotations. Another departure from idealized behavior may occur for broad levels since the radius of the resonant circle may not be constant due to the energy variation of the quantity $\frac{\Gamma_{pJ}}{\Gamma}$.

In the actual analysis, the quantities X, Y, and U are determined. These parameters are functions of four s-wave amplitudes, $f_{5/2}$, $g_{5/2}$, and $f_{7/2}$, $g_{7/2}$, which cannot be uniquely determined unless interference with particles of higher angular momenta is present. Since the s-wave amplitudes may behave differently, the energy dependence of X, Y, and U may be complicated. In spite of these difficulties, some conclusion as to the validity of the fitting parameters may be obtained from the following conditions on X, Y, and U.

1. X, Y, and U must satisfy the conditions:

$$-1 \leq X \leq 1; \quad -1 \leq Y \leq 1; \quad 0 \leq U \leq 1; \quad X^2+Y^2 \leq 1-U \qquad (43)$$

2. If no resonances are present, the points (X, Y) in the (X, Y) plane should describe a clockwise rotation.

3. If a resonance is present, the points (X, Y) should describe a crude counterclockwise rotation with a radius of curvature given by:

$$\frac{2J+1}{(2I+1)(2s+1)} \frac{\Gamma_{pJ}}{\Gamma_J} \qquad (44)$$

4. Analysis Procedure

If only s-wave processes are occurring, there is a graphical

method of determining the scattering parameters. The expression for the scattering cross section is a function of three variables, X, Y and U. Since the detailed fitting of the angular distributions is insensitive to the values of U, U may be estimated from the measured reaction cross section. Using these values of U, and the measured scattering cross sections in equation 37, there results a set of linear relations for each angular distribution involving only X and Y as unknowns. These equations, one for each angle, can be considered as defining a set of straight lines in the X, Y plane. The best intersection of these lines will then determine the best values of X and Y. An example of this method of solution is shown in fig. 49, where the short transverse lines indicate the errors in the experimental determination of the scattering cross section.

If the values of X and Y obtained in this way exhibit unreasonable energy dependence, or violate the conditions in equation 43, or if the circle of confusion of the intersecting lines is incompatible with the experimental errors, it must be assumed that the pure s-wave analysis is not valid. Scattering processes of greater complexity must then be considered. The only additional processes considered here consisted of the inclusion of p-wave resonant states. Values of the p-wave resonant scattering parameters such as the spin J of the compound state, the resonant energy E_r, the proton partial width, and the total width of the state were assumed. When possible, these values were chosen to be consistent with estimated parameters obtained from experiments on the reactions which occur. These assumed values were introduced into

equation 38, and a graphical analysis employed to determine the s-wave scattering parameters. The p-wave scattering parameters were then adjusted to make the s-wave parameters exhibit reasonable behavior.

VII. RESULTS

1. Proton Bombarding Energy $E_p < 0.9$ Mev

For proton energies of less than 900 kev, the excitation curves (fig. 9) are smoothly varying functions of energy with no indications of anomalous scattering which might be attributed to the previously reported states in C^{11} at excitation energies of 8.97, 9.13, or 9.28 Mev. Analysis of the angular distributions in this energy region (figs. 10-13) indicate that the scattering can be explained by pure s-wave potential scattering. If it is assumed that only potential scattering is occurring and that the potential scattering phase shift is the same in both scattering channels, the phase shift may be determined from the parameters X and Y from the relation:

$$\varphi = \frac{1}{2} \tan^{-1} \frac{Y}{X} \qquad (45)$$

Values of the potential scattering phase shift obtained in this way are shown in fig. 50. The energy variation of this phase shift is compatible with the causality condition expressed by equation 40.

From the excitation functions and angular distributions in this energy region, it can be concluded that if the previously reported states do not interfere with nearby states, their total widths must be of the order of 1 kev or less, or that the partial proton widths are less than 2% of the total widths.

2. Proton Bombarding Energy, $0.9 < E_p < 1.3$ Mev

Between incident proton energies of 0.9 Mev and 1.3 Mev, the effects of the previously reported state in C^{11} at an excitation energy of

9.74 Mev should be observed in the scattering. Since there exists conflicting evidence for the spin and parity assignments of this state, several hypotheses were employed in the analysis.

If it is assumed that this state is formed solely by s-wave protons, the theoretical cross sections can be made to duplicate the experimental scattering angular distributions very well (figs. 14-21). The s-wave scattering parameters X and Y, exhibit reasonable behavior and suggest the presence of a resonance (fig. 51). The most attractive assignment for this level is then $J^{\pi} = 5/2^{+}$, consistent with the $B^{10}(p, \alpha_o)Be^7$ angular distributions (7). From the values of X and Y, the ratio of the proton partial width to the total width is $\Gamma_p/\Gamma = 0.2$. This value is only accurate to a factor of two, but compares favorably with a ratio of $\Gamma_p/\Gamma = 0.15$ obtained from the $B^{10}(p, \alpha_o)Be^7$ excitation functions by assuming that the cross section at resonance can be described by a Breit-Wigner single level formula. It was not possible to obtain accurate values of the resonant energy or total width of this state from the scattering parameters.

There are some difficulties with the $J = 5/2^{+}$ assignment, however. 1) The $B^{10}(p, \gamma)C^{11}$ angular distributions must be explained. 2) Below a bombarding energy of 1.140 Mev, the values of X and Y are such that $X^2 + Y^2 = 1 - U$ which implies that the s-wave scattering amplitudes are the same in each scattering channel. The latter difficulty can be remedied if smaller values of the s-wave reaction cross section are used than those given in the $B^{10}(p, \alpha_o)Be^7$ work (7). These smaller values would suggest that the measured (p, α) cross sections contain contributions from other than s-wave processes which is an additional indication that more than pure s-wave scattering events are occurring.

Because of these difficulties, the angular distributions were analyzed by assuming the presence of a p-wave $3/2^-$ or $5/2^-$ state. From the interpretations of the $B^{10}(p,\gamma)C^{11}$ and $B^{10}(p,\alpha)Be^7$ reaction data, the following possibilities for values of the p-wave resonance parameters were obtained

E_r	Γ_p/Γ	Γ	$(a^1_{5/2,7/2})^2$
1.15 Mev	0.25	300 kev	0.6
1.17 Mev	0.75	500 kev	
1.20 Mev			

With any combination of these values, the theoretical cross sections can again be made to duplicate the experimental scattering angular distributions. However, the s-wave scattering amplitudes $f_{5/2}$, $g_{5/2}$, $f_{7/2}$, and $g_{7/2}$ behave in an unreasonable manner. At energies above 1.2 Mev, the condition $f^2_{7/2} + g^2_{7/2} \leq 1$ is violated. In addition, the s-wave scattering amplitudes in the 5/2 channel are still undergoing resonant behavior, and the strength of this s-wave resonance as measured by the quantity Γ_p/Γ increases with increasing values of the ratio Γ_p/Γ for the p-wave state. If both p-wave and s-wave resonances exist at this energy, it is difficult to explain the angular distributions of both the $B^{10}(p,\gamma)C^{11}$ and $B^{10}(p,\alpha_o)Be^7$ reaction products.

Since the level structure in C^{11} is not simplified by the assumption of a p-wave resonance in this energy region, the $J = 5/2^+$ assignment for the state is to be preferred.

3. Proton Bombarding Energy $1.3 < E_p < 1.5$ Mev .

Because the pure s-wave analysis breaks down at energies above 1.29 Mev, it is necessary to assume that events of greater complexity are occurring in this energy region. In addition, if it is assumed that the states at 1.15 and 1.53 Mev are both formed by s-wave protons, it is also necessary to find a reason for the peaking of the odd powers of cos θ at a bombarding energy of 1.36 Mev in the angular distributions of alpha particles from the reaction $B^{10}(p, a_o)Be^7$. One possible solution is the introduction of a p-wave state near 1.36 Mev. Using an intermediate coupling model, Kurath (33) predicts the existence of five normal (negative) parity states in C^{11} between excitation energies of 8.0 and 12.0 Mev with angular momentum values $J = 1/2, 3/2, 5/2, 7/2, 9/2$. Because of these many possibilities and the number of variable parameters associated with them, it was not possible to obtain a definitive analysis of the data. However, assuming a $J^{\pi} = 3/2^-$ state at a proton bombarding energy of 1.36 Mev, with a total width of 200 kev and a ratio $\Gamma_p/\Gamma = 0.8$, the analysis could be satisfactorily extended to an energy of 1.49 Mev. (figs. 24, 25). The primary conclusion that can be drawn from the analysis is that the scattering angular distributions cannot be explained with the assumption of only one state near 1.15 Mev. Either more states must be added, or some background other than s-wave considered.

4. Proton Bombarding Energies $1.5 < E_p < 1.9$ Mev

Since the elastic scattering shows an anomaly near 1.5 Mev at all angles, it is attractive to retain the hypothesis derived from the $B^{10}(p, a)Be^7$ experiment that this is a positive parity state with $J = 7/2$

formed by s-wave and d-wave protons. A pure s-wave scattering analysis is not sufficient to explain the observed scattering angular distributions. Inclusion of d-wave scattering parameters for the formation of the state is probably necessary since the alpha particle angular distributions indicate a d-wave partial proton width of about 18% of the s-wave width. Because of the necessity of introducing higher than s-wave angular momentum protons it was not possible to draw quantitative conclusions concerning the resonant parameters of the state. Qualitatively, the s-wave analysis indicates that the scattering parameters are undergoing resonant behavior and that the ratio Γ_p/Γ is large, not in disagreement with a value of $\Gamma_p/\Gamma = 0.64$ obtained from the alpha particle excitation functions.

5. Proton Bombarding Energy $E_p > 1.9$ Mev

At an energy of approximately 2.1 Mev there is an anomaly which is large at backward scattering angles and which disappears at 90°. This indicates that the state is formed by p-wave protons. Because of the size of the cross section at the peak of the anomaly, the spin of the state can be limited to values of $J > 5/2$. This leaves possible J values of 7/2 and 9/2, either of which is possible according to the theoretical predictions of Kurath. From detailed fitting at the peak of the anomaly, if only s-wave background is considered, it was found that a $J^\pi = 7/2^-$ assignment produces the best agreement with experiment. The best values of the p-wave fitting parameters were found to be: $E_r = 2.060$ Mev, $\Gamma = 400$ kev, and $\Gamma_p/\Gamma = 1$, with formation of the state occurring entirely through the 7/2 channel (i.e. $a^1_{7/2,\,7/2} = 1$). This state may thus

correspond to the previously reported state at an excitation of 10.69 Mev, although this would indicate an error of roughly 100 kev in resonant energy.

Using the above values of the p-wave resonant parameters, reasonable fits to the angular distributions can be obtained for an energy interval of 100 kev either side of the peak in the excitation curve (figs. 32-38). If the analysis is extended over a wider energy range, the s-wave scattering parameters again behave unreasonably. This may be due to non-s-wave background which will contribute relatively more to the cross section where the yield due to the p-wave state is small.

If the analysis of the state at 2.060 Mev is valid, the s-wave amplitudes indicate the presence of an s-wave $J^{\pi} = 7/2^{+}$ level at some higher energy. This may be due to the previously reported level at an excitation of 10.89 Mev. Because the analysis cannot be extended over a wide energy interval, and because the s-wave scattering amplitudes cannot be determined accurately near 2.1 Mev where a major portion of the cross section is due to the p-wave state, it was not possible to obtain values for the resonant parameters of this state.

At bombarding proton energies above 2.3 Mev it was not possible to analyze the angular distributions with only s-wave scattering. Because little is known about the nature of the states in this energy region, greater complexity in the analysis was not considered.

6. Conclusions

Before definitive results can be obtained from the analysis of the

scattering data, more experiments on the proton induced reactions will have to be performed in order to eliminate some of the possibilities for spin and parity assignments for states in C^{11}. Of primary importance is a more complete measurement of the ground state gamma angular distributions at energies from 0.90 Mev to 1.5 Mev. A search for a cos θ dependence should be made in this energy interval and if found, this dependence should be determined as a function of energy. The possibility of determining the existence of p-wave states in this region, namely at 1.15 Mev and 1.36 Mev and determining possible assignments for these states should be enhanced through this experiment.

Another experiment of great interest would be the continuation of the $B^{10}(p, \alpha)Be^{7}$ excitation functions to higher energies to look for a possible alpha decay from the state at 2.060 Mev. If such a transition is observed, it should be possible to choose between the $J = 7/2$ and $J = 9/2$ assignments, since if the state is $J^{\pi} = 7/2^{-}$ the decay will proceed through d-wave alpha particles, whereas if the assignment is $9/2^{-}$, g-wave decay is required.

With or without these additional experiments it will be necessary to perform a more comprehensive analysis of the scattering, considering the possibilities of p-wave potential scattering and d-wave resonant scattering. Because of the additional complexity introduced with these assumptions, it will probably be necessary to perform these computations on an electronic computer before definitive results can be obtained.

APPENDIX
SPECTROMETER ANGLE CALIBRATION

We shall consider a special case of scattering geometry where the incident beam lies in a horizontal plane. The angle θ_L that the scattered beam makes with respect to the incident beam direction can be defined in terms of the projection ϕ of the scattering angle in the horizontal plane and the angle ψ that the scattered beam makes with the horizontal plane. As a function of ϕ and ψ, the scattering angle is given by:

$$\cos\theta_L = \cos\phi \cos\psi \qquad (1A)$$

For the conversion of reaction yield measurements into cross section it is necessary to know the angle θ_1 between the incident beam and the normal to the target surface and the angle θ_2 between the scattered beam and the target normal. In particular, it is convenient to derive a condition such that θ_1 equals θ_2. This condition can be expressed in terms of ϕ and ψ as:

$$\cos^2\theta_1 = \cos^2\theta_2 = \frac{\sin^2\phi \cos^2\psi}{1 + 2\cos\phi\cos\psi + \cos^2\psi} \qquad (2A)$$

Methods of determining ϕ and ψ are mentioned in the text. The scattered beam is required to pass through a small circular aperture whose position is known relative to the direction of the incident beam. This position is measured in terms of the angle ϕ and the height h of the aperture relative to the incident beam. The scattering yields N measured through this aperture should be corrected for the effects con-

sidered below.

1. Variation of the Solid Angle Subtended by the Aperture at the Target

Because the height of the aperture is varied, the solid angle subtended by the aperture at the target varies due to changes in the effective area of the opening as seen from the target and changes in the distance from the aperture to the target. The effective area A_{eff} of the opening is given by:

$$A_{eff} = \pi a^2 \cos\psi = \frac{\pi a^2 r}{(r^2+h^2)^{1/2}} \qquad (3A)$$

where r is the horizontal distance from the aperture to the target and a is the diameter of the aperture. The solid angle subtended by the opening at the target is

$$\Omega = \frac{\pi a^2 r}{(r^2+h^2)^{3/2}} \qquad (4A)$$

If all other factors are equal, the scattering yield will be proportional to this solid angle. The variation in yield due to variations in solid angle is obtained by differentiation with respect to h and is given by:

$$\frac{\Delta\Omega}{\Omega} = \frac{\Delta N}{N} = \frac{-3h\Delta h}{r^2+h^2} \qquad (5A)$$

For the 8" spectrometer this effect contributed a correction of approximately 5% in scattering yield.

2. Variation of Scattering Yield Due to the Angular Dependence of the Scattering Cross Section

The expression for the thick target yield can be obtained from equation 11 as:

$$N = \frac{E_{20}}{K} \frac{d\sigma/d\Omega}{(\epsilon E_{10})a + \epsilon(E_{20}) \frac{\cos \theta_1}{\cos \theta_2})} \tag{6A}$$

By differentiating this expression with respect to θ_L, the correction to the scattering yield can be obtained. If a heavy target nucleus is used for these measurements, several approximations can be made to facilitate the evaluation of this derivative. The scattering cross section can be assumed to exhibit an angular dependence given by the Rutherford cross section

$$\frac{d\sigma}{d\Omega} \propto \csc^4 \frac{\theta_c}{2} \tag{7A}$$

In addition, the following approximations are valid:

1. $\theta_c = \theta_L$ (8A)

2. $\epsilon(E_{10}) = \epsilon(E_{20}) = \text{constant}$ (9A)

3. $a = 1; \ \partial a/\partial\theta_L << 1$ (10A)

If the calibration is carried out near a scattering angle of ninety degrees and θ_1 is taken approximately equal to θ_2, these further approximations are valid:

1. $\theta_1 = \theta_2 = 45^\circ$ (11A)

2. $d/d\theta_2 = - d/d\theta_L$ (12A)

For the calibration of the 8" spectrometer, the target orientation was held fixed relative to the incident beam direction and θ_1 was therefore a constant. When these approximations are employed, the logarithmic derivative of N becomes:

$$\frac{\Delta N}{N} = -2 \cot \frac{\theta_L}{2} + \frac{1}{2} \qquad (13A)$$

After these corrections have been made, the particle collection efficiency as a function of position on the magnet entrance aperture is obtained. The geometric center of the entrance aperture was taken as determining the mean angles ϕ_o and ψ_o which were used to calculate the scattering angle given by equation 1A. The accuracy placed on this calibration was $\pm 1/2^{\circ}$.

REFERENCES

1. F. Ajzenberg-Selove and T. Lauritsen, Nuclear Physics 11, 105-111 (1959).
2. V. R. Johnson, Phys. Rev. 86, 302 (1952).
3. M. Cerineo, Nuclear Physics 2, 113 (1956).
4. A. Graue and B. Trumpy, Phil. Mag. 2, 138 (1957).
5. G. G. Bach and D. J. Livesy, Phil. Mag. 46, 824 (1955).
6. W. E. Burcham and J. M. Freeman, Phil. Mag. 41, 921 (1950).
7. J. W. Cronin, Phys. Rev. 101, 298 (1956).
8. Chadwick, Alexander, and Warren, Canadian J. Phys. 34, 381 (1956).
9. Maslin, Calvert, and Jaffe, Proc. Phys. Soc. 69, 754 (1956).
10. R. B. Day and T. Huus, Phys. Rev. 95, 1003 (1954).
11. Hunt, Pope, and Evans, Phys. Rev. 106, 1012 (1957).
12. Brown, Snyder, Fowler, and Lauritsen, Phys. Rev. 82, 159 (1951).
13. W. A. Wenzel, Ph. D. Thesis, California Institute of Technology (1952).
14. C. W. Li, Ph. D. Thesis, California Institute of Technology (1951).
15. R. O. Bondelid and C. A. Kennedy, Phys. Rev. 115, 1601 (1959).
16. Schlesinger, Schaeffer, and Barbaras, U. S. A. E. C. Report MDDC 1338 (1944).
17. Schlesinger, Schaeffer, Barbaras, and Wartik, U. S. A. E. C. Report MDDC 1339 (1944).
18. Schlesinger, Schaeffer, Barbaras, and Farr, U.S. A. E. C. Report MDDC 1340 (1944).
19. R. W. Dodson and H. Russel, U. S. A. E. C. Report MDDC 384 (1944).

20. F. Moser, Ph. D. Thesis, California Institute of Technology (1956).

21. W. D. Warters, Ph. D. Thesis, California Institute of Technology (1953).

22. W. Whaling, Handbuch der Physik, 34, 193 (1958).

23. M. S. Livingston and H. Bethe, Revs. Mod. Phys. 9, 245 (1937).

24. F. Bloch, Zeit. F. Physik 81, 363 (1933).

25. D. Kamke and P. Kramer, Private Communication.

26. J. A. Phillips, Phys. Rev. 97, 404 (1955).

27. S. K. Allison and S. D. Warshaw, Revs. Mod. Phys. 25, 779 (1953).

28. F. J. Eppling, M. I. T. Laboratory for Nuclear Science Annual Progress Report, 88 (June 1, 1954-May 31, 1955).

29. Gmelin, Handbuch der Anorganischen Chemie; Bor, 13, 138, Verlag Chemie, Weinheim/Bergstrasse (1954).

30. R. F. Christy, Physica 22, 1009 (1956).

31. T. Teichman and E. P. Wigner, Phys. Rev. 87, 123 (1952).

32. E. P. Wigner, Phys. Rev. 98, 145 (1955).

33. D. Kurath, Phys. Rev. 101, 216 (1956).

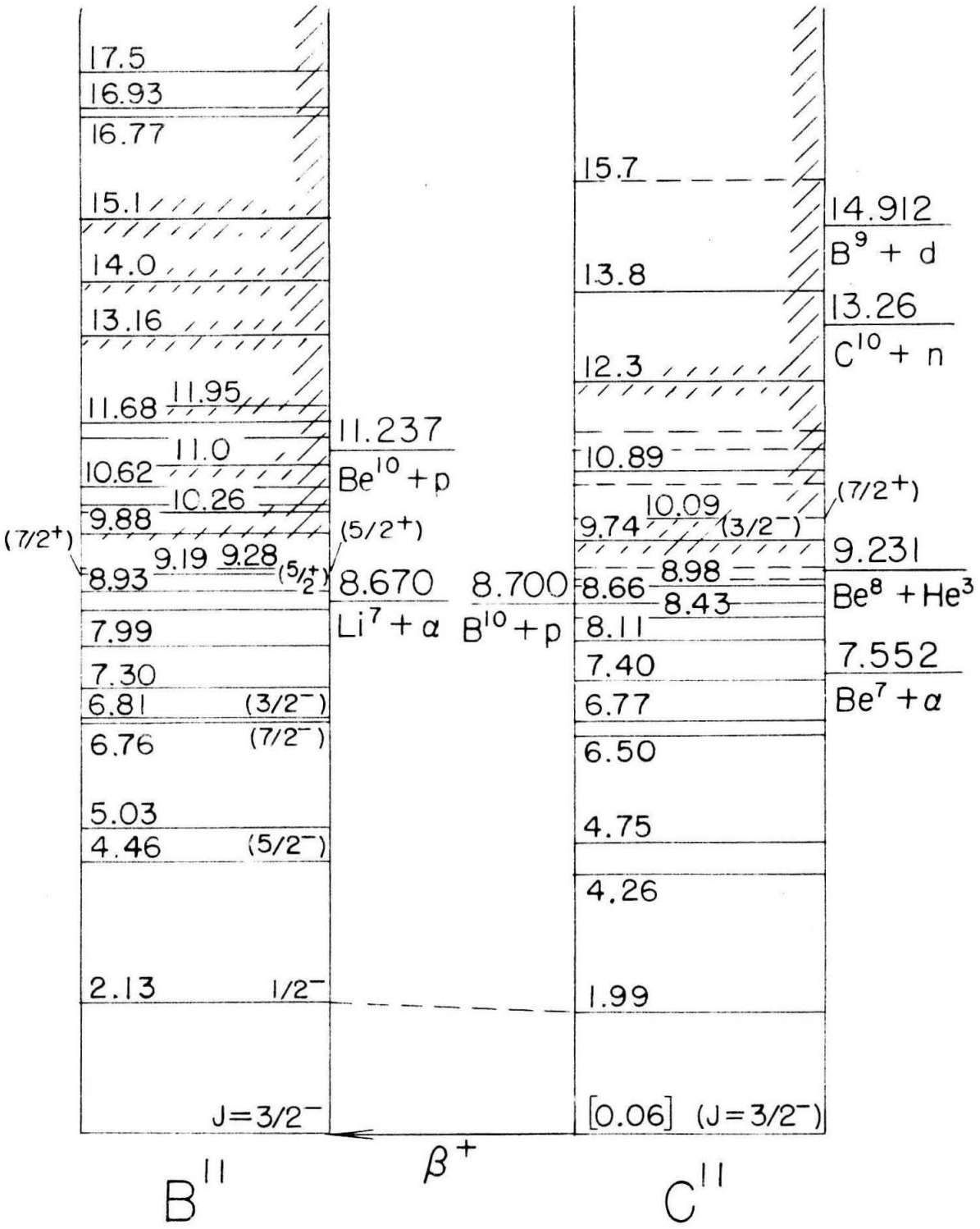

NUCLEAR ENERGY LEVELS B^{11}, C^{11}

FIGURE 1

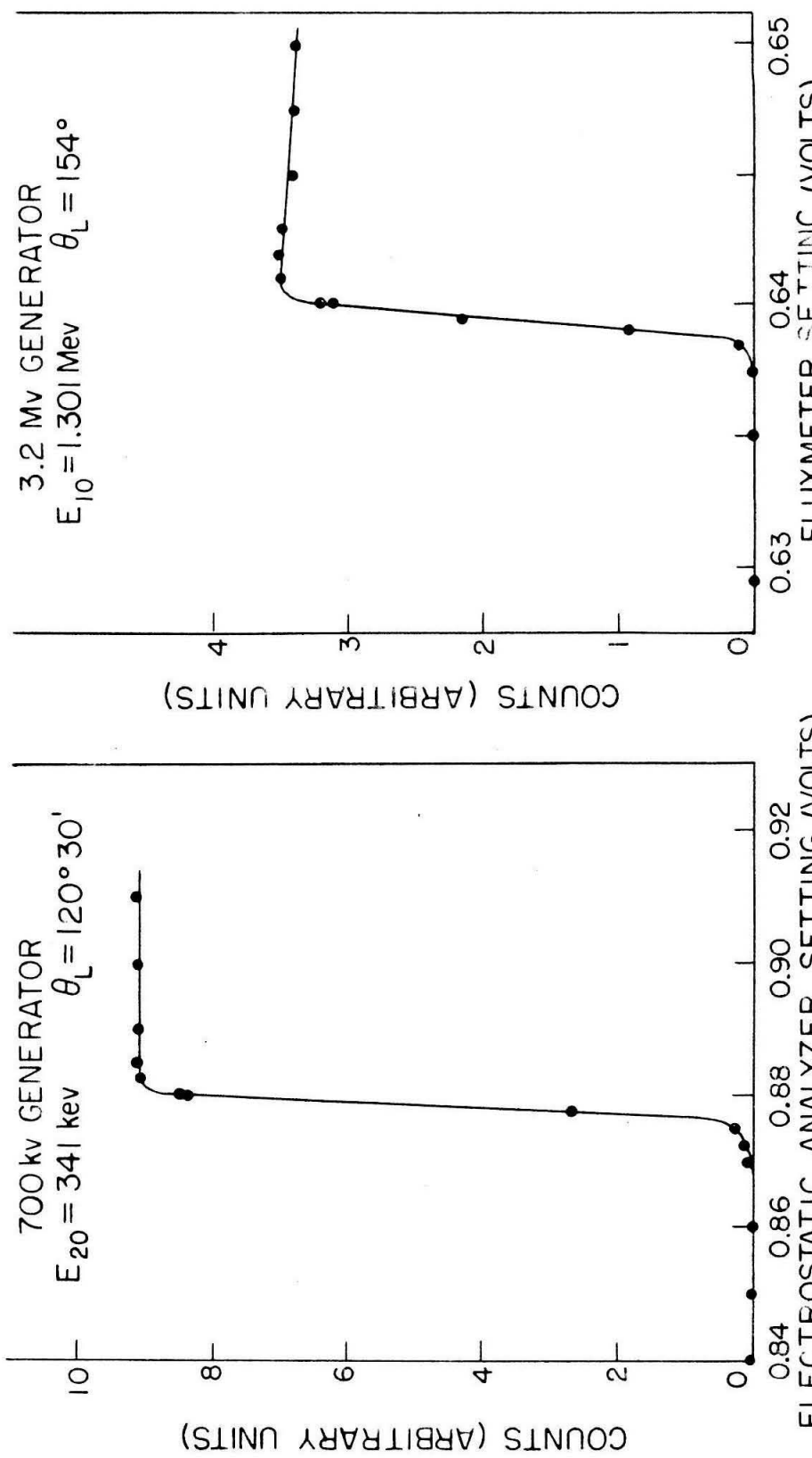
TARGET PROFILES
PROTONS ELASTICALLY SCATTERED BY COPPER
700 kv GENERATOR
E_{20} = 341 kev
θ_L = 120° 30'
COUNTS (ARBITRARY UNITS)
0
2
4
6
8
10
0.84
0.86
0.88
0.90
0.92
ELECTROSTATIC ANALYZER SETTING (VOLTS)
3.2 Mv GENERATOR
E_{10} = 1.301 Mev
θ_L = 154°
COUNTS (ARBITRARY UNITS)
0
1
2
3
4
0.63
0.64
0.65
FLUXMETER SETTING (VOLTS)

FIGURE 2

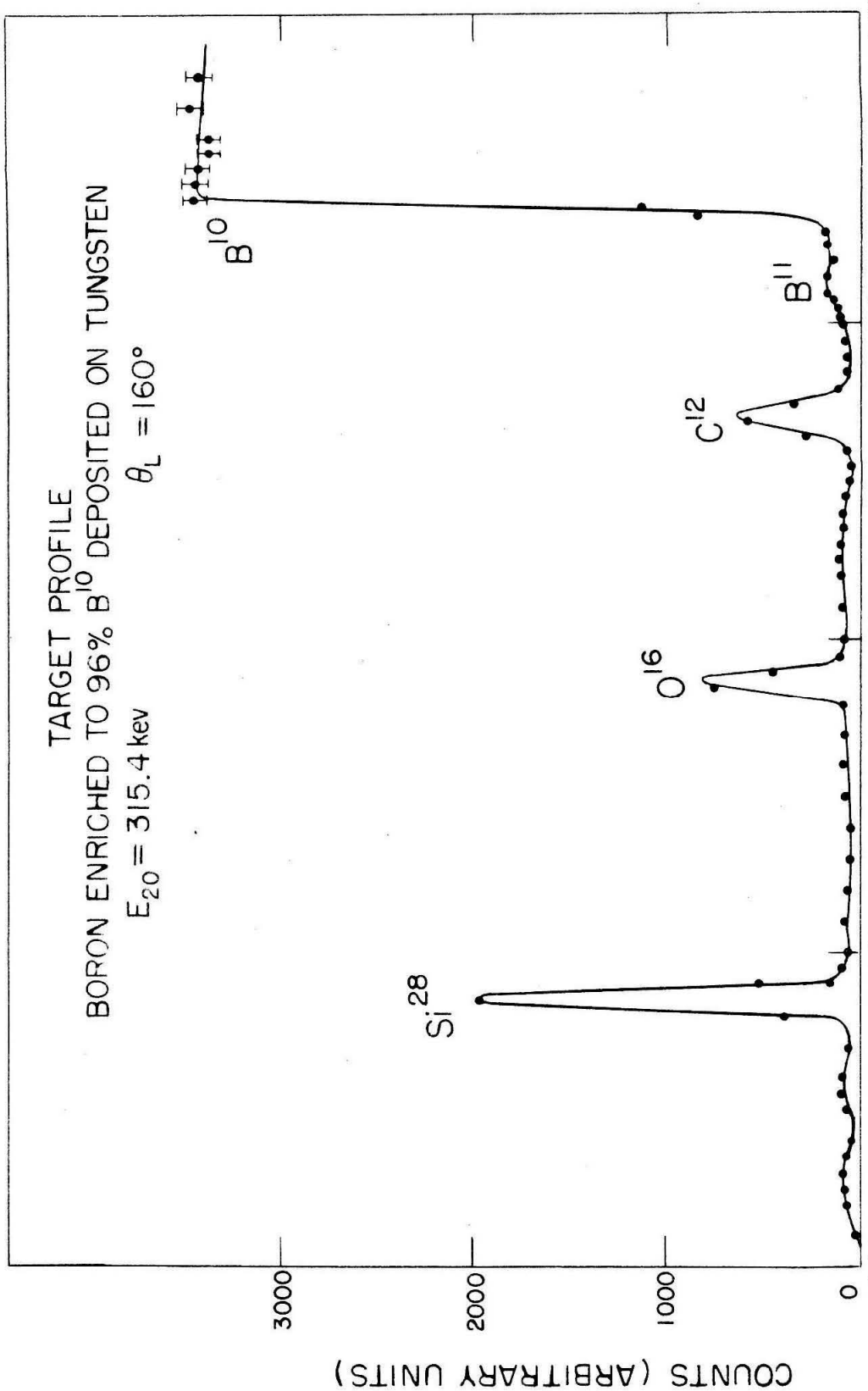
TARGET PROFILE
BORON ENRICHED TO 96% B10 DEPOSITED ON TUNGSTEN
E20 = 315.4 kev
θL = 160°
Si28
O16
C12
B11
B10
COUNTS (ARBITRARY UNITS)
0
1000
2000
3000
0.80
0.90
1.00
1.10
1.20
ELECTROSTATIC ANALYZER POTENTIOMETER SETTING (VOLTS)

FIGURE 3

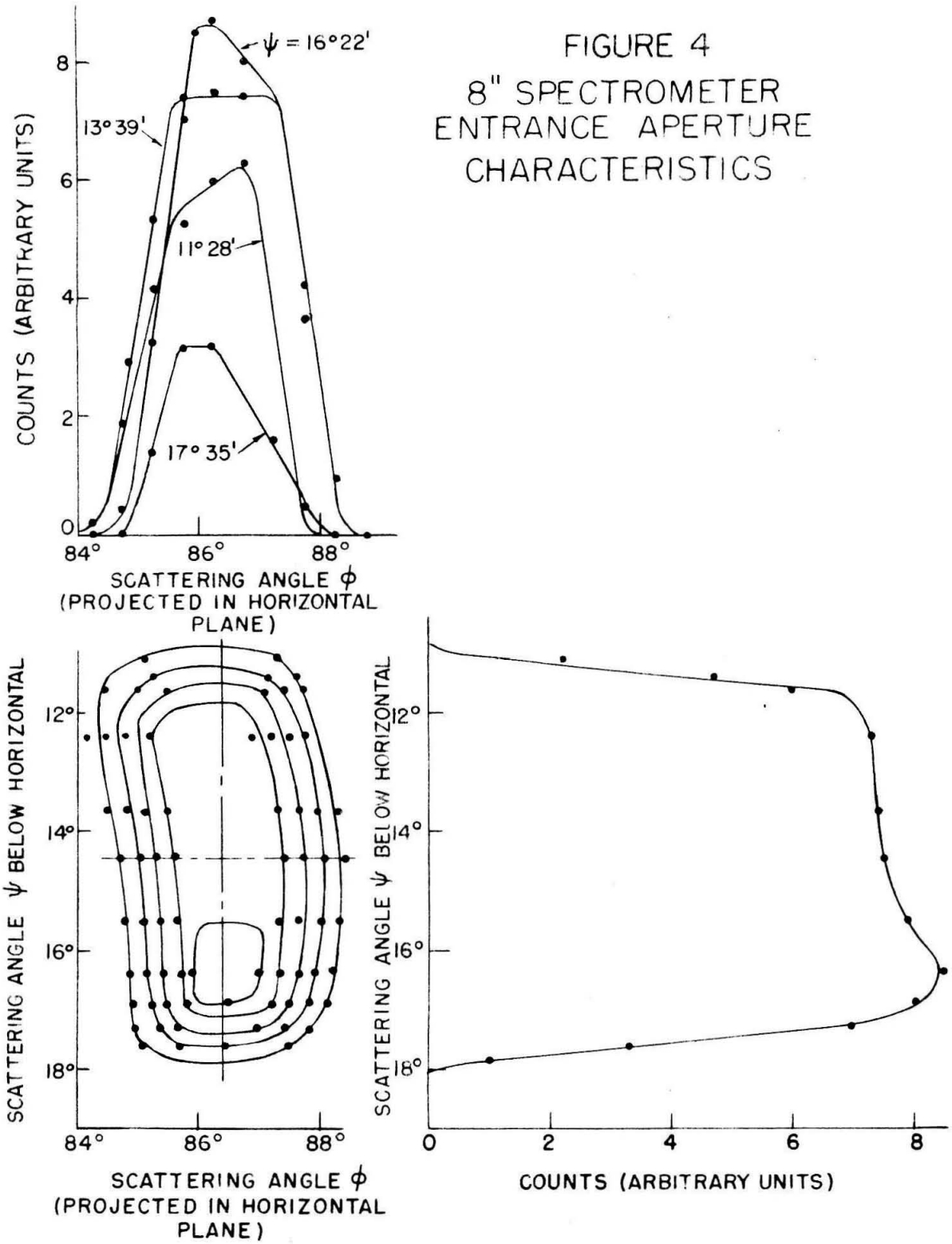

FIGURE 4
8" SPECTROMETER
ENTRANCE APERTURE
CHARACTERISTICS

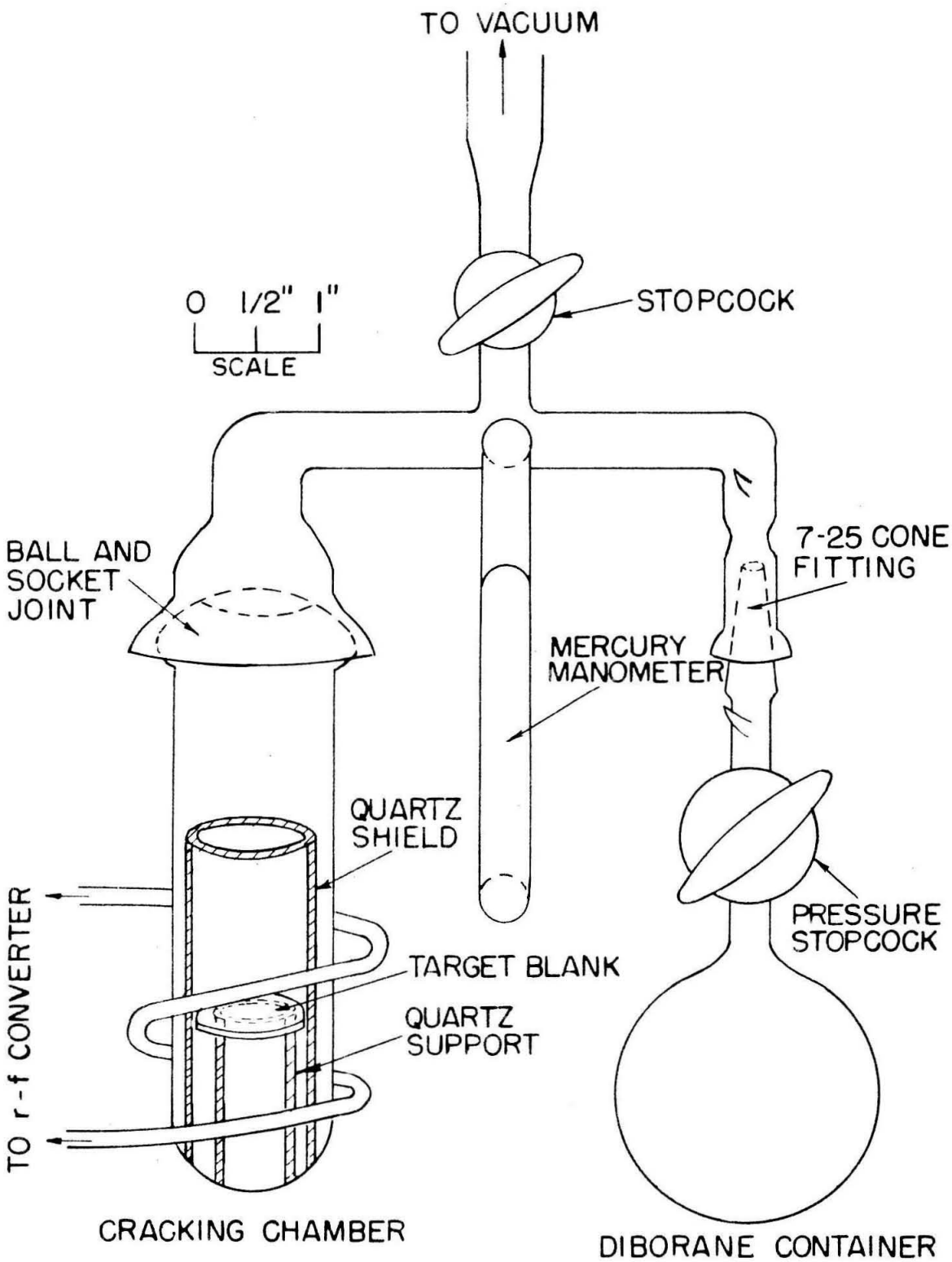

FIGURE 5
DIBORANE CRACKING APPARATUS

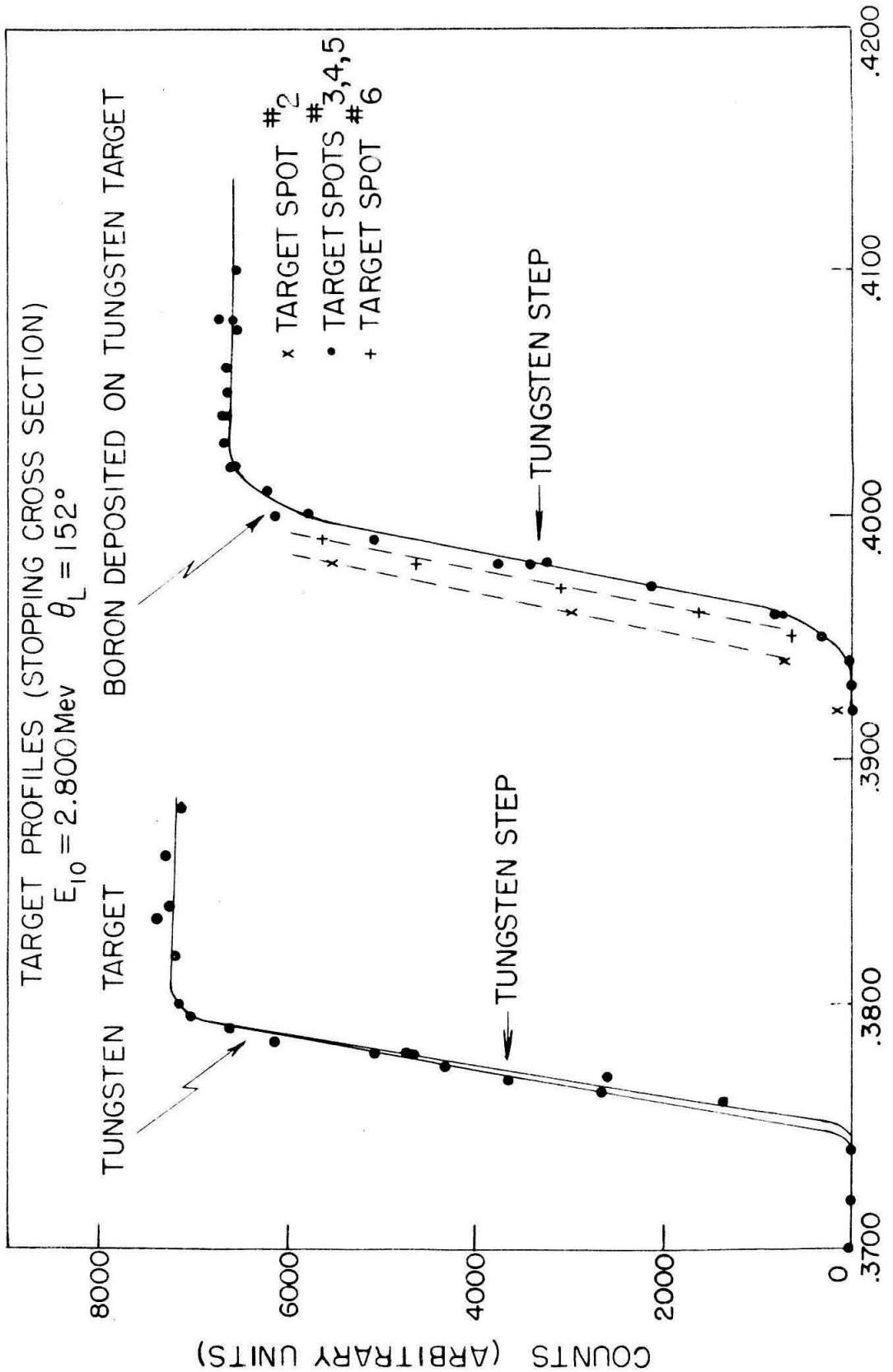
TARGET PROFILES (STOPPING CROSS SECTION)
$E_{10} = 2.800$ Mev $\theta_L = 152°$
TUNGSTEN TARGET
BORON DEPOSITED ON TUNGSTEN TARGET
x TARGET SPOT #2
• TARGET SPOTS #3,4,5
+ TARGET SPOT #6
TUNGSTEN STEP
TUNGSTEN STEP
COUNTS (ARBITRARY UNITS)
0
2000
4000
6000
8000
.3700
.3800
.3900
.4000
.4100
.4200
FLUXMETER SETTING (VOLTS)

FIGURE 6

FIGURE 7
ATOMIC STOPPING CROSS SECTION FOR PROTONS IN BORON

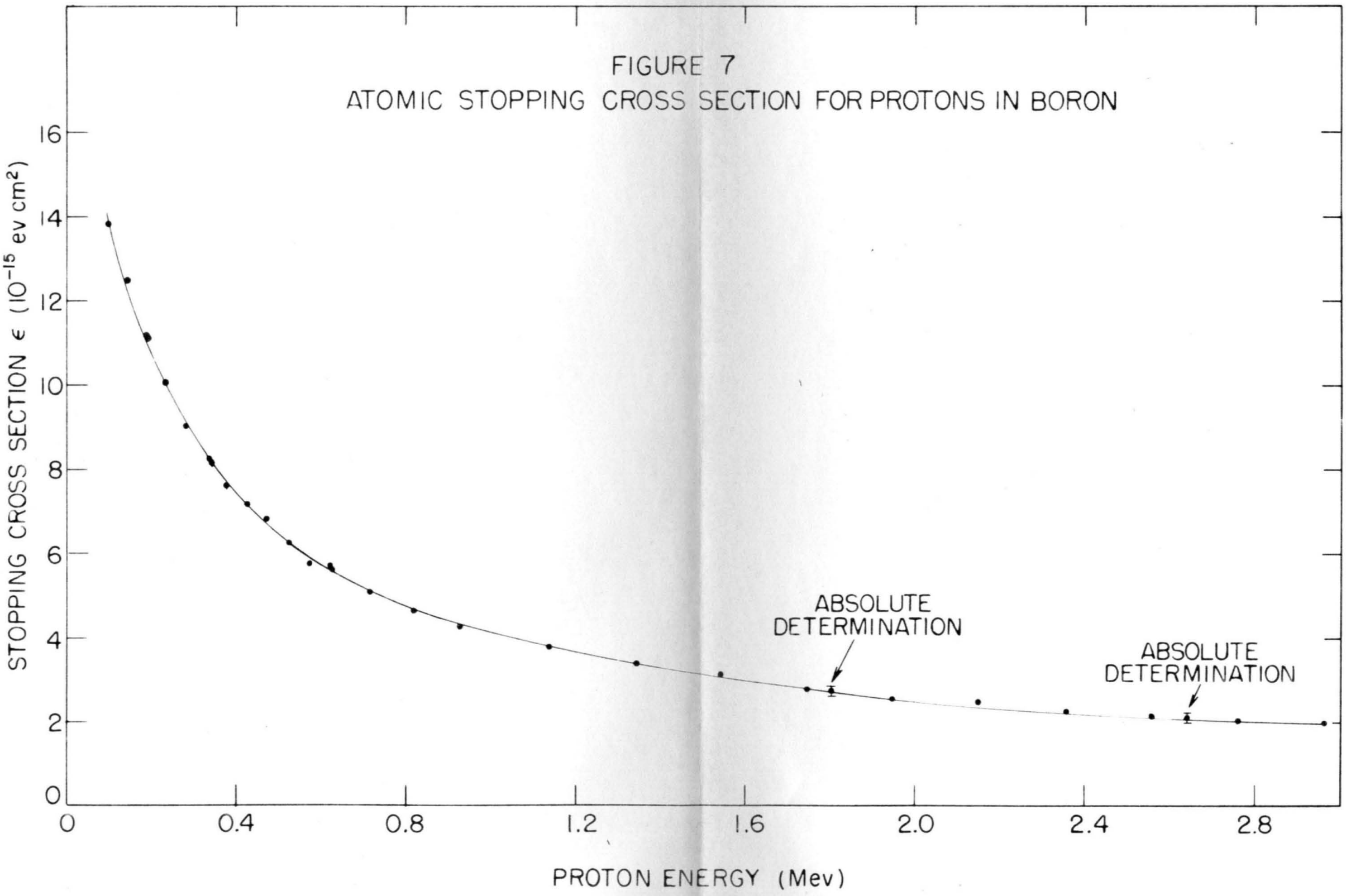

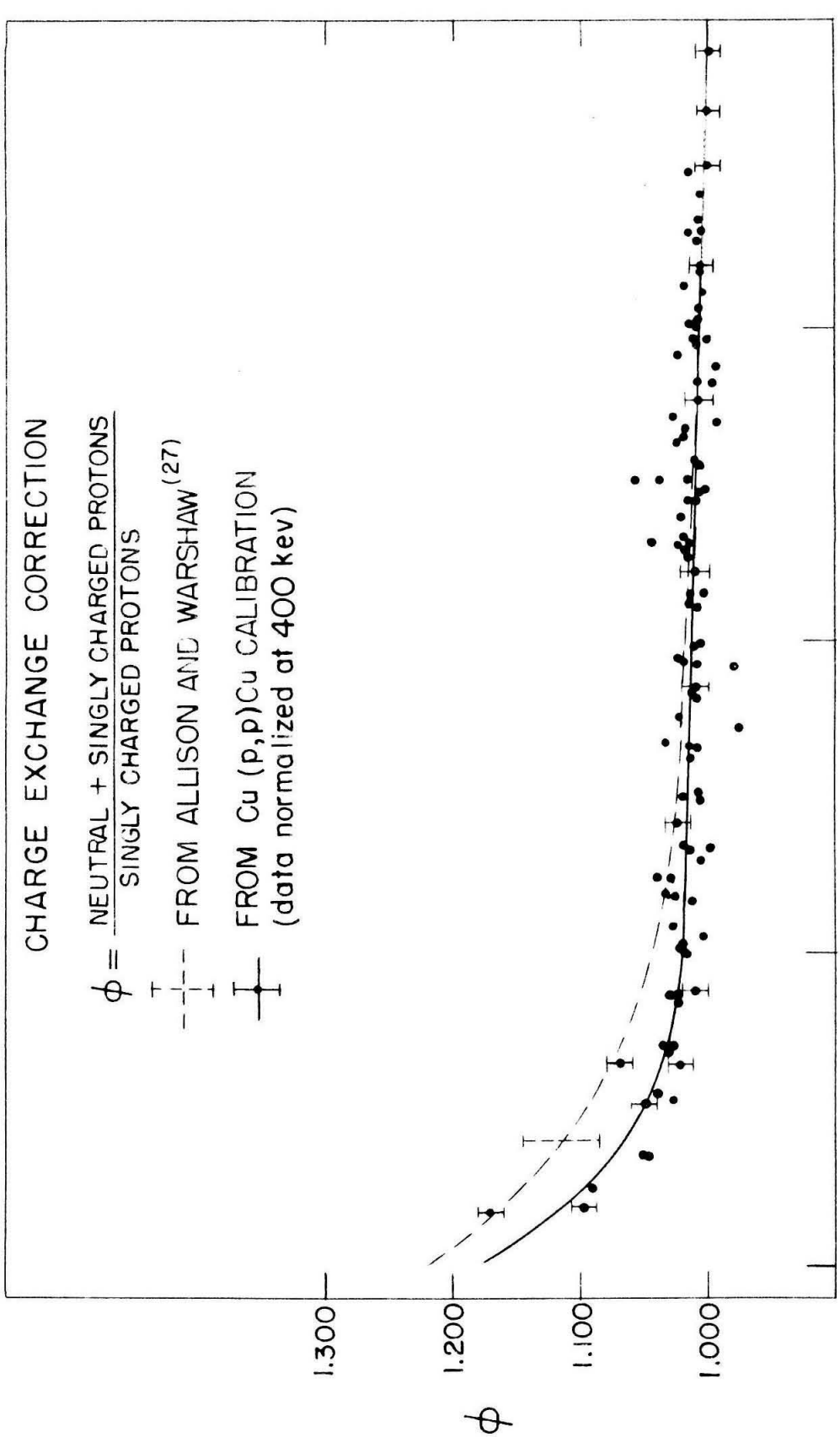
CHARGE EXCHANGE CORRECTION
ϕ = NEUTRAL + SINGLY CHARGED PROTONS / SINGLY CHARGED PROTONS
FROM ALLISON AND WARSHAW[27]
FROM Cu (p,p)Cu CALIBRATION
(data normalized at 400 kev)
1.300
1.200
1.100
1.000
ϕ
100
200
300
400
500
PROTON ENERGY (kev)

FIGURE 8

FIGURE 9

ELASTIC SCATTERING OF PROTONS BY BORON 10

$\left(\frac{d\sigma}{d\Omega}\right) \Big/ \left(\frac{d\sigma}{d\Omega}\right)_R$ NORMALIZED TO UNITY AT E < 200 kev

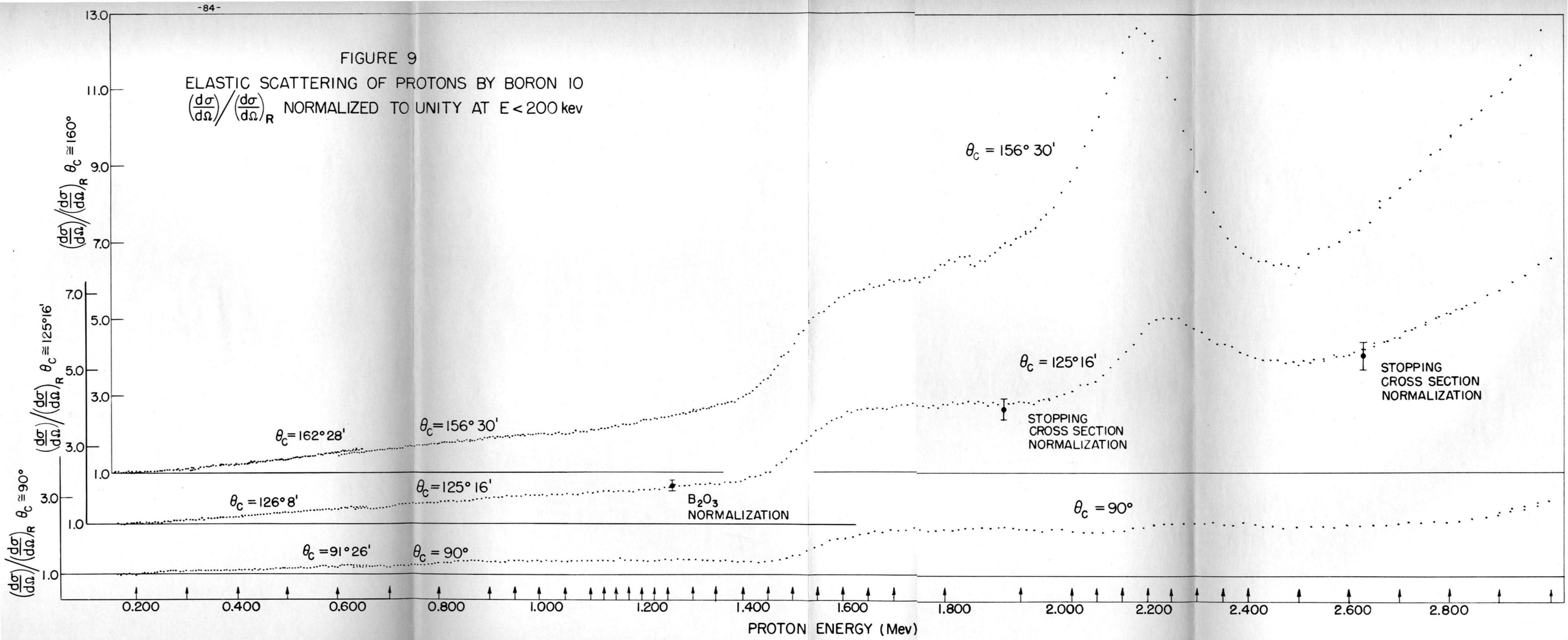

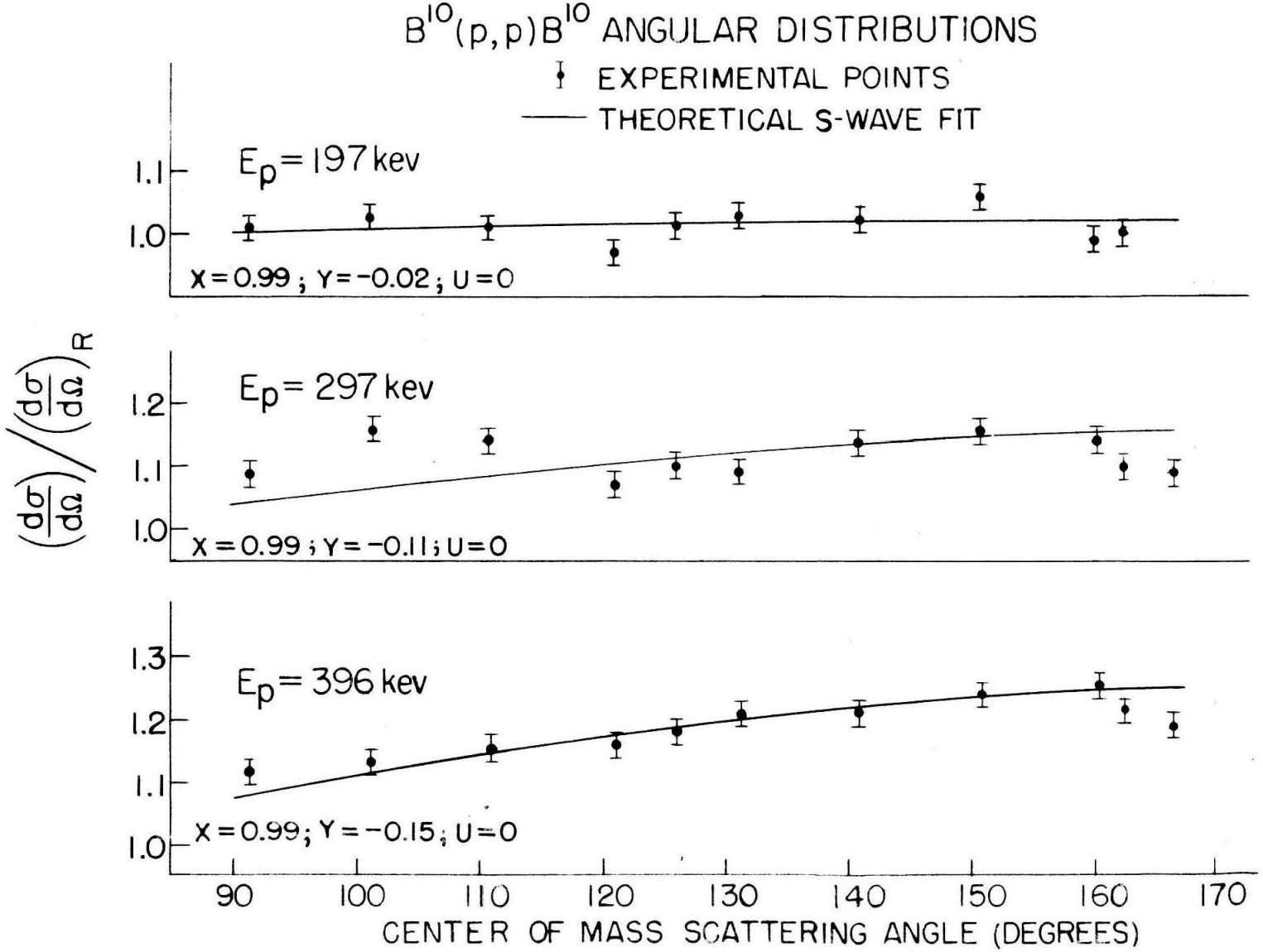
$B^{10}(p,p)B^{10}$ ANGULAR DISTRIBUTIONS
EXPERIMENTAL POINTS
THEORETICAL S-WAVE FIT
E_p = 197 kev
X = 0.99 ; Y = −0.02 ; U = 0
E_p = 297 kev
X = 0.99 ; Y = −0.11 ; U = 0
E_p = 396 kev
X = 0.99 ; Y = −0.15 ; U = 0
$\left(\frac{d\sigma}{d\Omega}\right) / \left(\frac{d\sigma}{d\Omega}\right)_R$
1.0
1.1
1.2
1.3
90
100
110
120
130
140
150
160
170
CENTER OF MASS SCATTERING ANGLE (DEGREES)

FIGURE 10

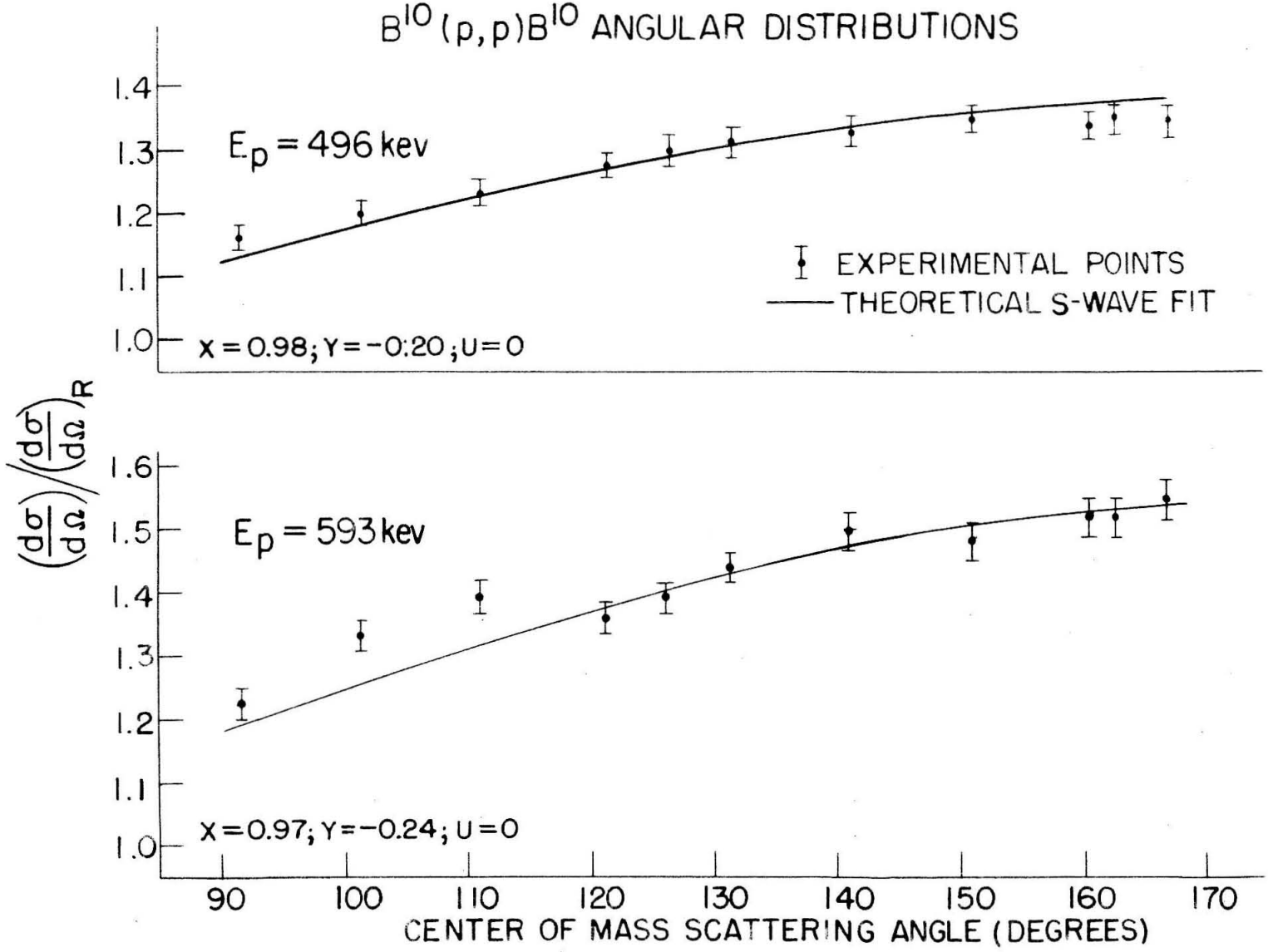
$B^{10}(p,p)B^{10}$ ANGULAR DISTRIBUTIONS
$E_p = 496$ kev
EXPERIMENTAL POINTS
THEORETICAL S-WAVE FIT
X = 0.98; Y = −0.20; U = 0
$E_p = 593$ kev
X = 0.97; Y = −0.24; U = 0
$\left(\frac{d\sigma}{d\Omega}\right)/\left(\frac{d\sigma}{d\Omega}\right)_R$
1.0
1.1
1.2
1.3
1.4
1.5
1.6
90
100
110
120
130
140
150
160
170
CENTER OF MASS SCATTERING ANGLE (DEGREES)

FIGURE 11

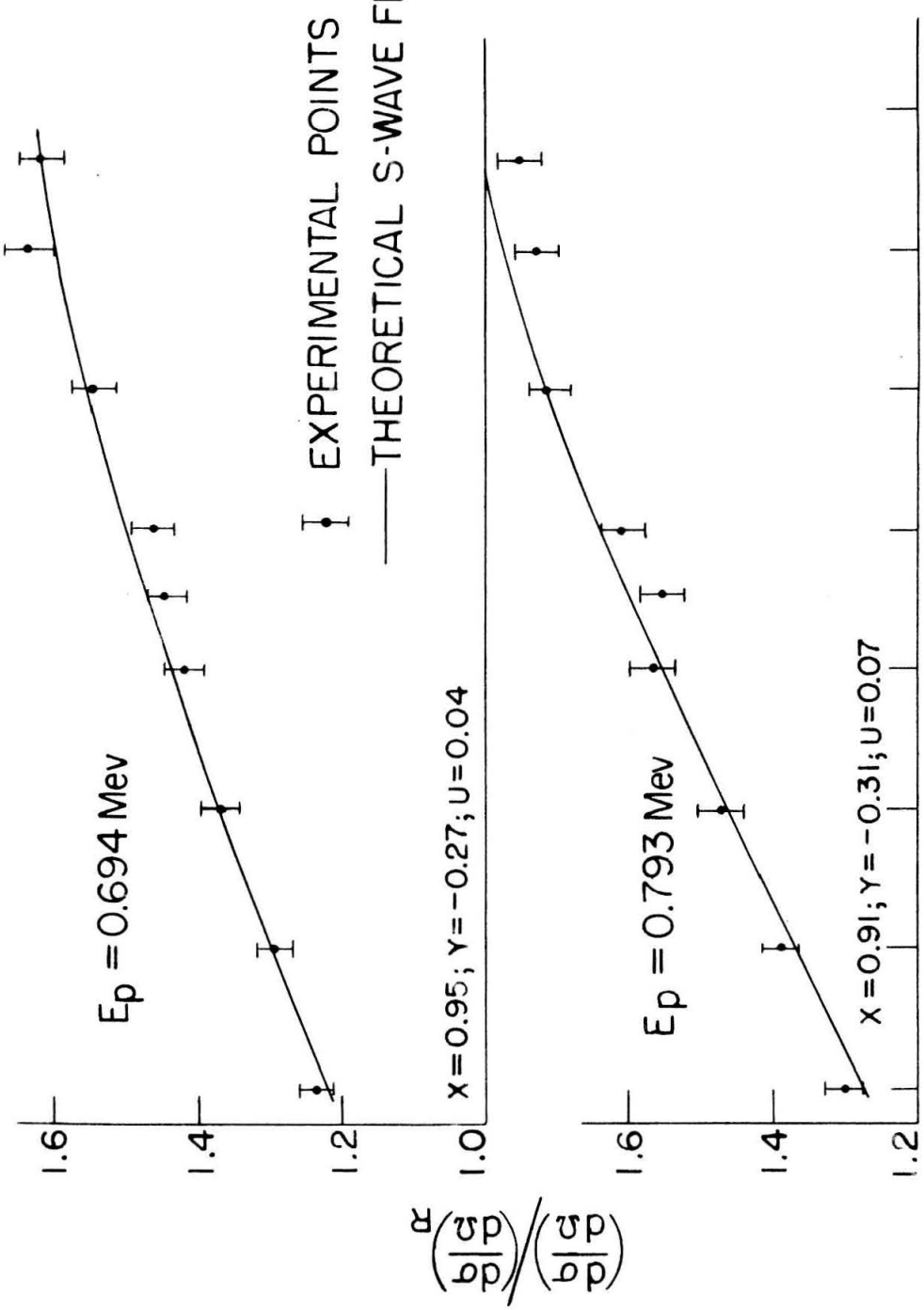
$B^{10}(p,p)B^{10}$ ANGULAR DISTRIBUTIONS
EXPERIMENTAL POINTS
THEORETICAL S-WAVE FIT
$E_p = 0.694$ Mev
$x = 0.95; \gamma = -0.27; U = 0.04$
$E_p = 0.793$ Mev
$x = 0.91; \gamma = -0.31; U = 0.07$
$\left(\frac{d\sigma}{d\Omega}\right) / \left(\frac{d\sigma}{d\Omega}\right)_R$
1.6
1.4
1.2
1.0
90
100
110
120
130
140
150
160
CENTER OF MASS SCATTERING ANGLE (DEGREES)

FIGURE 12

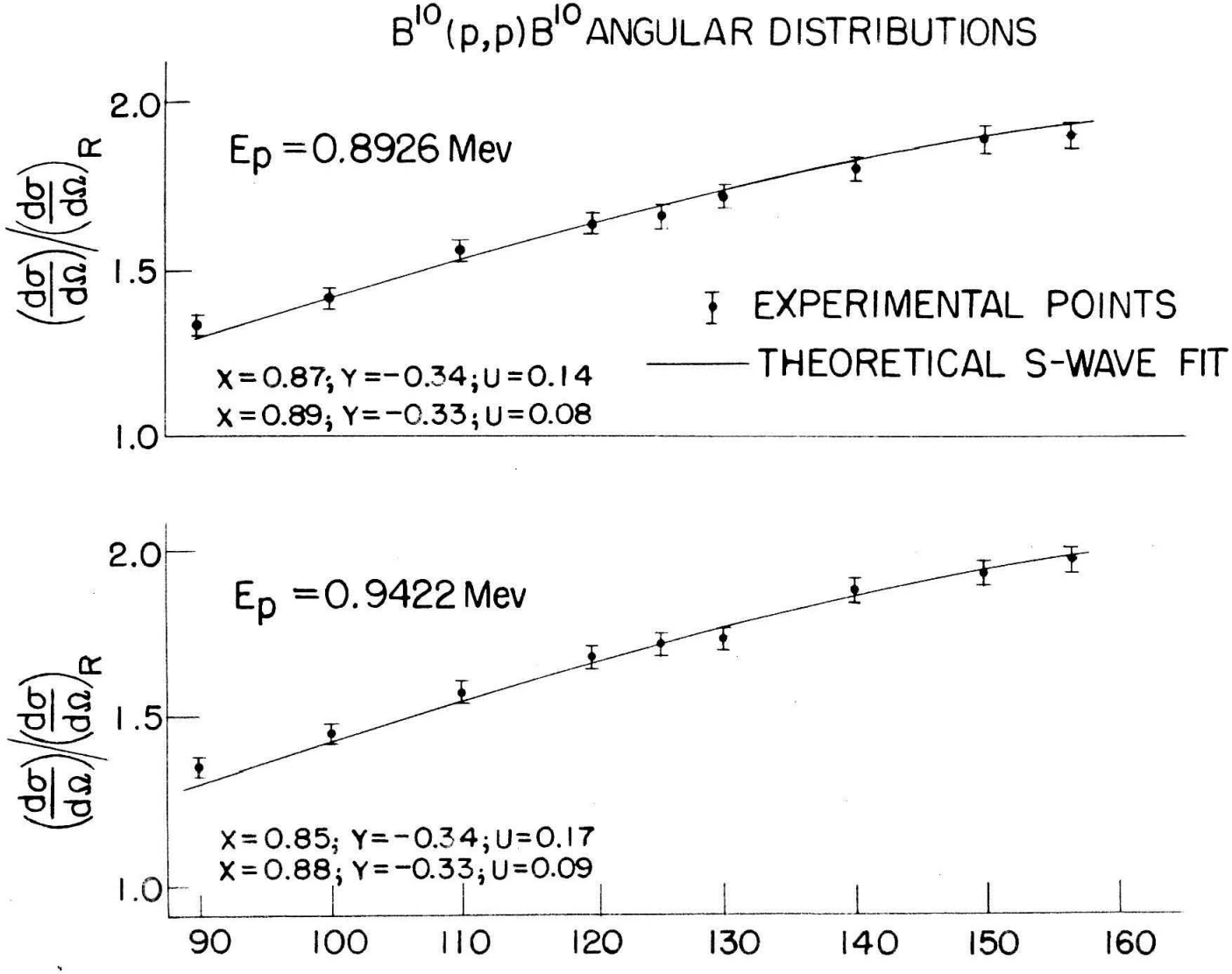
$B^{10}(p,p)B^{10}$ ANGULAR DISTRIBUTIONS
$\left(\frac{d\sigma}{d\Omega}\right)/\left(\frac{d\sigma}{d\Omega}\right)_R$
2.0
1.5
1.0
E_p = 0.8926 Mev
X = 0.87; Y = −0.34; U = 0.14
X = 0.89; Y = −0.33; U = 0.08
EXPERIMENTAL POINTS
THEORETICAL S-WAVE FIT
E_p = 0.9422 Mev
X = 0.85; Y = −0.34; U = 0.17
X = 0.88; Y = −0.33; U = 0.09
90
100
110
120
130
140
150
160
CENTER OF MASS SCATTERING ANGLE (DEGREES)

FIGURE 13

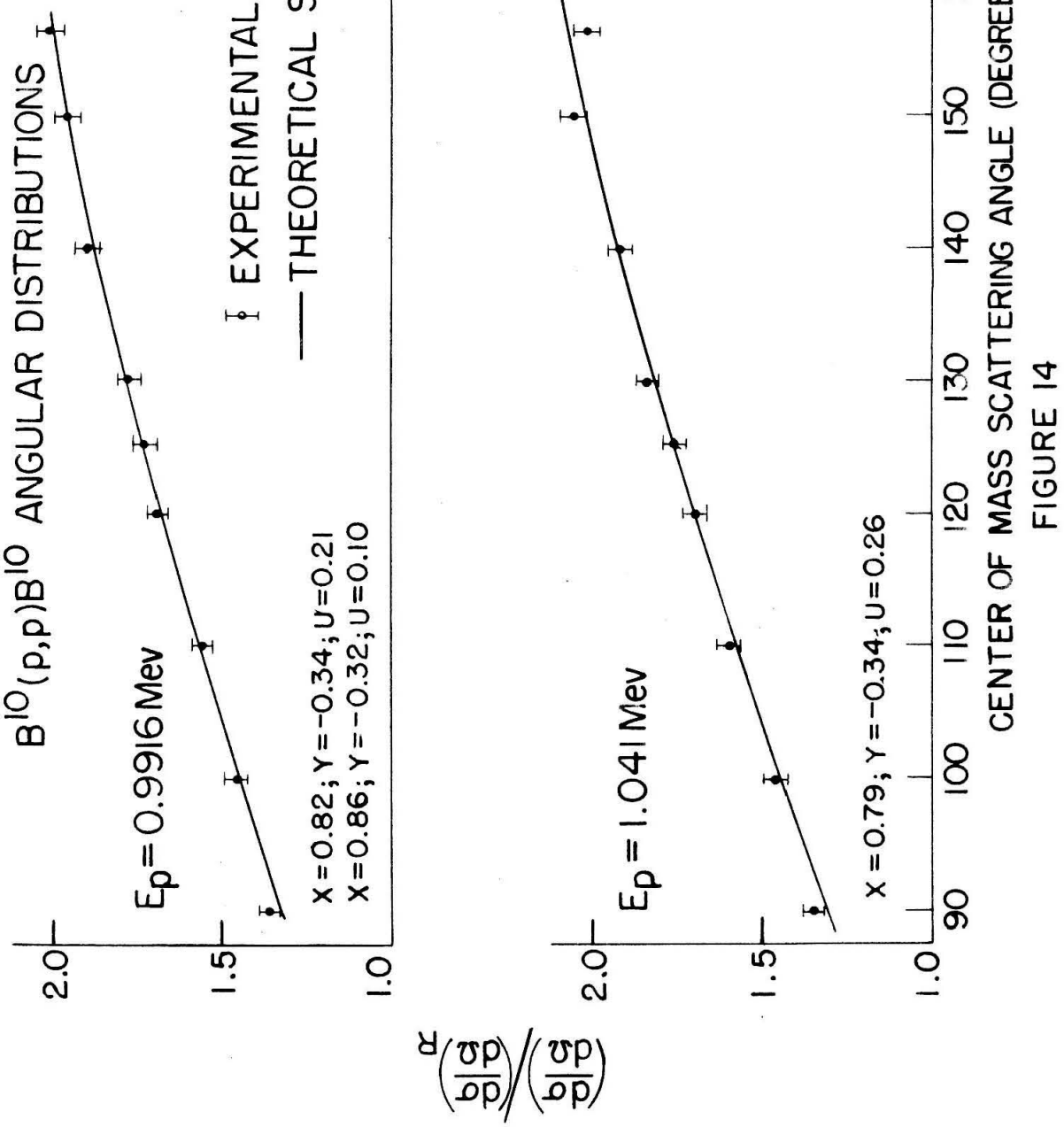
B10(p,p)B10 ANGULAR DISTRIBUTIONS
EXPERIMENTAL POINTS
THEORETICAL S-WAVE FIT
Ep = 0.9916 Mev
X = 0.82; Y = −0.34; U = 0.21
X = 0.86; Y = −0.32; U = 0.10
Ep = 1.041 Mev
X = 0.79; Y = −0.34; U = 0.26
(dσ/dΩ)/(dσ/dΩ)R
2.0
1.5
1.0
90
100
110
120
130
140
150
160
CENTER OF MASS SCATTERING ANGLE (DEGREES)

FIGURE 14

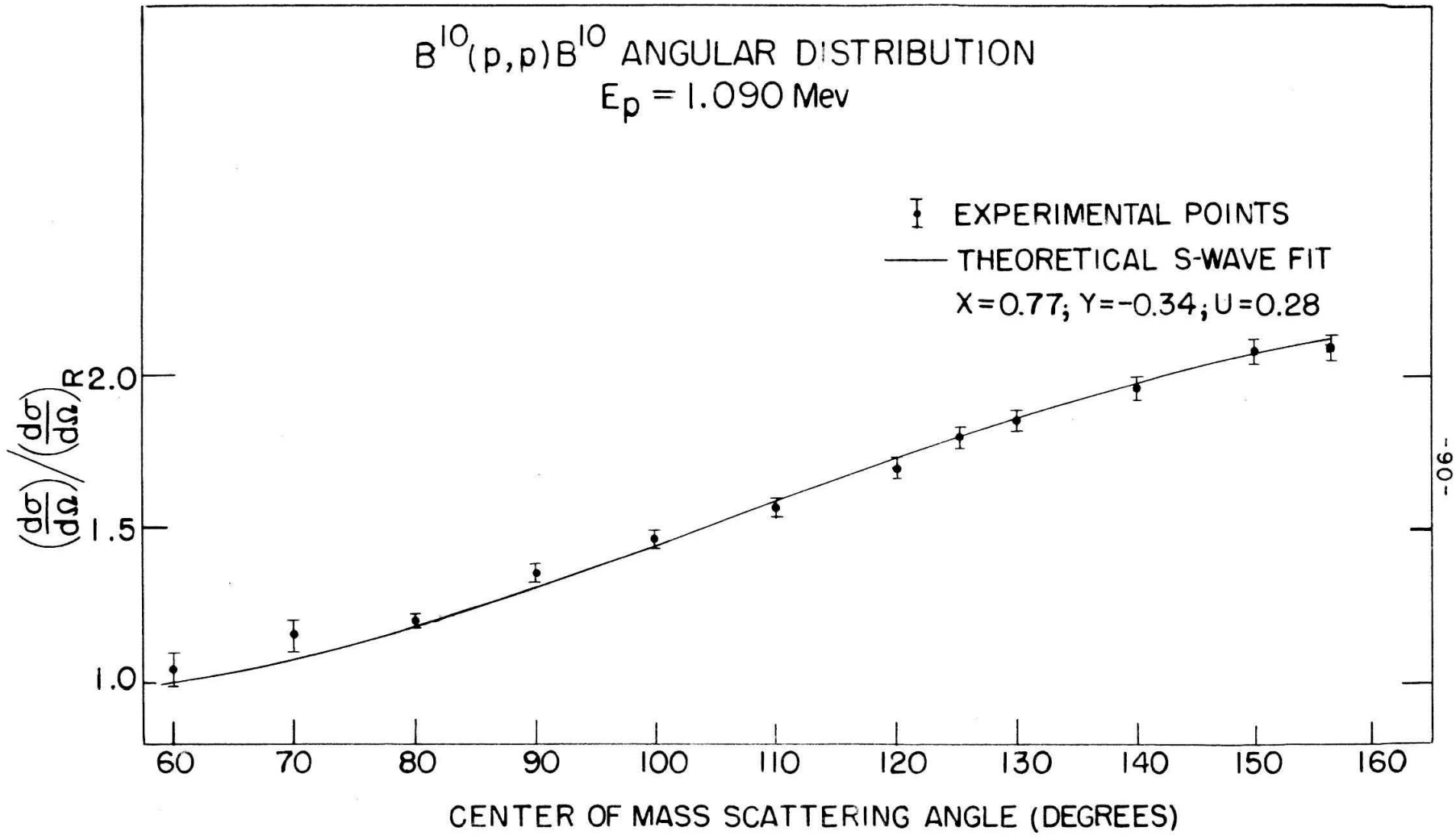
$B^{10}(p,p)B^{10}$ ANGULAR DISTRIBUTION
E_p = 1.090 Mev
EXPERIMENTAL POINTS
THEORETICAL S-WAVE FIT
X=0.77; Y=-0.34; U=0.28
$\left(\frac{d\sigma}{d\Omega}\right)/\left(\frac{d\sigma}{d\Omega}\right)_R$
2.0
1.5
1.0
60
70
80
90
100
110
120
130
140
150
160
CENTER OF MASS SCATTERING ANGLE (DEGREES)

FIGURE 15

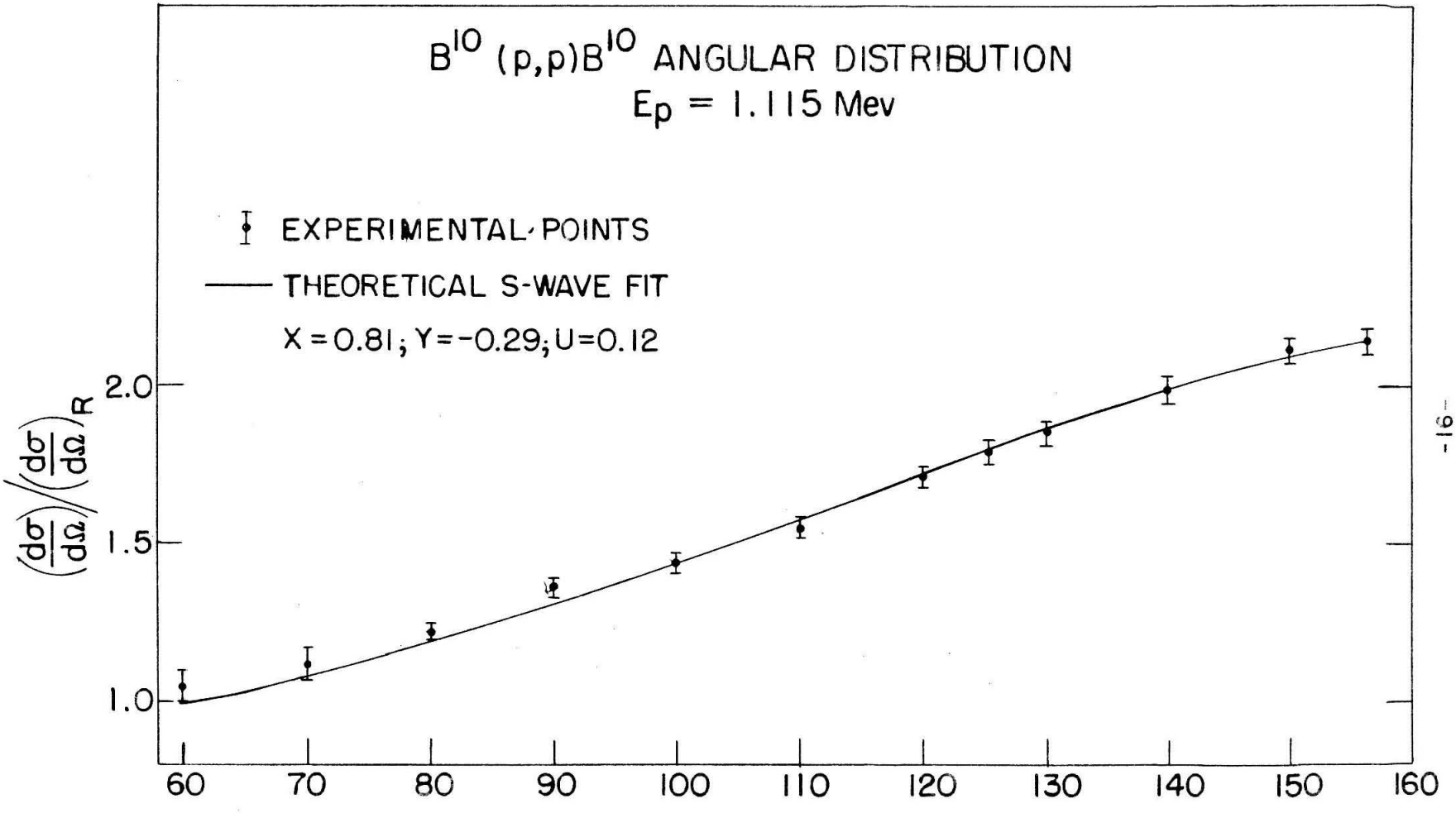
$B^{10}(p,p)B^{10}$ ANGULAR DISTRIBUTION
E_p = 1.115 Mev
EXPERIMENTAL POINTS
THEORETICAL S-WAVE FIT
X = 0.81; Y = -0.29; U = 0.12
$\left(\frac{d\sigma}{d\Omega}\right)/\left(\frac{d\sigma}{d\Omega}\right)_R$
2.0
1.5
1.0
60
70
80
90
100
110
120
130
140
150
160
CENTER OF MASS SCATTERING ANGLE (DEGREES)

FIGURE 16

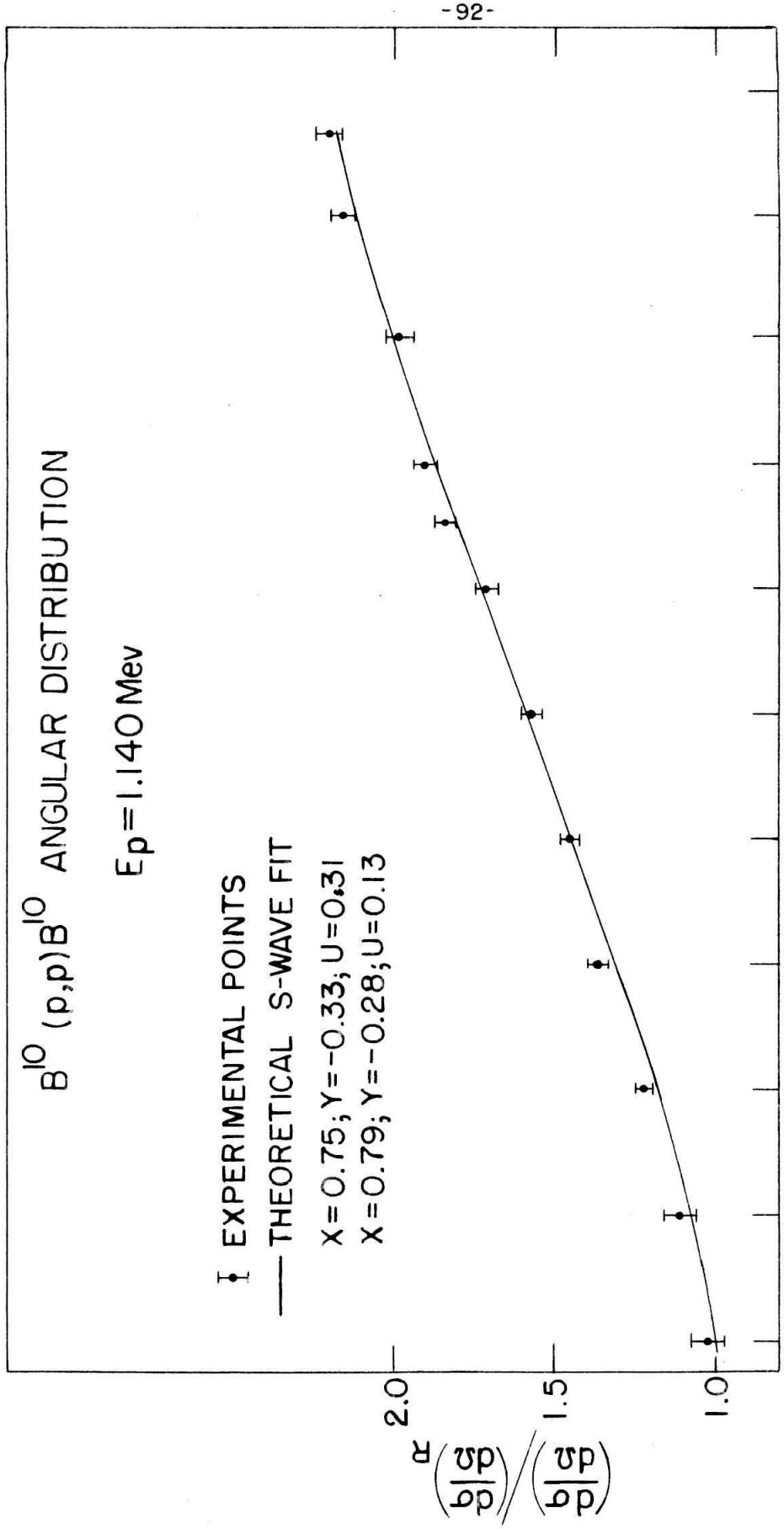
$B^{10}(p,p)B^{10}$ ANGULAR DISTRIBUTION
E_p=1.140 Mev
EXPERIMENTAL POINTS
THEORETICAL S-WAVE FIT
X=0.75; Y=-0.33; U=0.31
X=0.79; Y=-0.28; U=0.13
$\left(\frac{d\sigma}{d\Omega}\right)\Big/\left(\frac{d\sigma}{d\Omega}\right)_R$
2.0
1.5
1.0
60
70
80
90
100
110
120
130
140
150
160
CENTER OF MASS SCATTERING ANGLE (DEGREES)

FIGURE 17

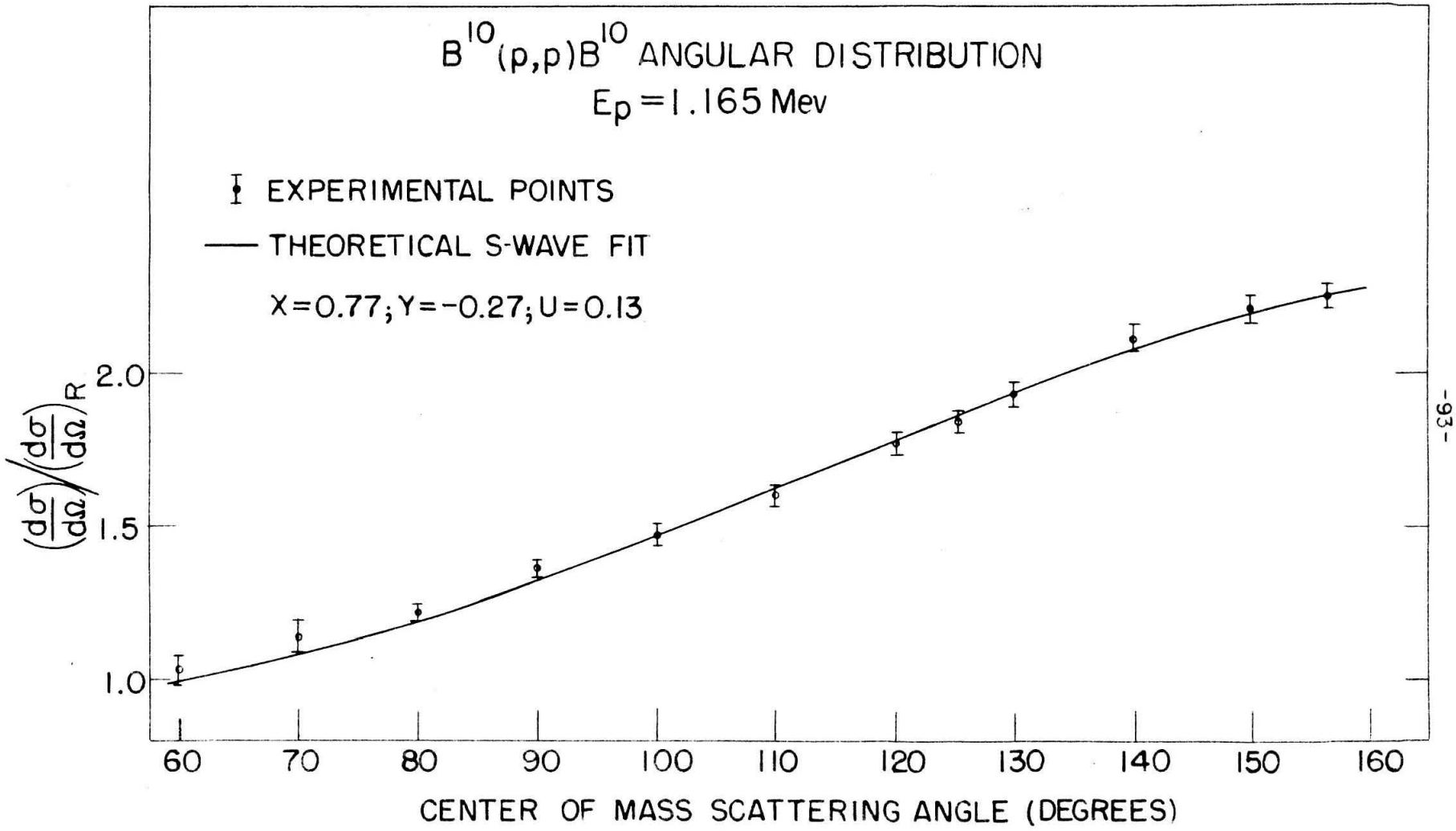
$B^{10}(p,p)B^{10}$ ANGULAR DISTRIBUTION
$E_p = 1.165$ Mev
EXPERIMENTAL POINTS
THEORETICAL S-WAVE FIT
X=0.77; Y=-0.27; U=0.13
$\frac{(d\sigma/d\Omega)}{(d\sigma/d\Omega)_R}$
2.0
1.5
1.0
60
70
80
90
100
110
120
130
140
150
160
CENTER OF MASS SCATTERING ANGLE (DEGREES)

FIGURE 18

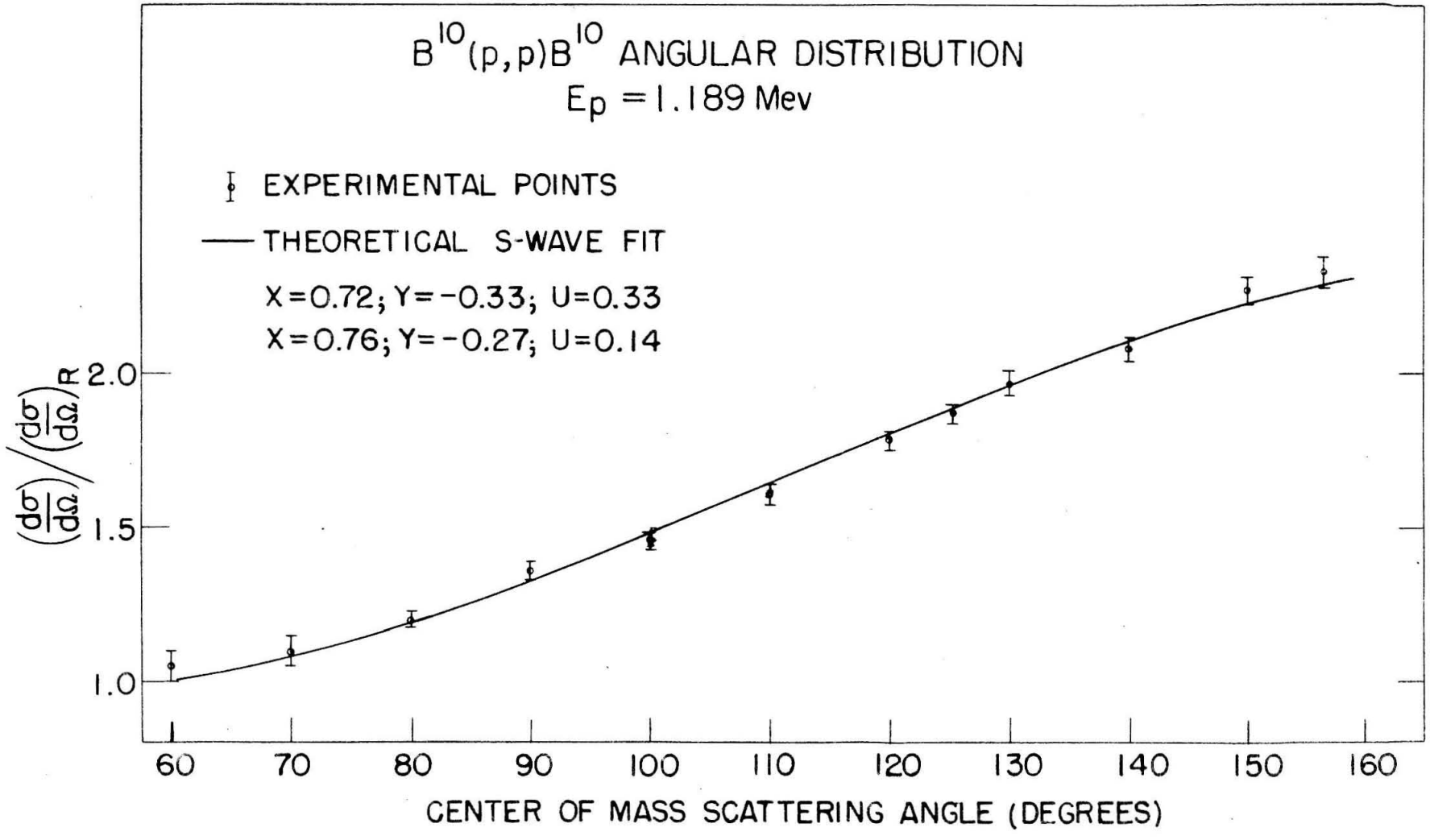
$B^{10}(p,p)B^{10}$ ANGULAR DISTRIBUTION
$E_p = 1.189$ Mev
EXPERIMENTAL POINTS
THEORETICAL S-WAVE FIT
X=0.72; Y=-0.33; U=0.33
X=0.76; Y=-0.27; U=0.14
$\frac{(d\sigma/d\Omega)}{(d\sigma/d\Omega)_R}$
2.0
1.5
1.0
60
70
80
90
100
110
120
130
140
150
160
CENTER OF MASS SCATTERING ANGLE (DEGREES)

FIGURE 19

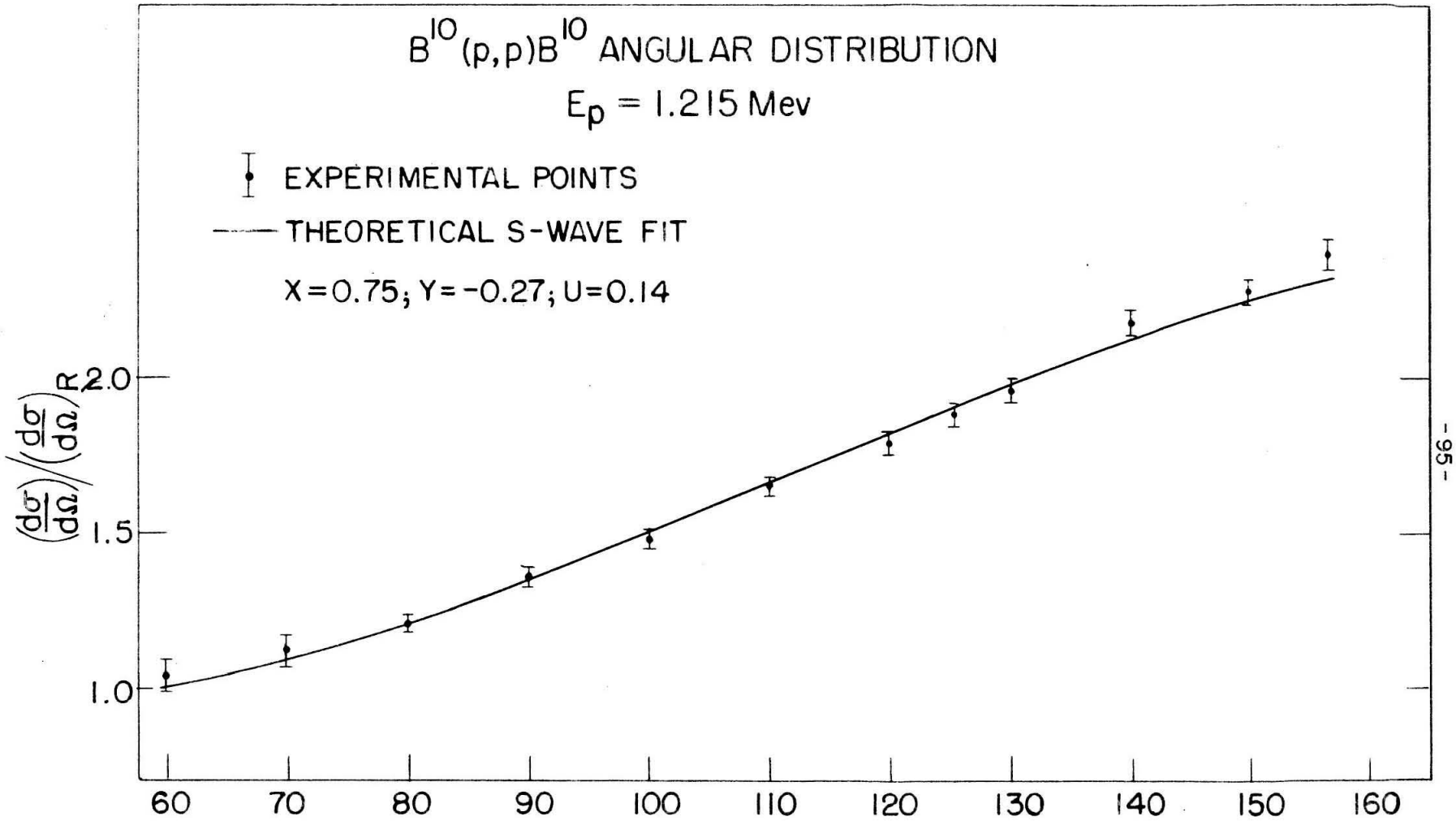
$B^{10}(p,p)B^{10}$ ANGULAR DISTRIBUTION
E_p = 1.215 Mev
EXPERIMENTAL POINTS
THEORETICAL S-WAVE FIT
X=0.75; Y=-0.27; U=0.14
$\frac{(d\sigma/d\Omega)}{(d\sigma/d\Omega)_R}$
2.0
1.5
1.0
60
70
80
90
100
110
120
130
140
150
160
CENTER OF MASS SCATTERING ANGLE (DEGREES)

FIGURE 20

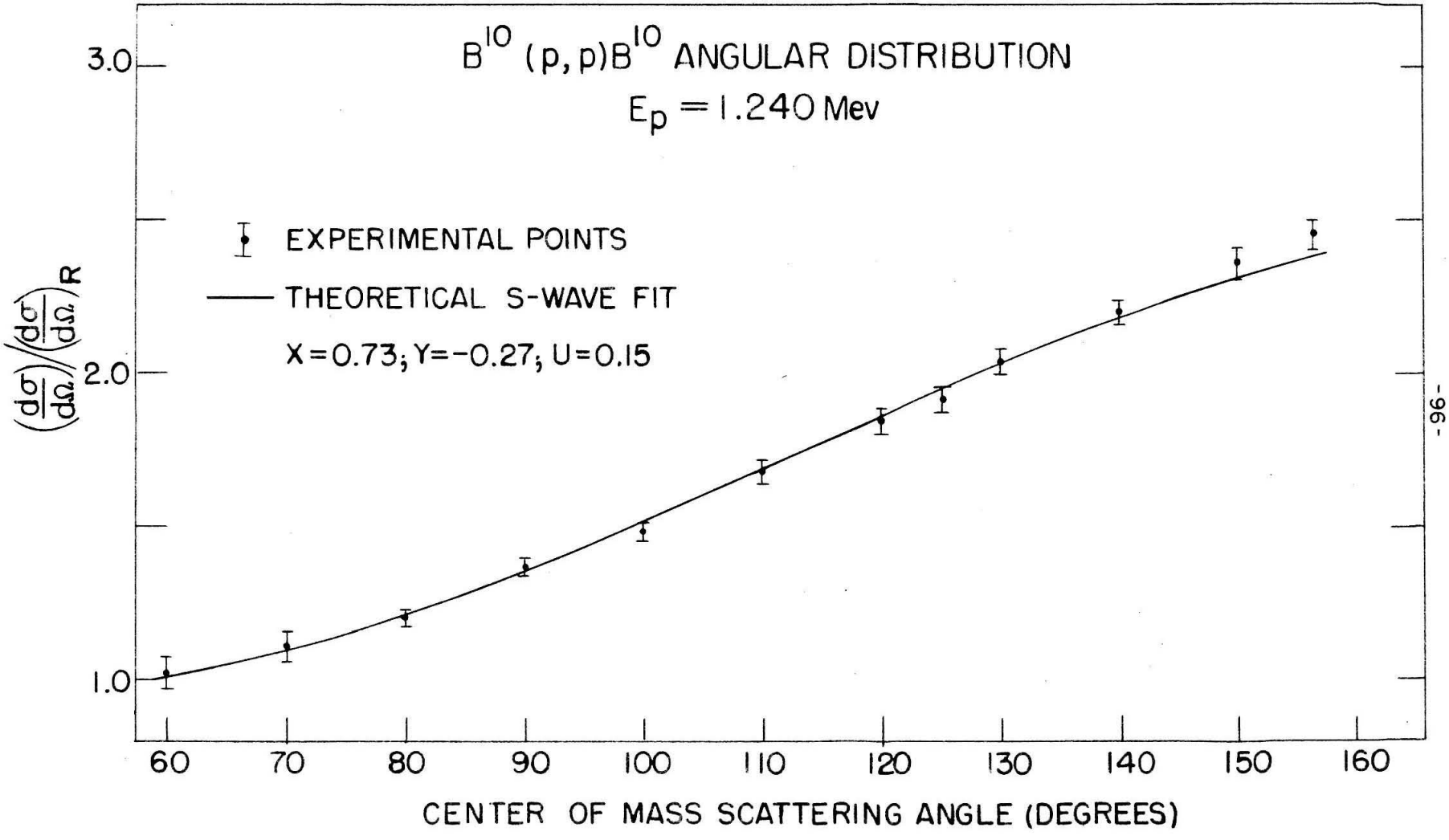
$B^{10}(p,p)B^{10}$ ANGULAR DISTRIBUTION
$E_p = 1.240$ Mev
EXPERIMENTAL POINTS
THEORETICAL S-WAVE FIT
X=0.73; Y=-0.27; U=0.15
$\left(\frac{d\sigma}{d\Omega}\right)/\left(\frac{d\sigma}{d\Omega}\right)_R$
3.0
2.0
1.0
60
70
80
90
100
110
120
130
140
150
160
CENTER OF MASS SCATTERING ANGLE (DEGREES)

FIGURE 21

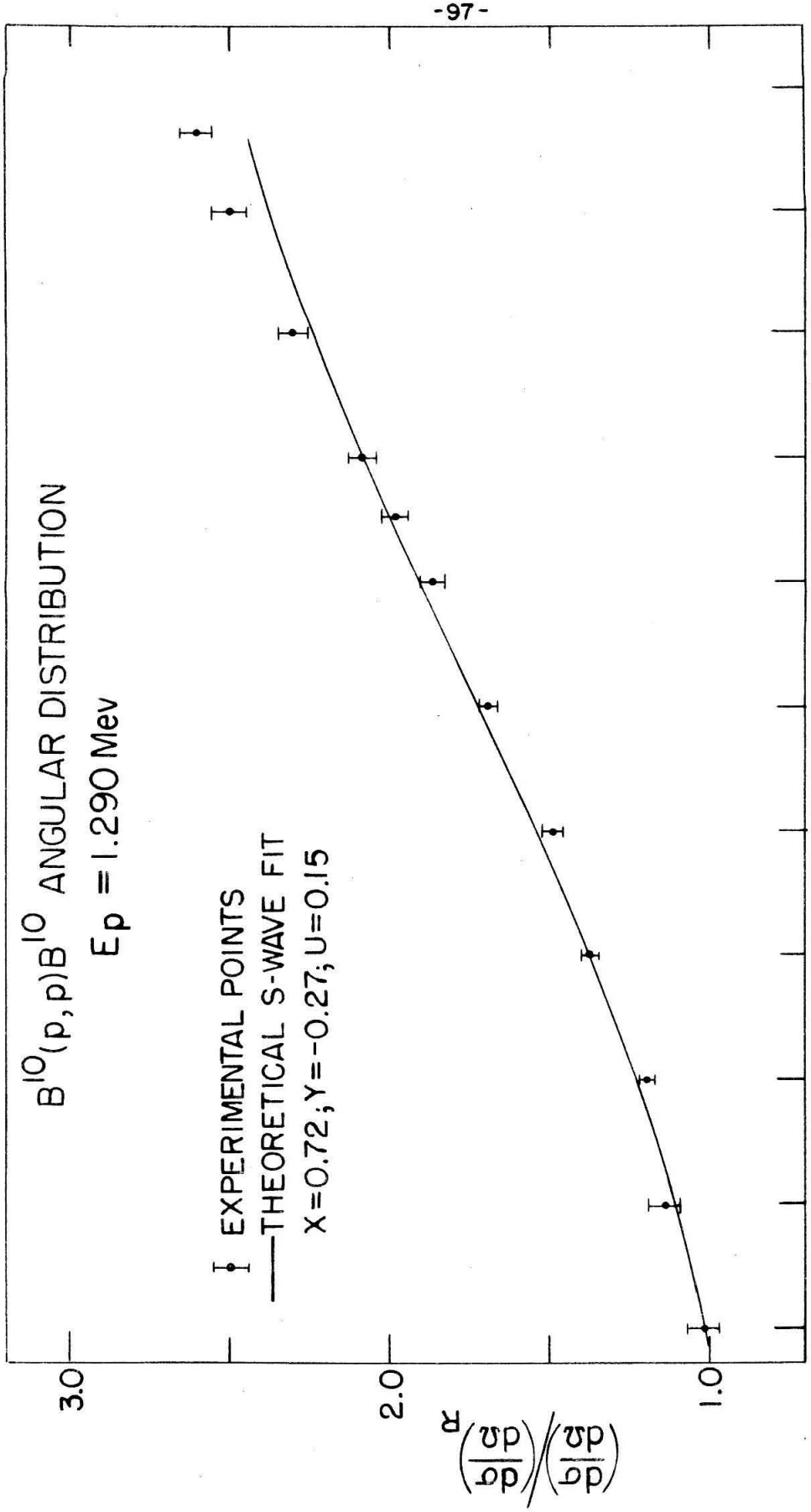
$B^{10}(p,p)B^{10}$ ANGULAR DISTRIBUTION
E_p = 1.290 Mev
EXPERIMENTAL POINTS
THEORETICAL S-WAVE FIT
X=0.72; Y=-0.27; U=0.15
$\left(\frac{d\sigma}{d\Omega}\right)\Big/\left(\frac{d\sigma}{d\Omega}\right)_R$
3.0
2.0
1.0
60
70
80
90
100
110
120
130
140
150
160
CENTER OF MASS SCATTERING ANGLE (DEGREES)

FIGURE 22

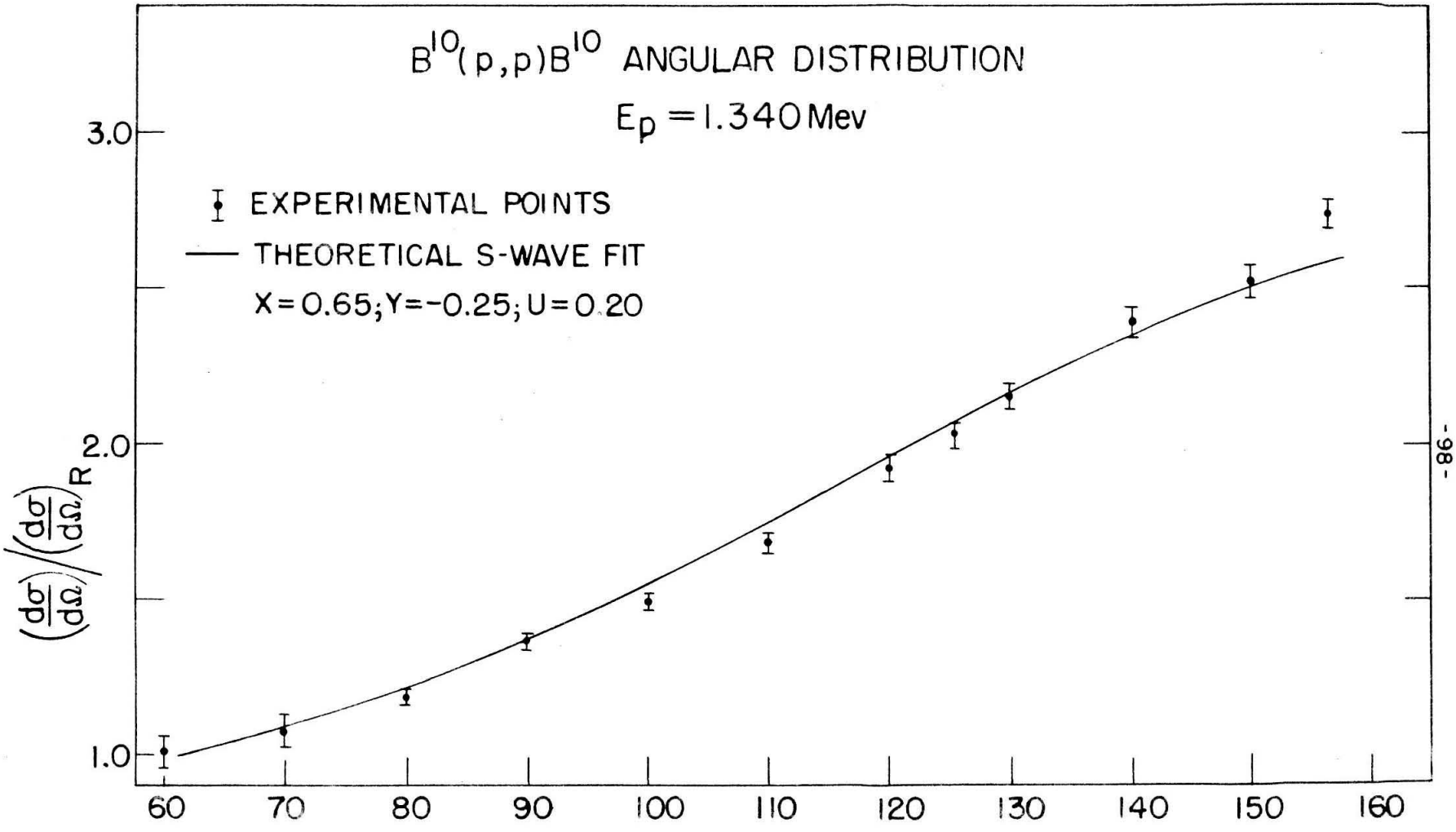
$B^{10}(p,p)B^{10}$ ANGULAR DISTRIBUTION
$E_p = 1.340$ Mev
EXPERIMENTAL POINTS
THEORETICAL S-WAVE FIT
X=0.65; Y=-0.25; U=0.20
$\left(\frac{d\sigma}{d\Omega}\right)/\left(\frac{d\sigma}{d\Omega}\right)_R$
3.0
2.0
1.0
60
70
80
90
100
110
120
130
140
150
160
CENTER OF MASS SCATTERING ANGLE (DEGREES)

FIGURE 23

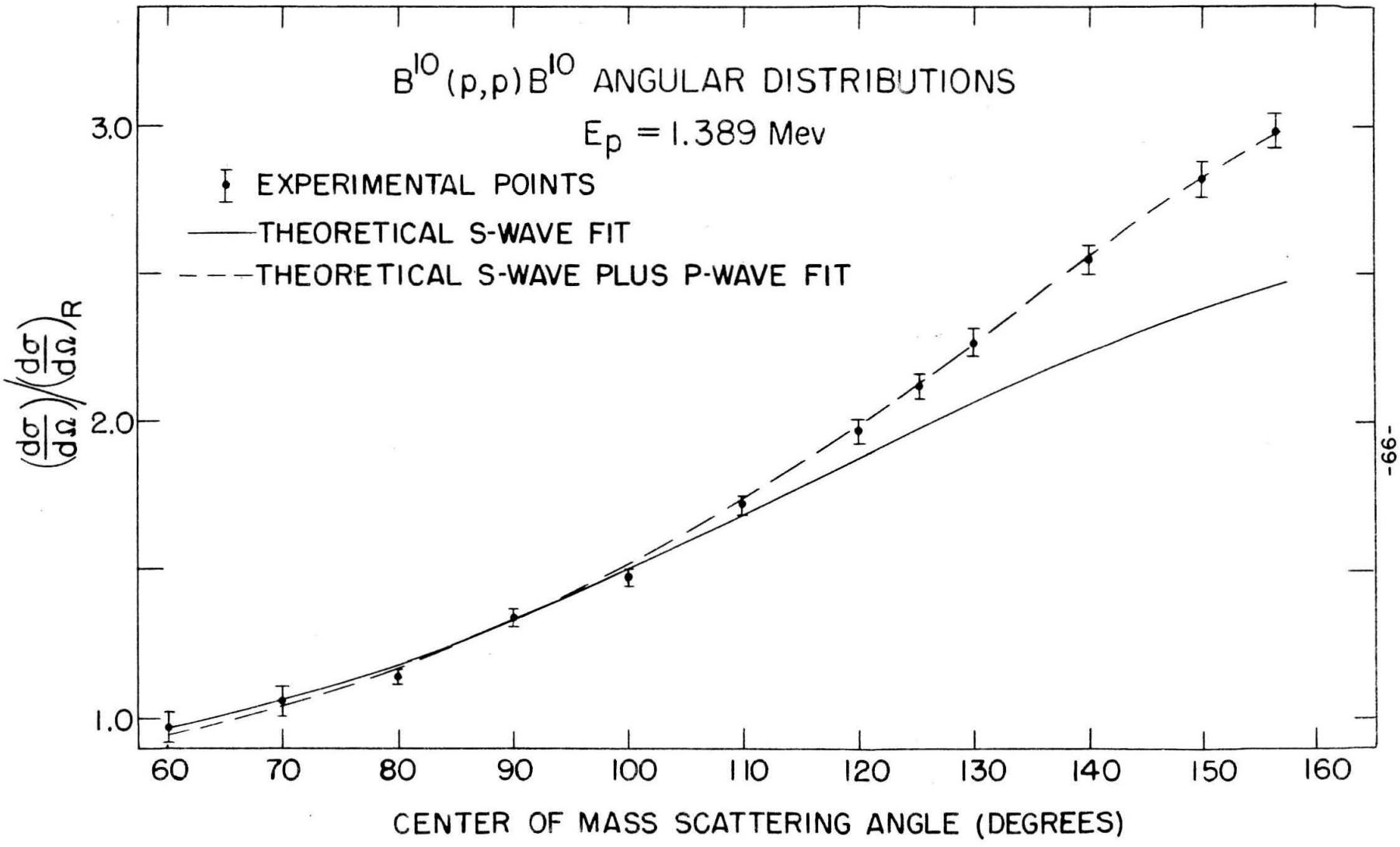
$B^{10}(p,p)B^{10}$ ANGULAR DISTRIBUTIONS
$E_p = 1.389$ Mev
EXPERIMENTAL POINTS
THEORETICAL S-WAVE FIT
THEORETICAL S-WAVE PLUS P-WAVE FIT
$\left(\frac{d\sigma}{d\Omega}\right)/\left(\frac{d\sigma}{d\Omega}\right)_R$
3.0
2.0
1.0
60
70
80
90
100
110
120
130
140
150
160
CENTER OF MASS SCATTERING ANGLE (DEGREES)

FIGURE 24

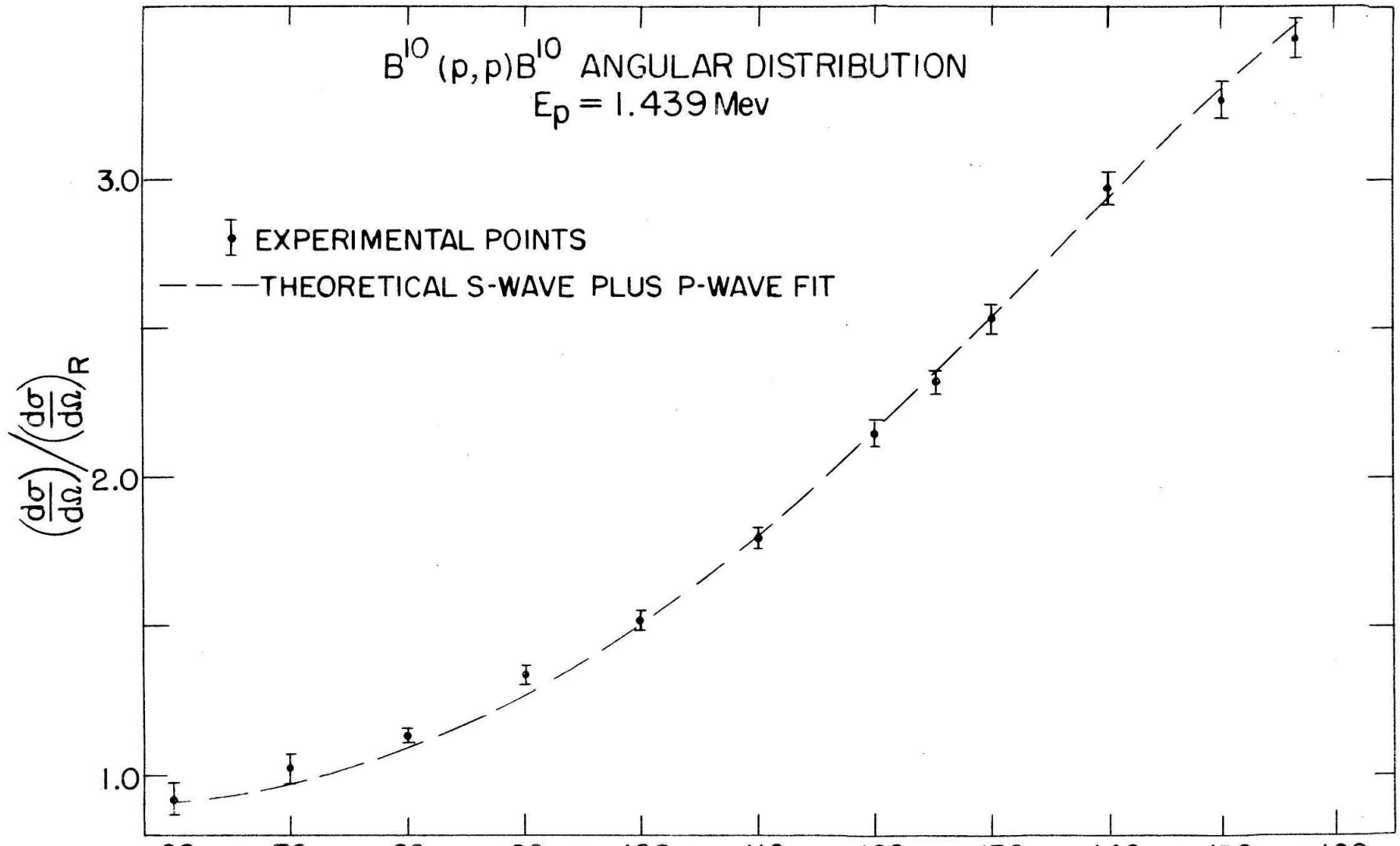
$B^{10}(p,p)B^{10}$ ANGULAR DISTRIBUTION
$E_p = 1.439$ Mev
EXPERIMENTAL POINTS
THEORETICAL S-WAVE PLUS P-WAVE FIT
$\left(\frac{d\sigma}{d\Omega}\right)/\left(\frac{d\sigma}{d\Omega}\right)_R$
3.0
2.0
1.0
60
70
80
90
100
110
120
130
140
150
160
CENTER OF MASS SCATTERING ANGLE (DEGREES)

FIGURE 25

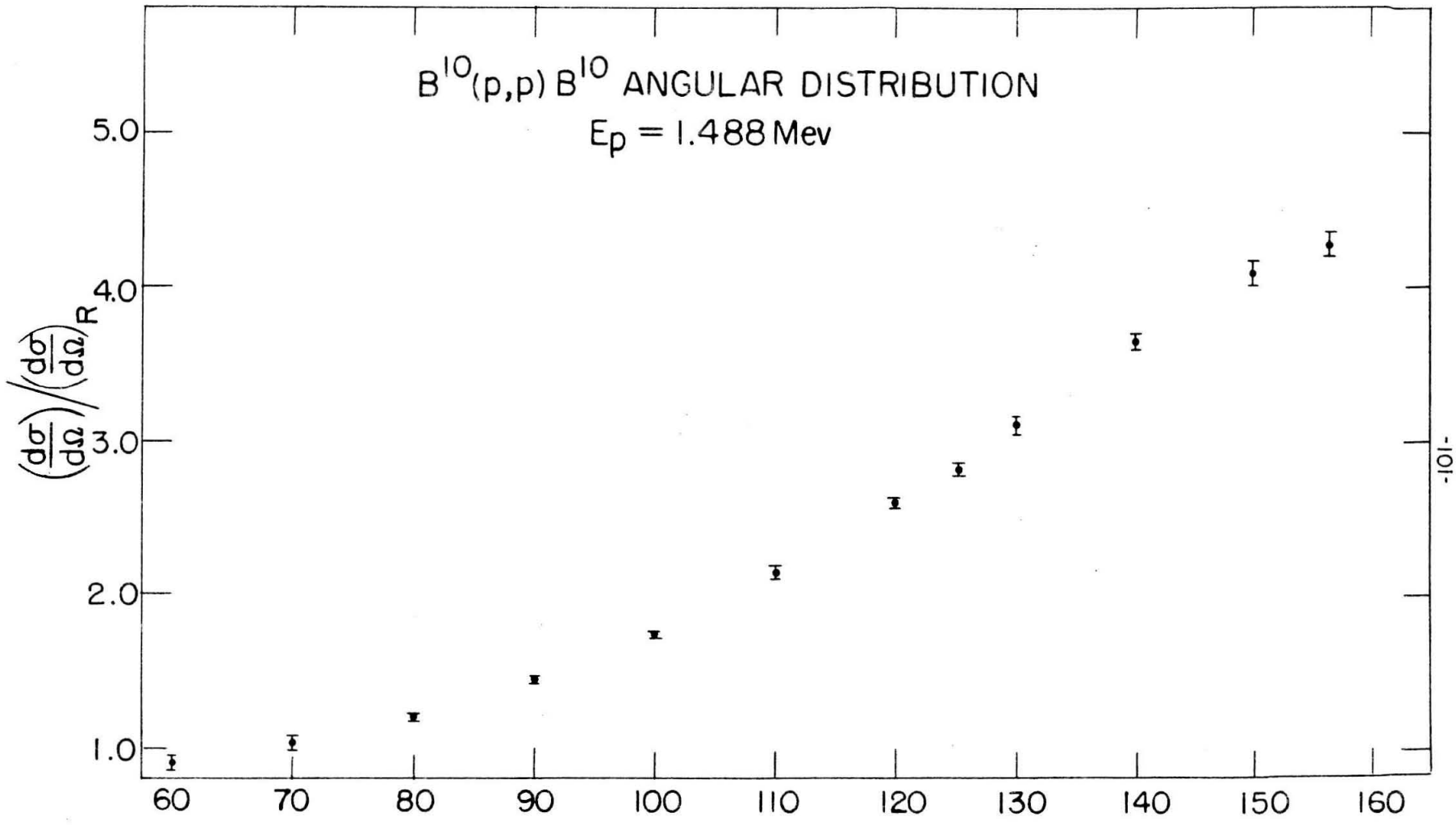
$B^{10}(p,p)\,B^{10}$ ANGULAR DISTRIBUTION
$E_p = 1.488$ Mev
$\left(\frac{d\sigma}{d\Omega}\right)/\left(\frac{d\sigma}{d\Omega}\right)_R$
5.0
4.0
3.0
2.0
1.0
60
70
80
90
100
110
120
130
140
150
160
CENTER OF MASS SCATTERING ANGLE (DEGREES)

FIGURE 26

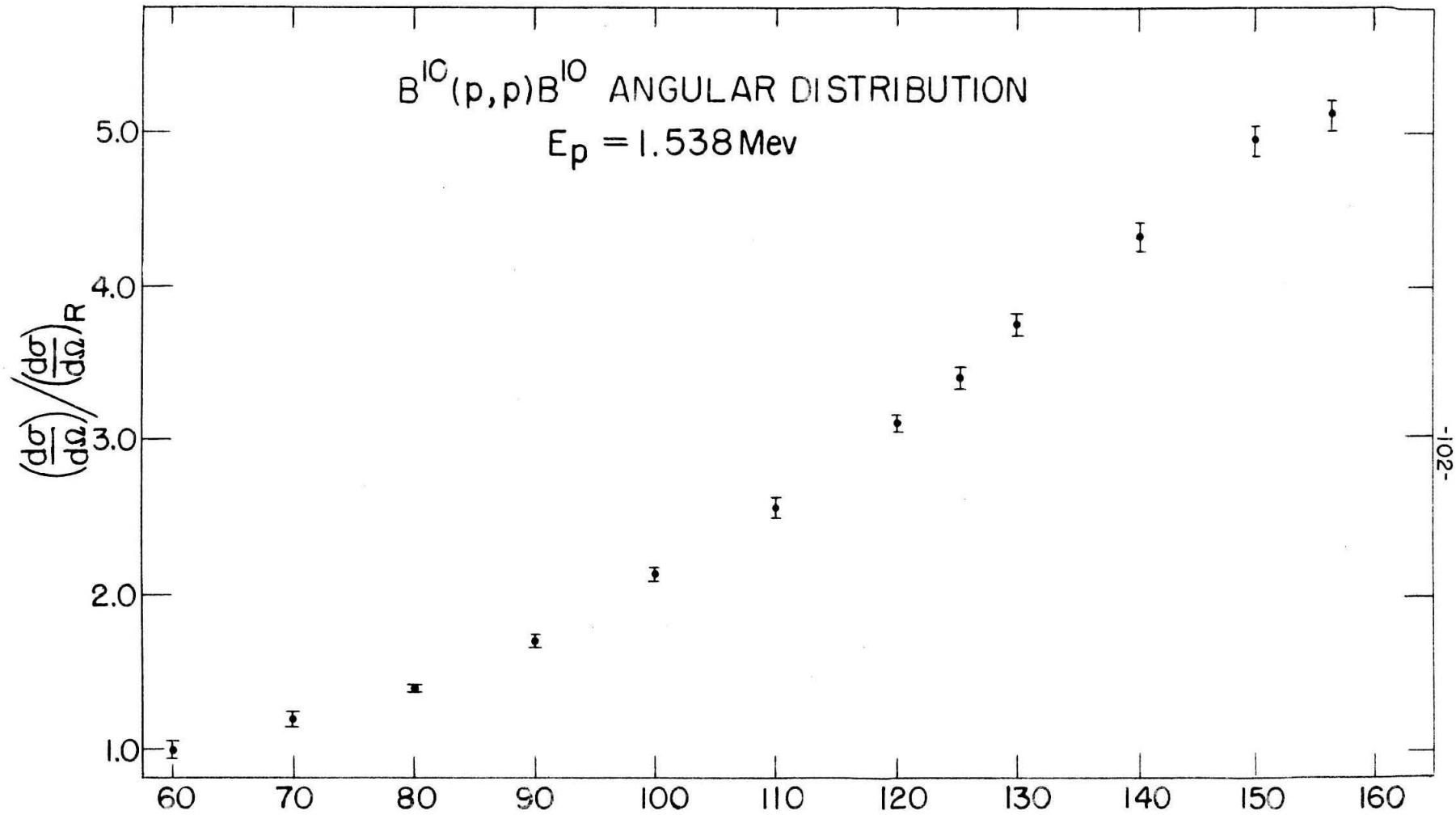
$B^{10}(p,p)B^{10}$ ANGULAR DISTRIBUTION
$E_p = 1.538$ Mev
$\frac{(d\sigma/d\Omega)}{(d\sigma/d\Omega)_R}$
5.0
4.0
3.0
2.0
1.0
60
70
80
90
100
110
120
130
140
150
160
CENTER OF MASS SCATTERING ANGLE (DEGREES)

FIGURE 27

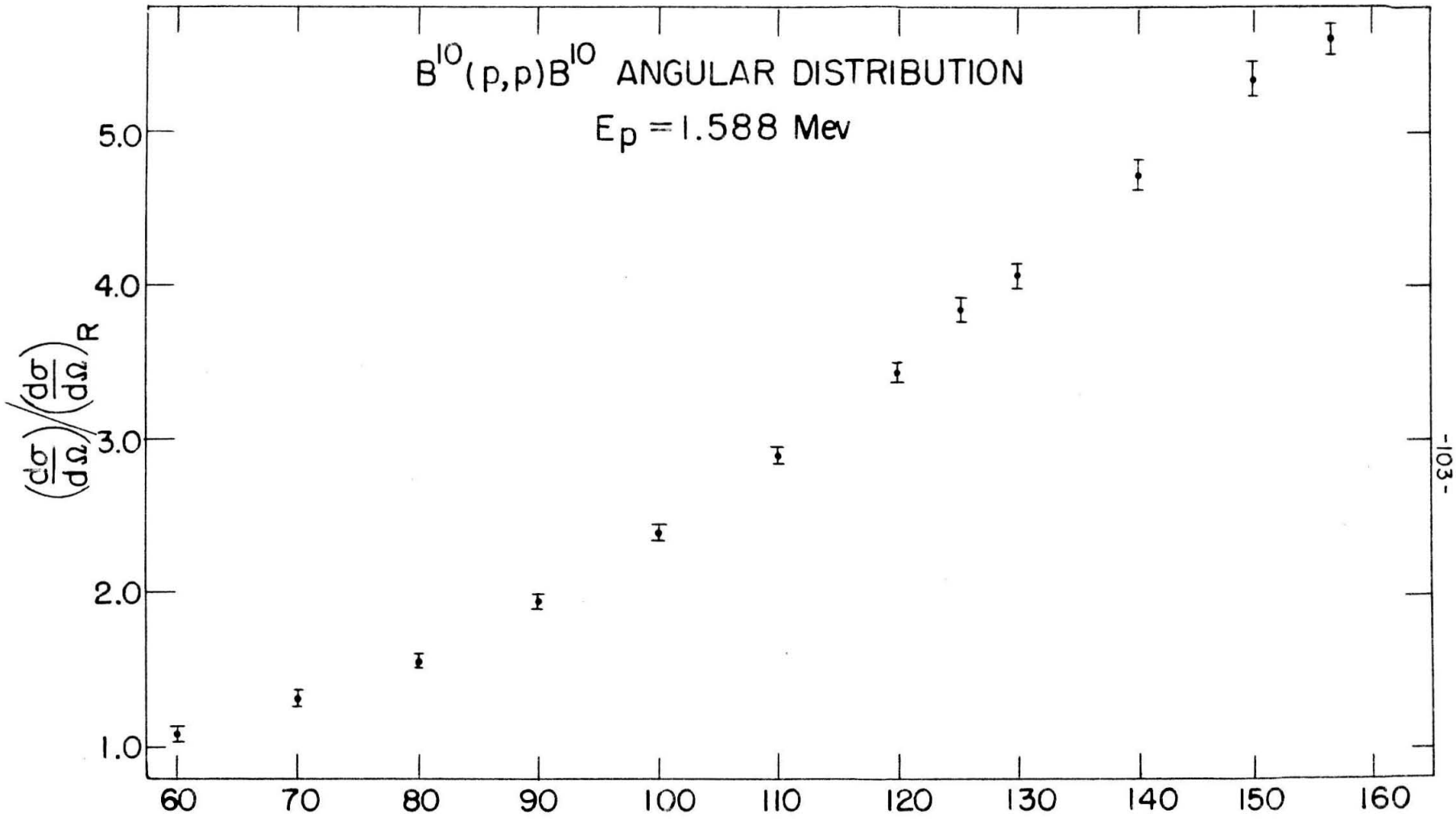
$B^{10}(p,p)B^{10}$ ANGULAR DISTRIBUTION
$E_p = 1.588$ Mev
$\left(\frac{d\sigma}{d\Omega}\right)/\left(\frac{d\sigma}{d\Omega}\right)_R$
5.0
4.0
3.0
2.0
1.0
60
70
80
90
100
110
120
130
140
150
160
CENTER OF MASS SCATTERING ANGLE (DEGREES)

FIGURE 28

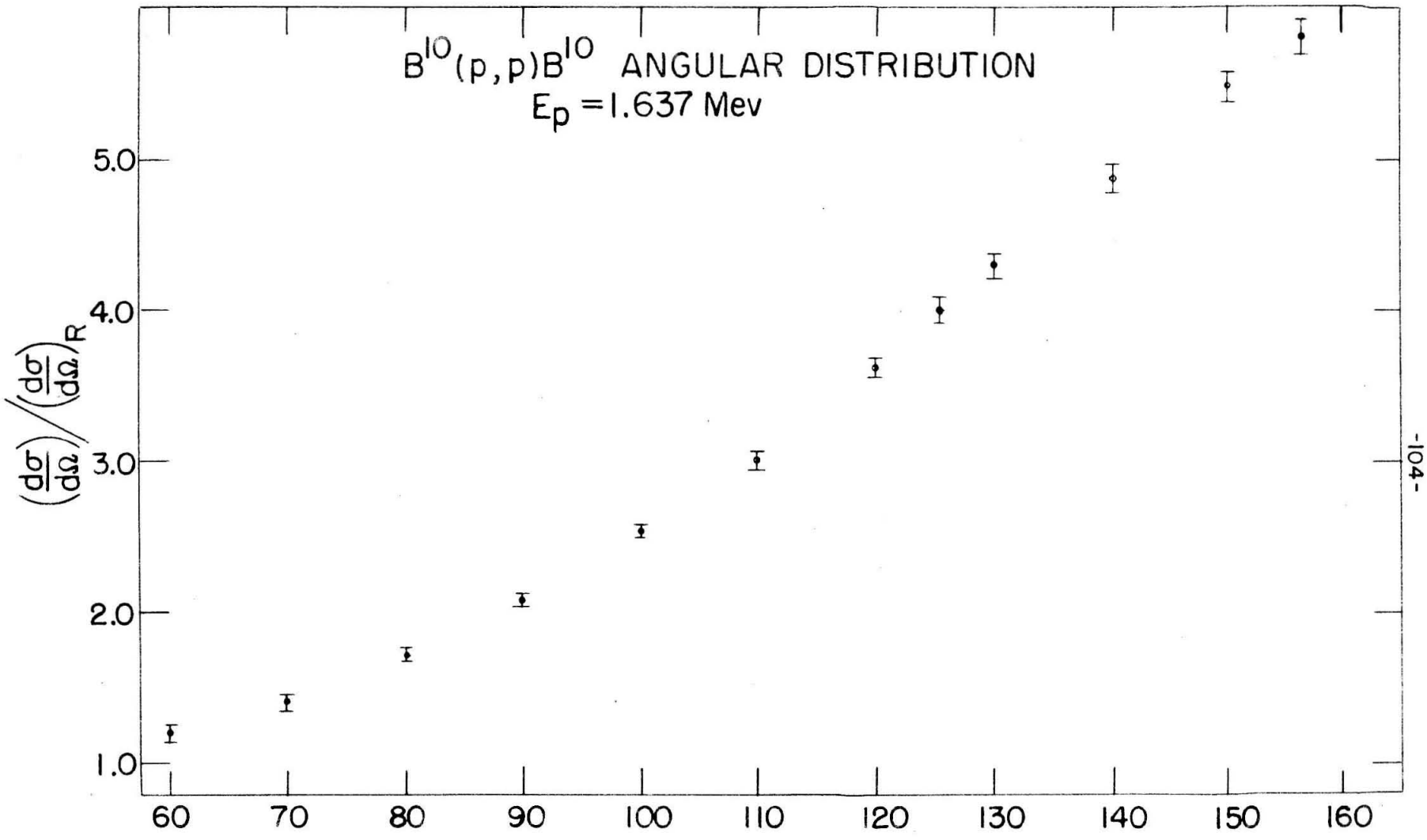
$B^{10}(p,p)B^{10}$ ANGULAR DISTRIBUTION
E_p = 1.637 Mev
$\left(\frac{d\sigma}{d\Omega}\right)/\left(\frac{d\sigma}{d\Omega}\right)_R$
5.0
4.0
3.0
2.0
1.0
60
70
80
90
100
110
120
130
140
150
160
CENTER OF MASS SCATTERING ANGLE (DEGREES)

FIGURE 29

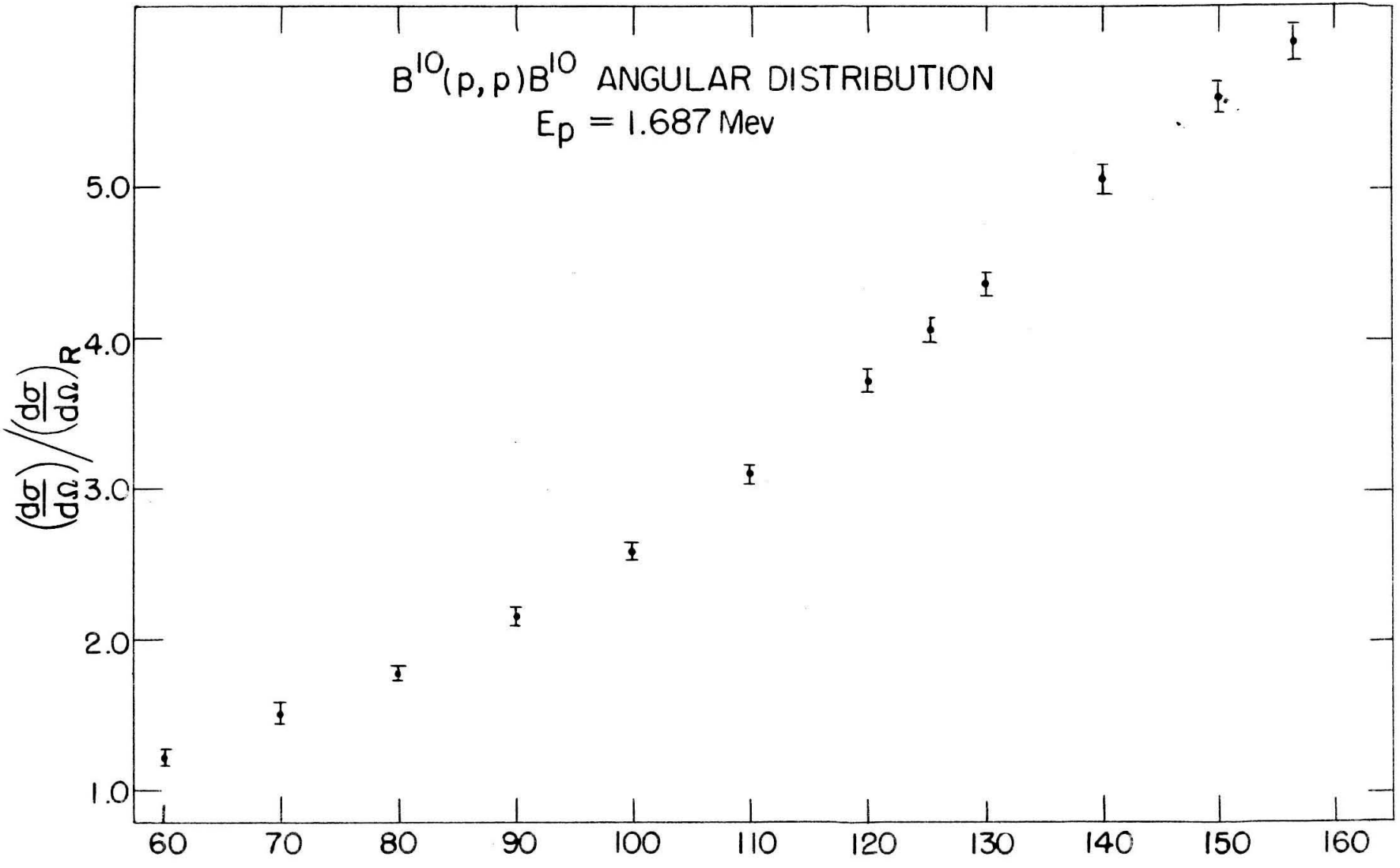
$B^{10}(p,p)B^{10}$ ANGULAR DISTRIBUTION
E_p = 1.687 Mev
$\left(\frac{d\sigma}{d\Omega}\right)/\left(\frac{d\sigma}{d\Omega}\right)_R$
5.0
4.0
3.0
2.0
1.0
60
70
80
90
100
110
120
130
140
150
160
CENTER OF MASS SCATTERING ANGLE (DEGREES)

FIGURE 30

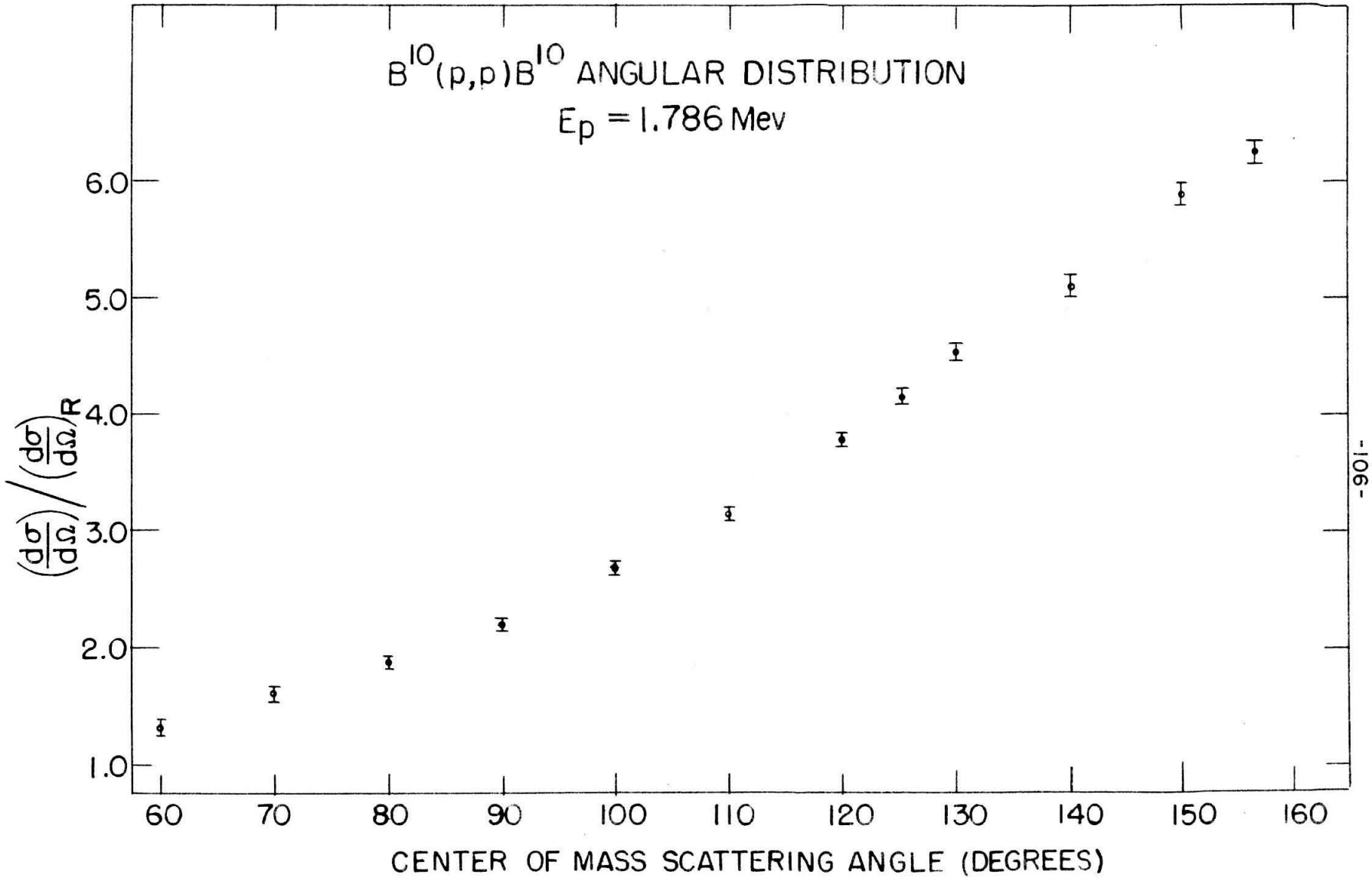
$B^{10}(p,p)B^{10}$ ANGULAR DISTRIBUTION
$E_p = 1.786$ Mev
$\left(\frac{d\sigma}{d\Omega}\right) / \left(\frac{d\sigma}{d\Omega}\right)_R$
6.0
5.0
4.0
3.0
2.0
1.0
60
70
80
90
100
110
120
130
140
150
160
CENTER OF MASS SCATTERING ANGLE (DEGREES)

FIGURE 31

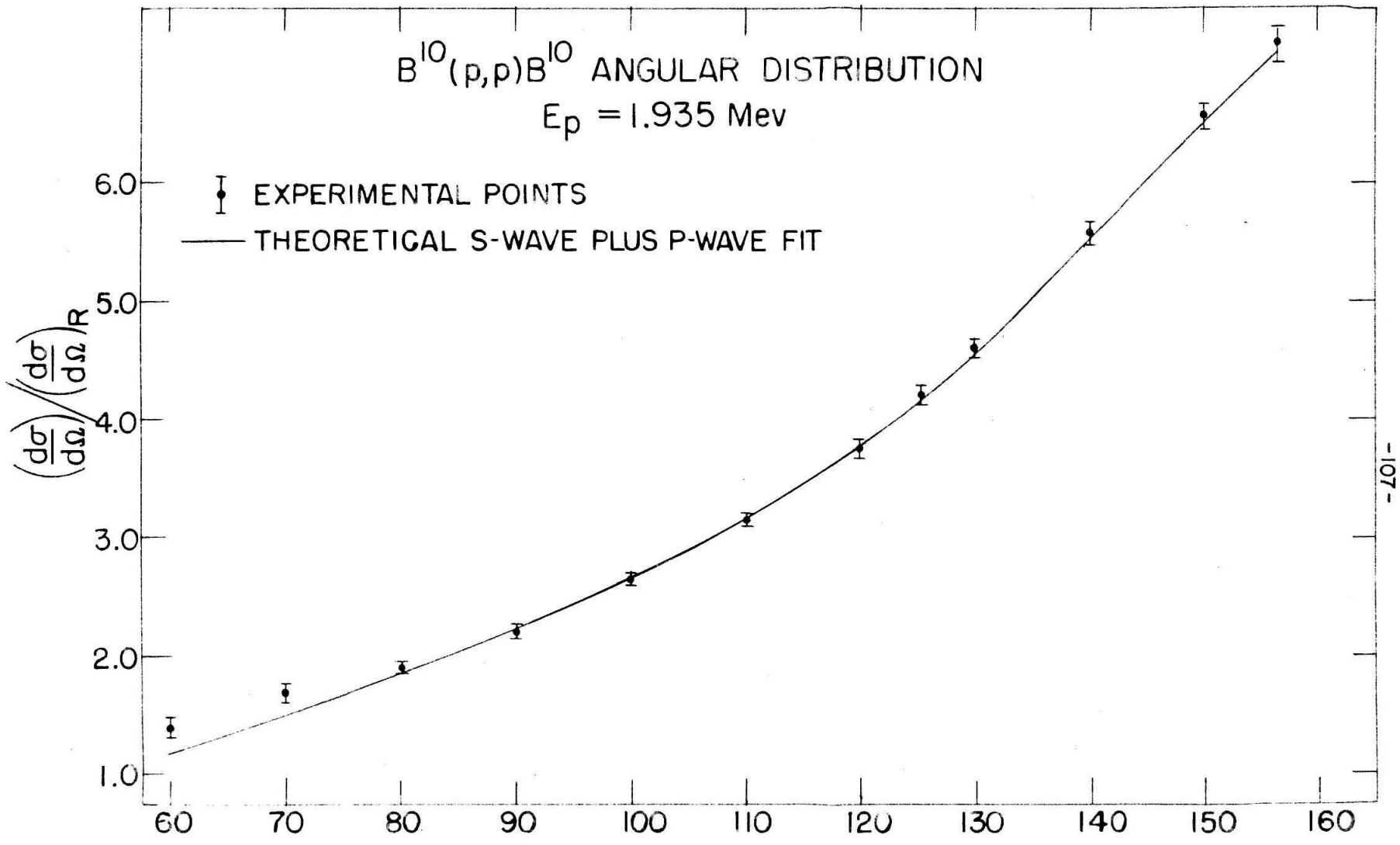
$B^{10}(p,p)B^{10}$ ANGULAR DISTRIBUTION
E_p = 1.935 Mev
EXPERIMENTAL POINTS
THEORETICAL S-WAVE PLUS P-WAVE FIT
$\left(\frac{d\sigma}{d\Omega}\right)/\left(\frac{d\sigma}{d\Omega}\right)_R$
6.0
5.0
4.0
3.0
2.0
1.0
60
70
80
90
100
110
120
130
140
150
160
CENTER OF MASS SCATTERING ANGLE (DEGREES)

FIGURE 32

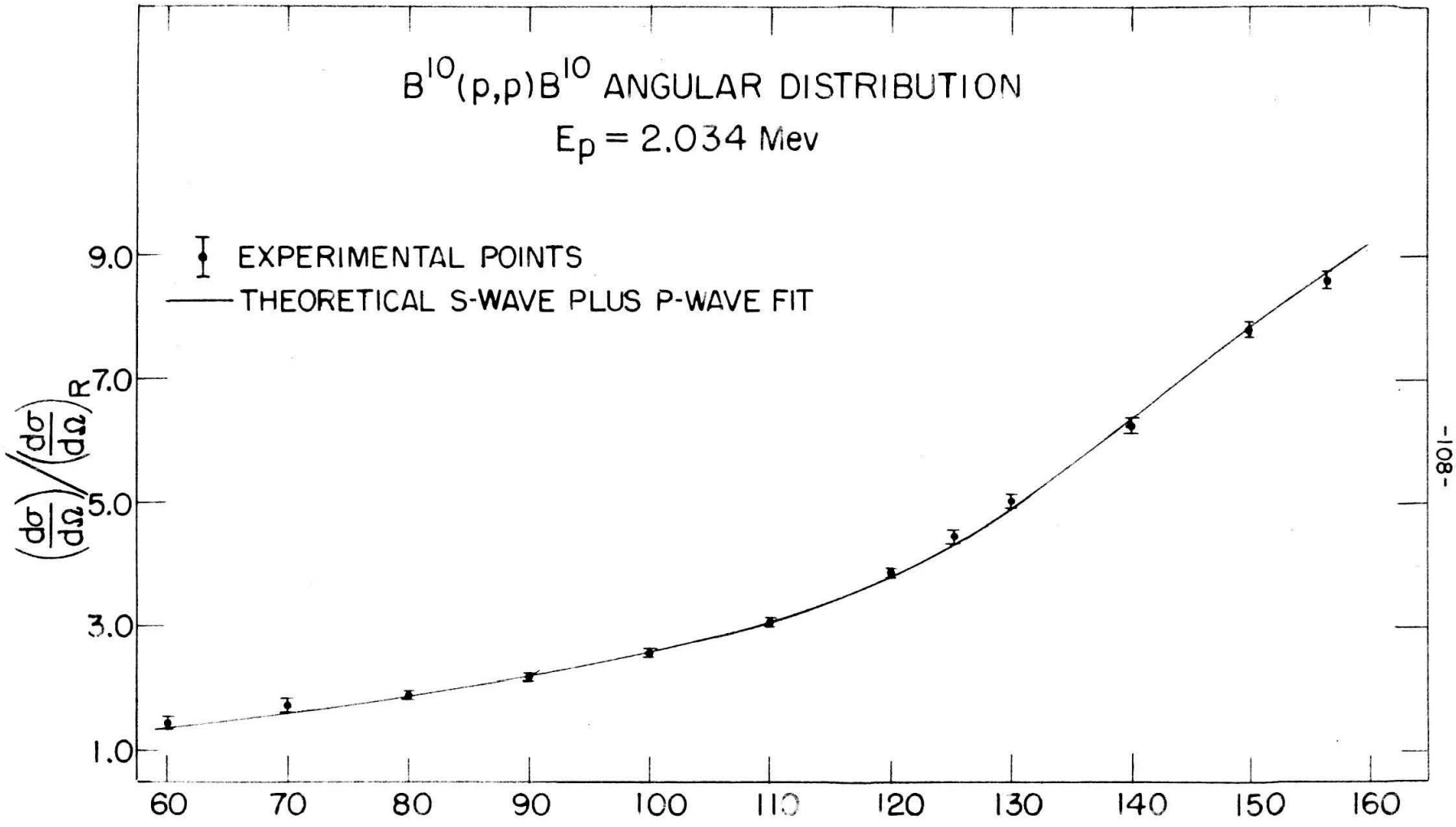
$B^{10}(p,p)B^{10}$ ANGULAR DISTRIBUTION
$E_p = 2.034$ Mev
EXPERIMENTAL POINTS
THEORETICAL S-WAVE PLUS P-WAVE FIT
$\left(\frac{d\sigma}{d\Omega}\right)/\left(\frac{d\sigma}{d\Omega}\right)_R$
9.0
7.0
5.0
3.0
1.0
60
70
80
90
100
110
120
130
140
150
160
CENTER OF MASS SCATTERING ANGLE (DEGREES)

FIGURE 33

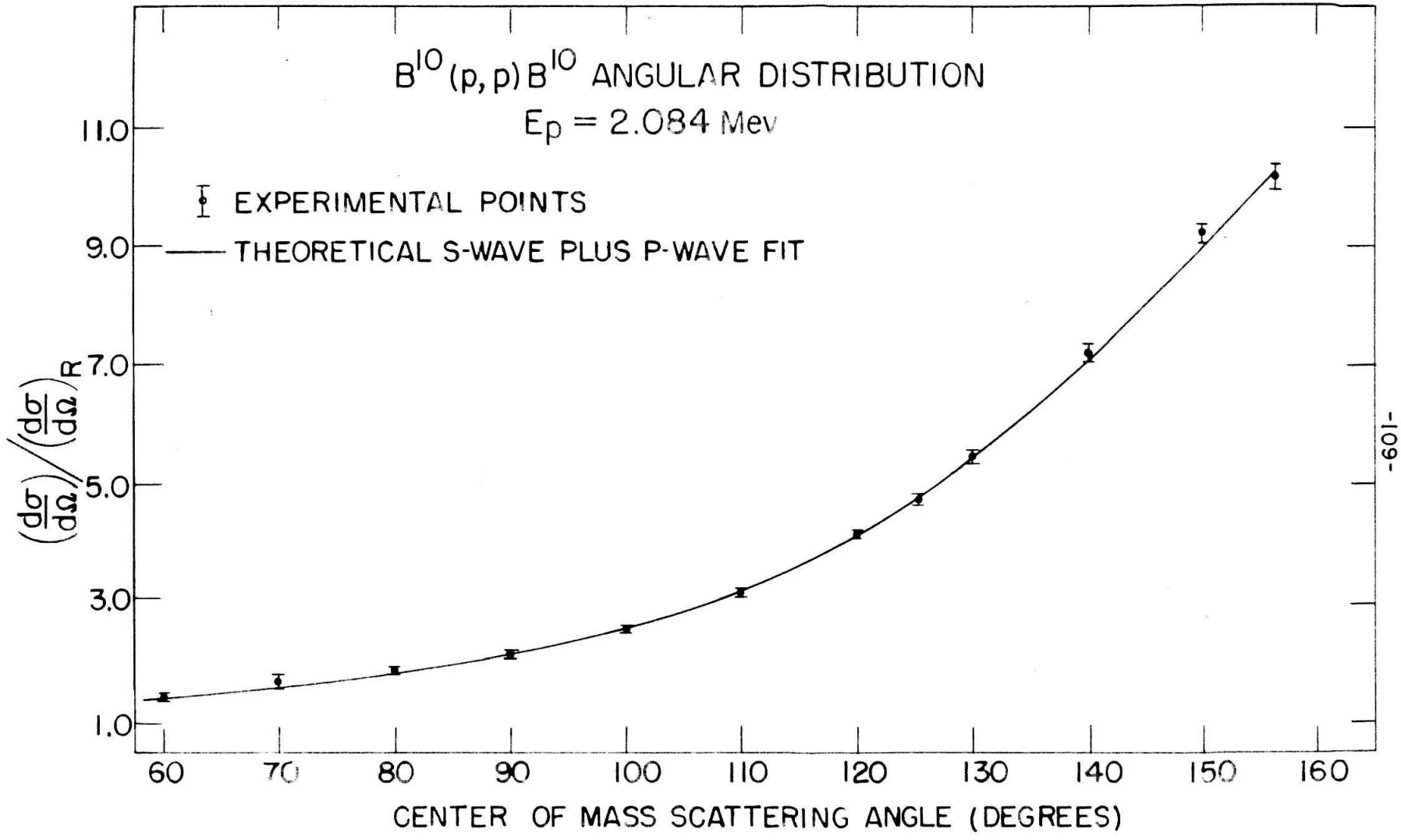
$B^{10}(p,p)B^{10}$ ANGULAR DISTRIBUTION
$E_p = 2.084$ Mev
EXPERIMENTAL POINTS
THEORETICAL S-WAVE PLUS P-WAVE FIT
$\left(\frac{d\sigma}{d\Omega}\right)/\left(\frac{d\sigma}{d\Omega}\right)_R$
11.0
9.0
7.0
5.0
3.0
1.0
60
70
80
90
100
110
120
130
140
150
160
CENTER OF MASS SCATTERING ANGLE (DEGREES)

FIGURE 34

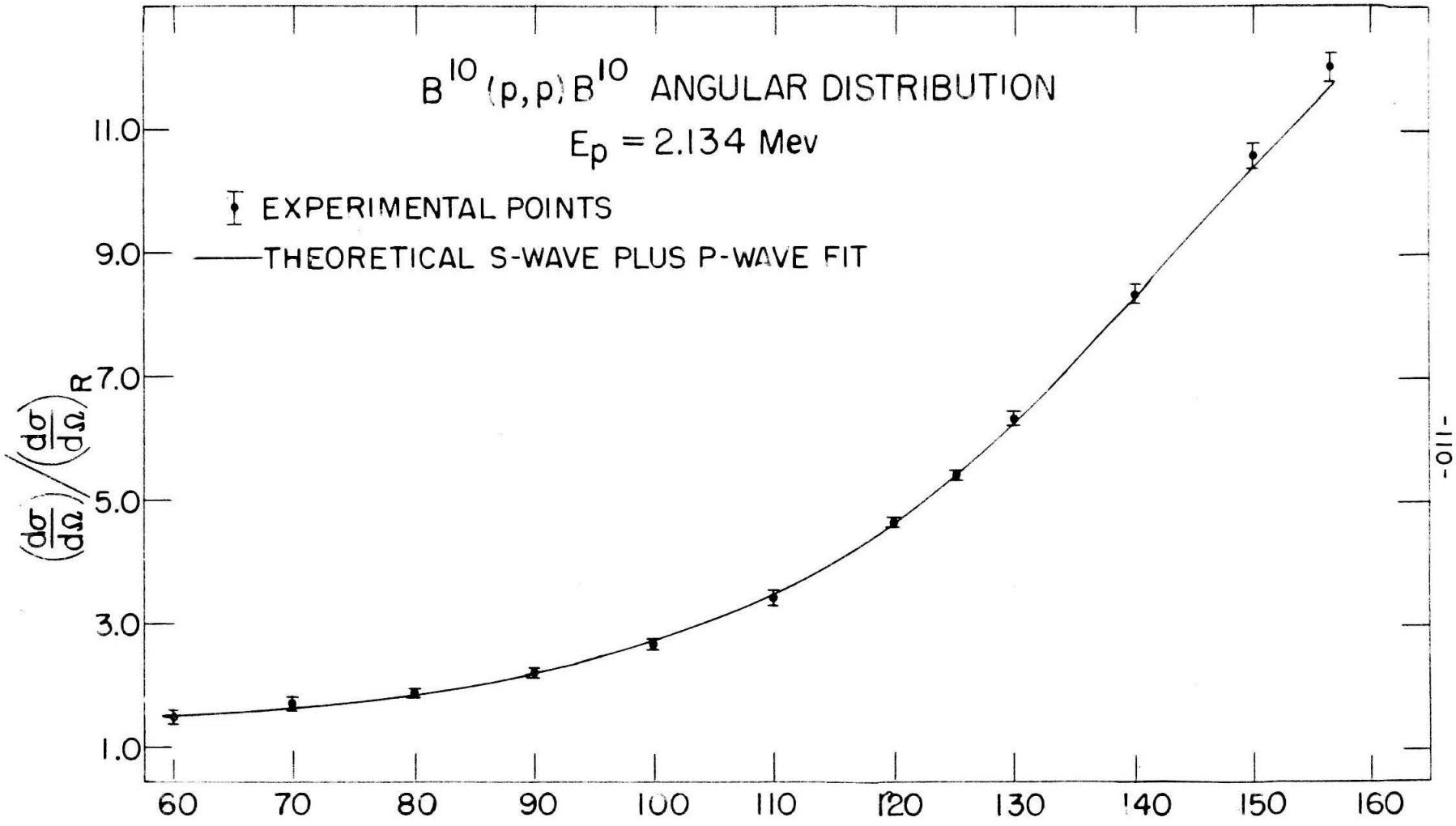
$B^{10}(p,p)B^{10}$ ANGULAR DISTRIBUTION
$E_p = 2.134$ Mev
EXPERIMENTAL POINTS
THEORETICAL S-WAVE PLUS P-WAVE FIT
$\left(\frac{d\sigma}{d\Omega}\right)/\left(\frac{d\sigma}{d\Omega}\right)_R$
11.0
9.0
7.0
5.0
3.0
1.0
60
70
80
90
100
110
120
130
140
150
160
CENTER OF MASS SCATTERING ANGLE (DEGREES)

FIGURE 35

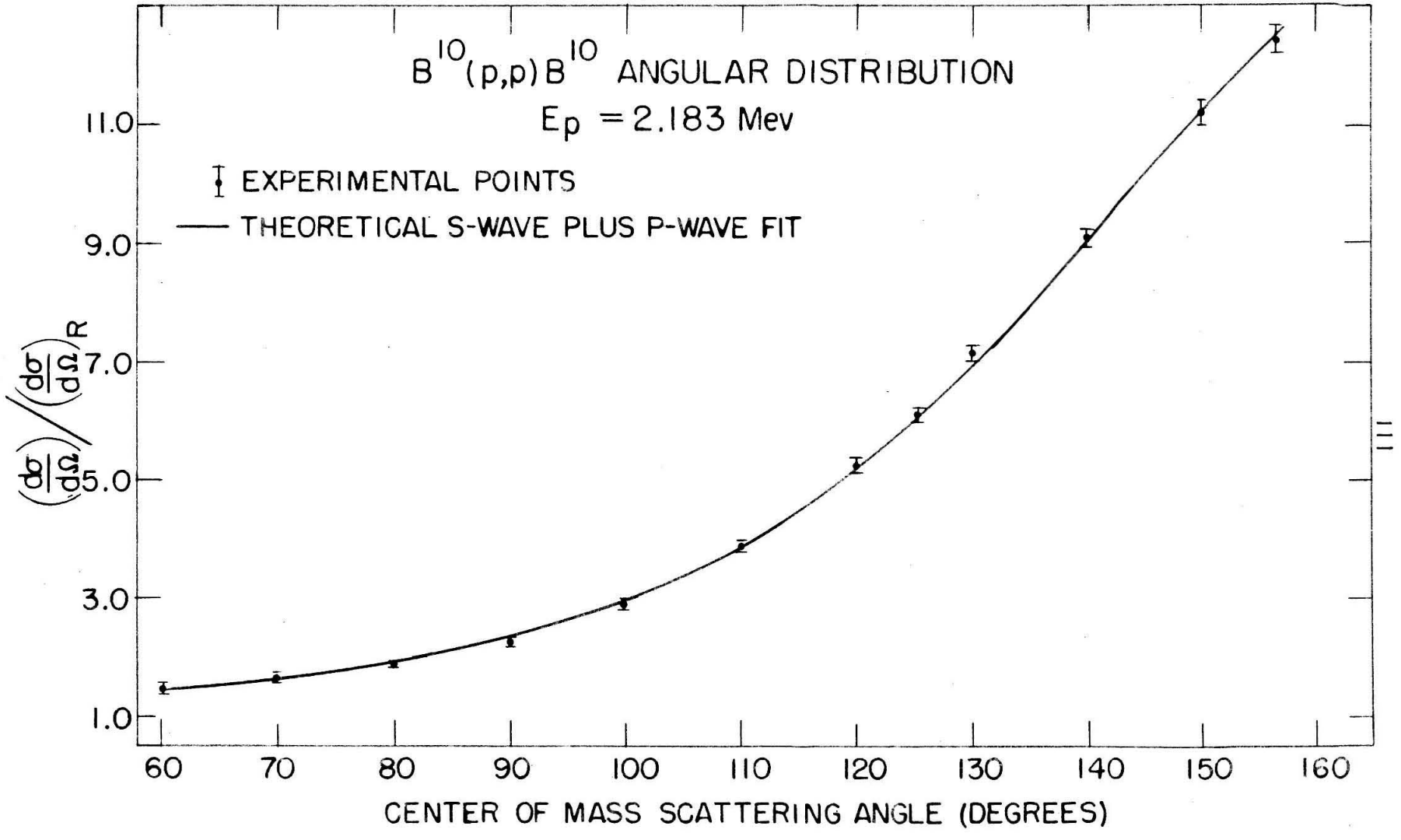
$B^{10}(p,p)B^{10}$ ANGULAR DISTRIBUTION
$E_p = 2.183$ Mev
EXPERIMENTAL POINTS
THEORETICAL S-WAVE PLUS P-WAVE FIT
$\left(\frac{d\sigma}{d\Omega}\right) / \left(\frac{d\sigma}{d\Omega}\right)_R$
11.0
9.0
7.0
5.0
3.0
1.0
60
70
80
90
100
110
120
130
140
150
160
CENTER OF MASS SCATTERING ANGLE (DEGREES)

FIGURE 36

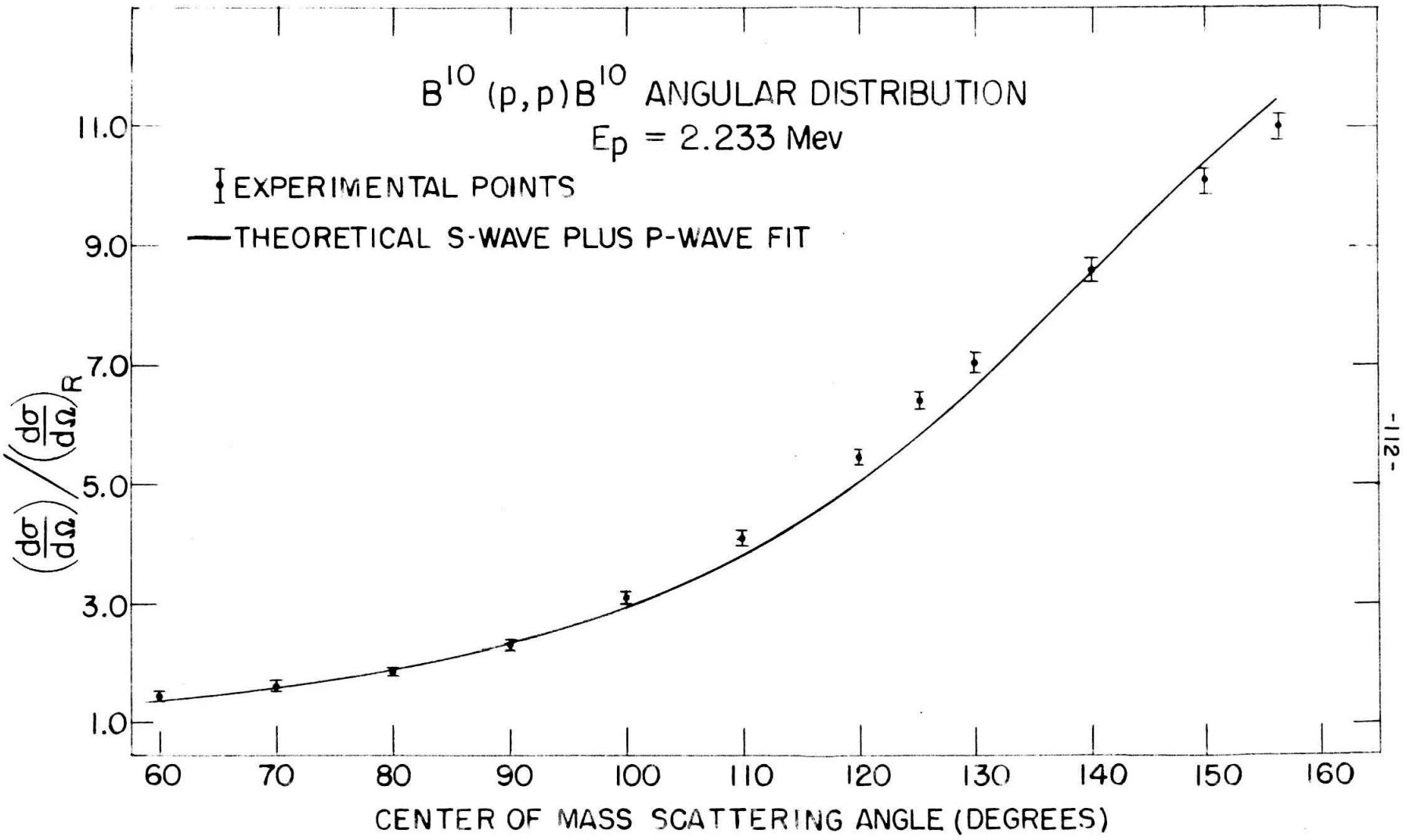
$B^{10}(p,p)B^{10}$ ANGULAR DISTRIBUTION
E_p = 2.233 Mev
EXPERIMENTAL POINTS
THEORETICAL S-WAVE PLUS P-WAVE FIT
$\left(\frac{d\sigma}{d\Omega}\right) / \left(\frac{d\sigma}{d\Omega}\right)_R$
11.0
9.0
7.0
5.0
3.0
1.0
60
70
80
90
100
110
120
130
140
150
160
CENTER OF MASS SCATTERING ANGLE (DEGREES)

FIGURE 37

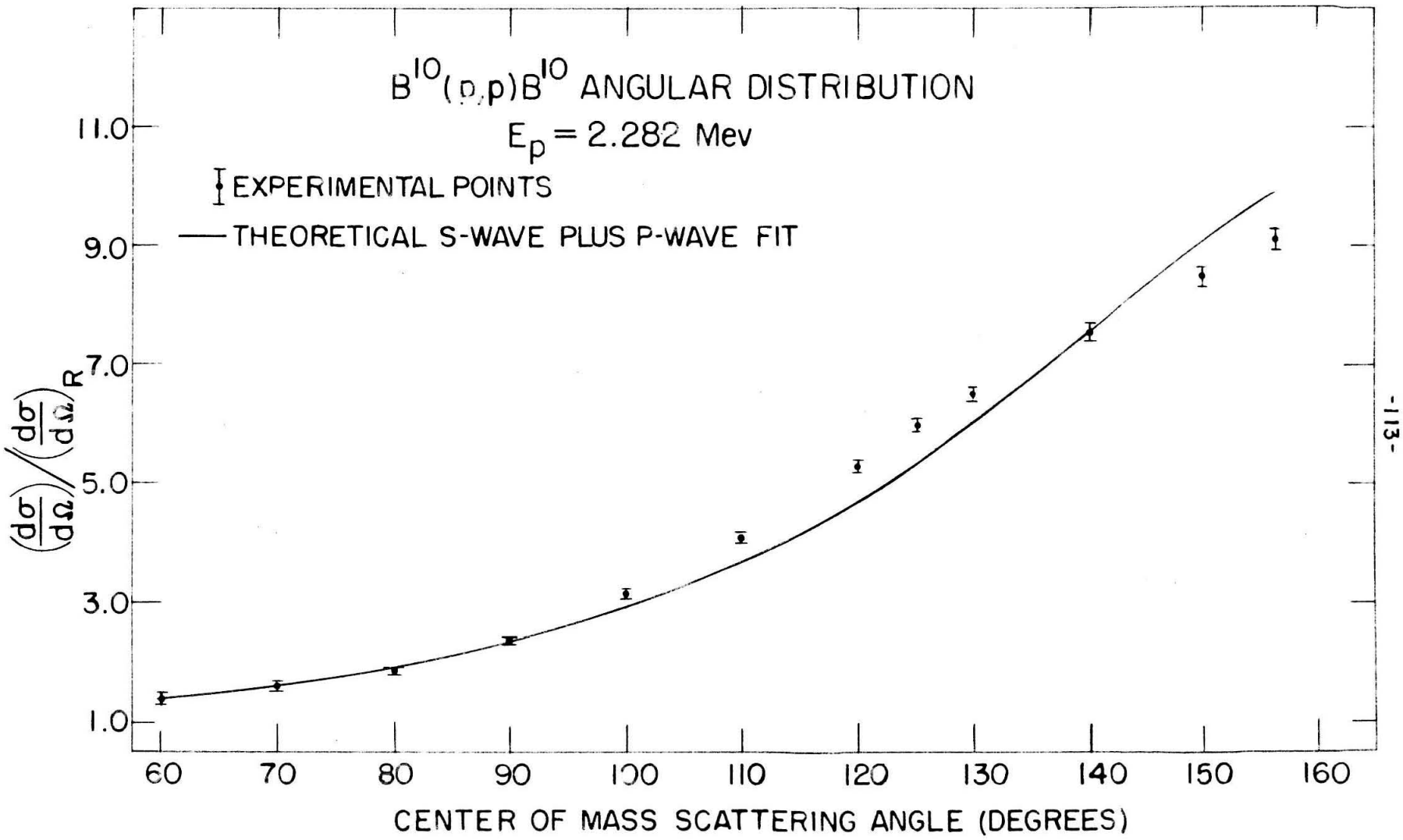
$B^{10}(p,p)B^{10}$ ANGULAR DISTRIBUTION
$E_p = 2.282$ Mev
EXPERIMENTAL POINTS
THEORETICAL S-WAVE PLUS P-WAVE FIT
$\left(\frac{d\sigma}{d\Omega}\right)/\left(\frac{d\sigma}{d\Omega}\right)_R$
11.0
9.0
7.0
5.0
3.0
1.0
60
70
80
90
100
110
120
130
140
150
160
CENTER OF MASS SCATTERING ANGLE (DEGREES)

FIGURE 38

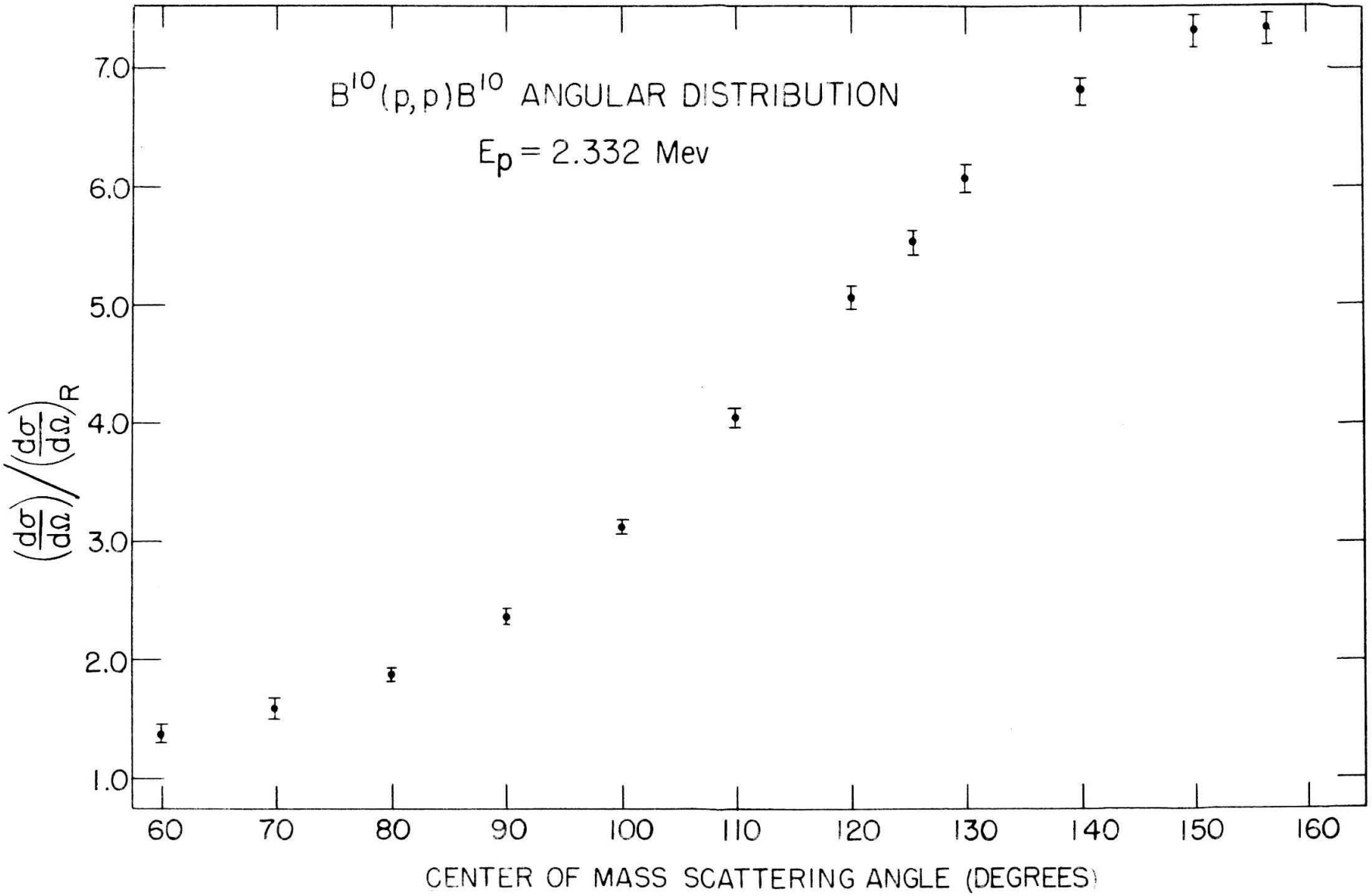
$B^{10}(p,p)B^{10}$ ANGULAR DISTRIBUTION
$E_p = 2.332$ Mev
$\left(\frac{d\sigma}{d\Omega}\right)/\left(\frac{d\sigma}{d\Omega}\right)_R$
7.0
6.0
5.0
4.0
3.0
2.0
1.0
60
70
80
90
100
110
120
130
140
150
160
CENTER OF MASS SCATTERING ANGLE (DEGREES)

FIGURE 39

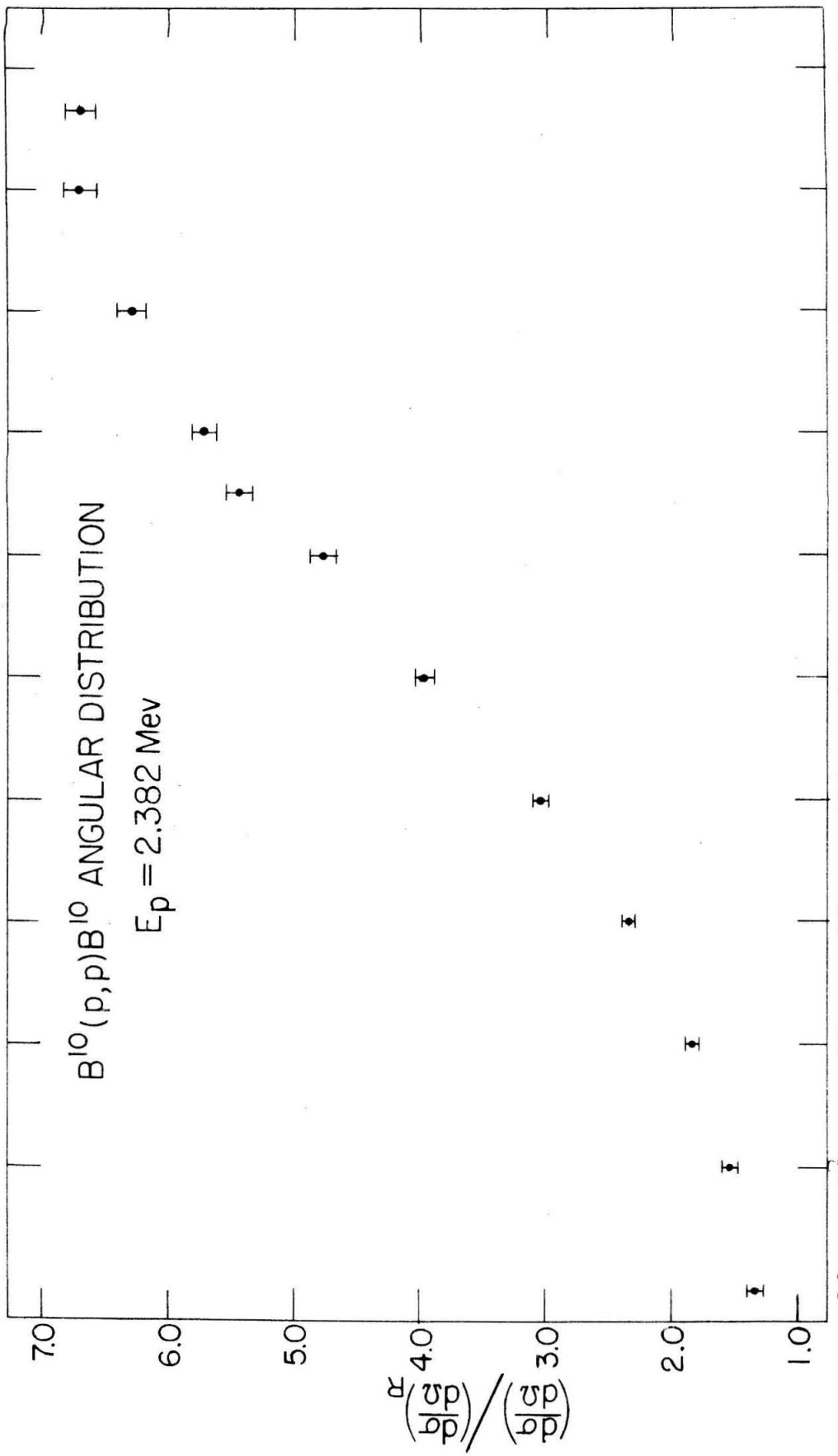
$B^{10}(p,p)B^{10}$ ANGULAR DISTRIBUTION
$E_p = 2.382$ Mev
$\left(\frac{d\sigma}{d\Omega}\right) / \left(\frac{d\sigma}{d\Omega}\right)_R$
7.0
6.0
5.0
4.0
3.0
2.0
1.0
60
70
80
90
100
110
120
130
140
150
160
CENTER OF MASS SCATTERING ANGLE (DEGREES)

FIGURE 40

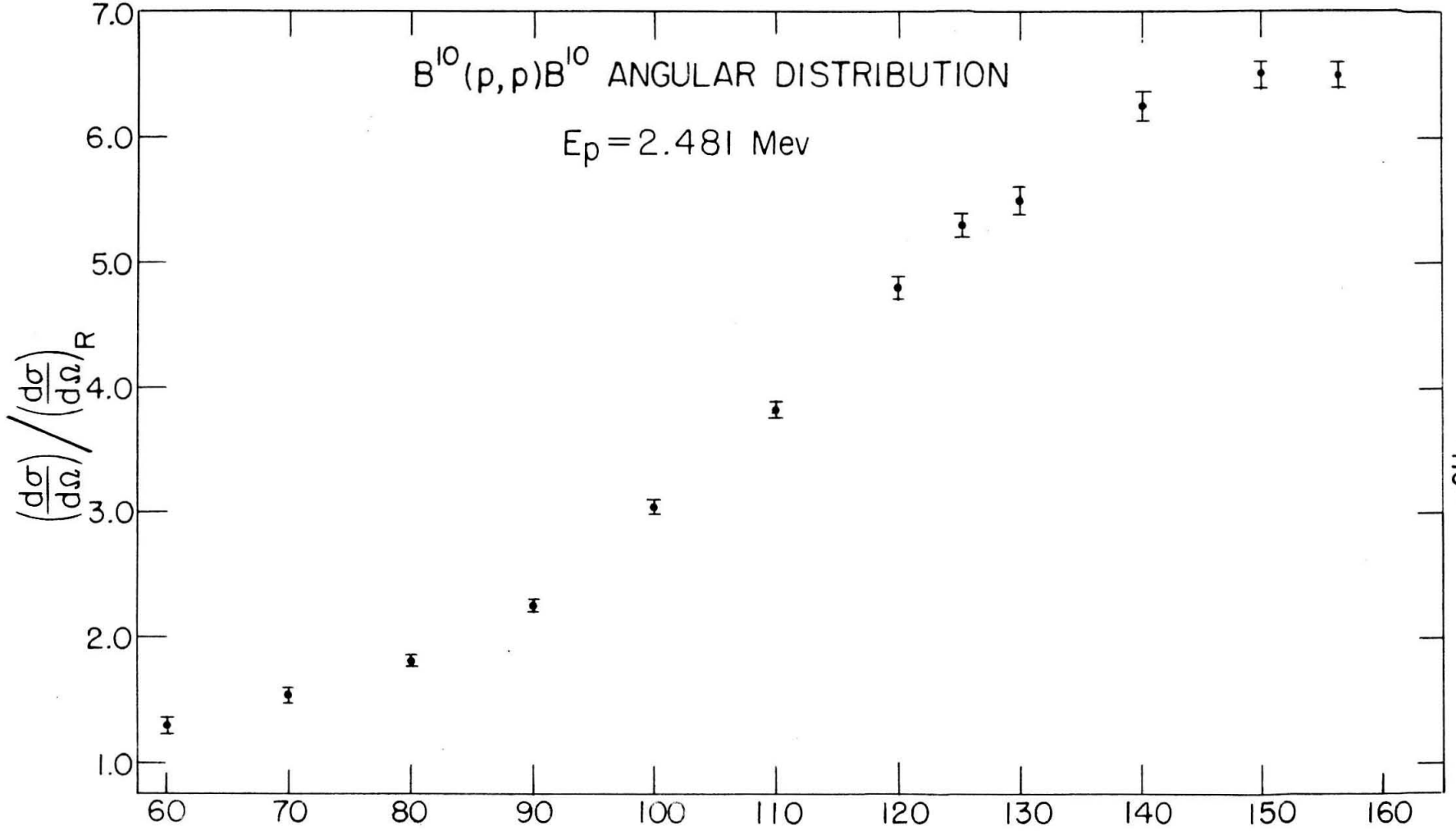
$B^{10}(p,p)B^{10}$ ANGULAR DISTRIBUTION
$E_p = 2.481$ Mev
$\left(\frac{d\sigma}{d\Omega}\right) / \left(\frac{d\sigma}{d\Omega}\right)_R$
7.0
6.0
5.0
4.0
3.0
2.0
1.0
60
70
80
90
100
110
120
130
140
150
160
CENTER OF MASS SCATTERING ANGLE (DEGREES)

FIGURE 41

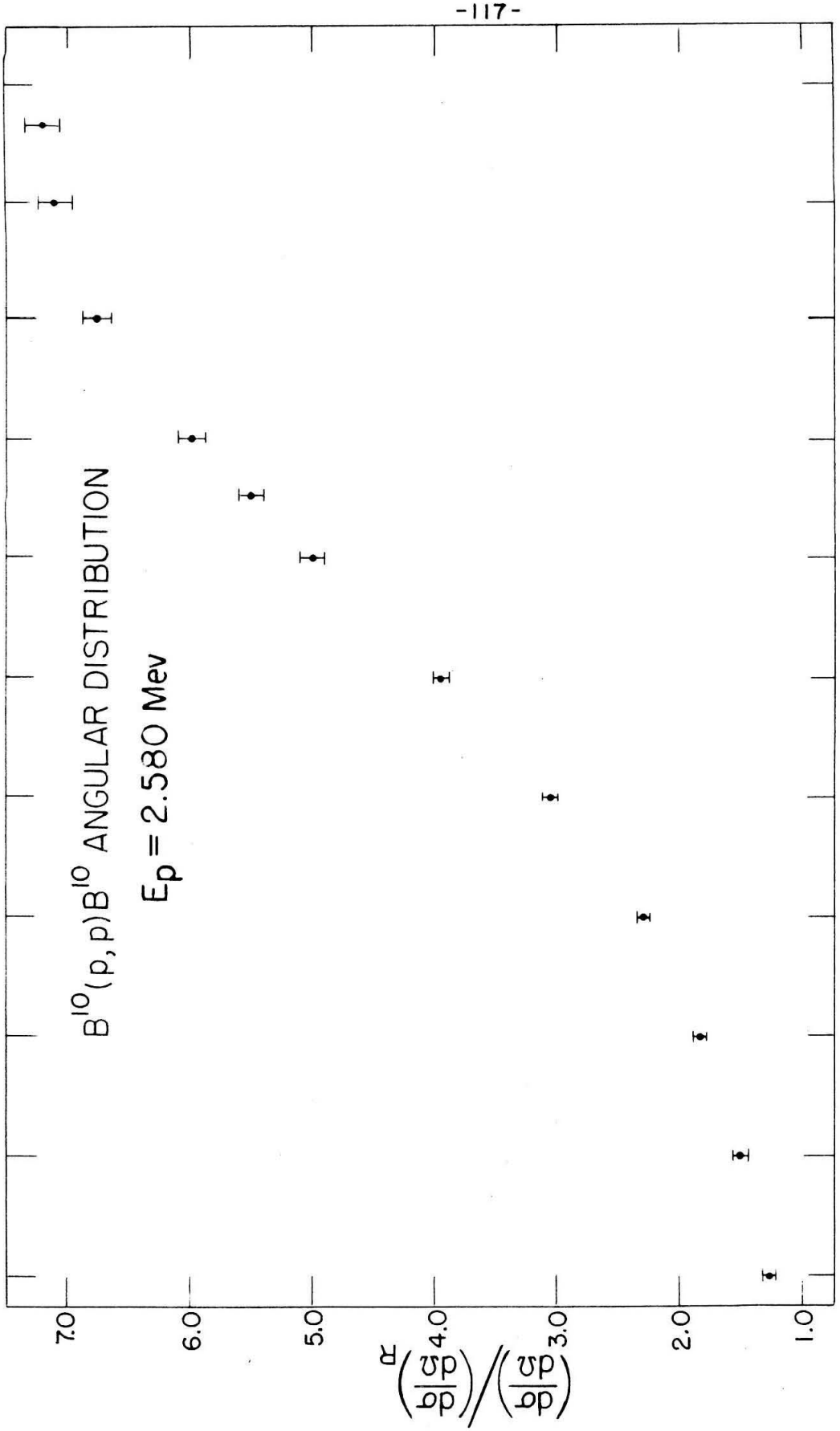
$B^{10}(p,p)B^{10}$ ANGULAR DISTRIBUTION
$E_p = 2.580$ Mev
$\left(\frac{d\sigma}{d\Omega}\right) / \left(\frac{d\sigma}{d\Omega}\right)_R$
7.0
6.0
5.0
4.0
3.0
2.0
1.0
60
70
80
90
100
110
120
130
140
150
160
CENTER OF MASS SCATTERING ANGLE (DEGREES)

FIGURE 42

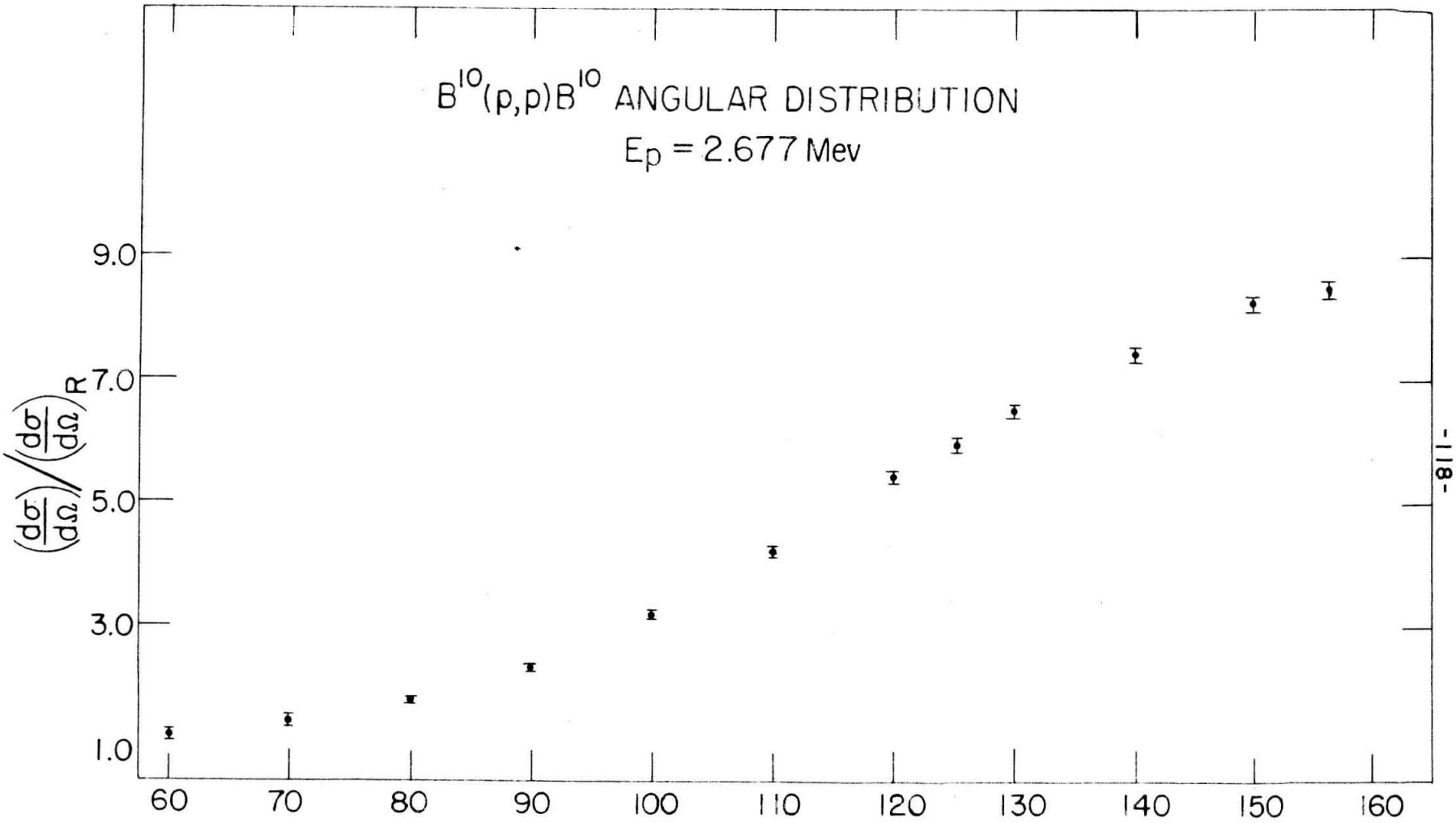
$B^{10}(p,p)B^{10}$ ANGULAR DISTRIBUTION
$E_p = 2.677$ Mev
$\left(\frac{d\sigma}{d\Omega}\right)/\left(\frac{d\sigma}{d\Omega}\right)_R$
9.0
7.0
5.0
3.0
1.0
60
70
80
90
100
110
120
130
140
150
160
CENTER OF MASS SCATTERING ANGLE (DEGREES)

FIGURE 43

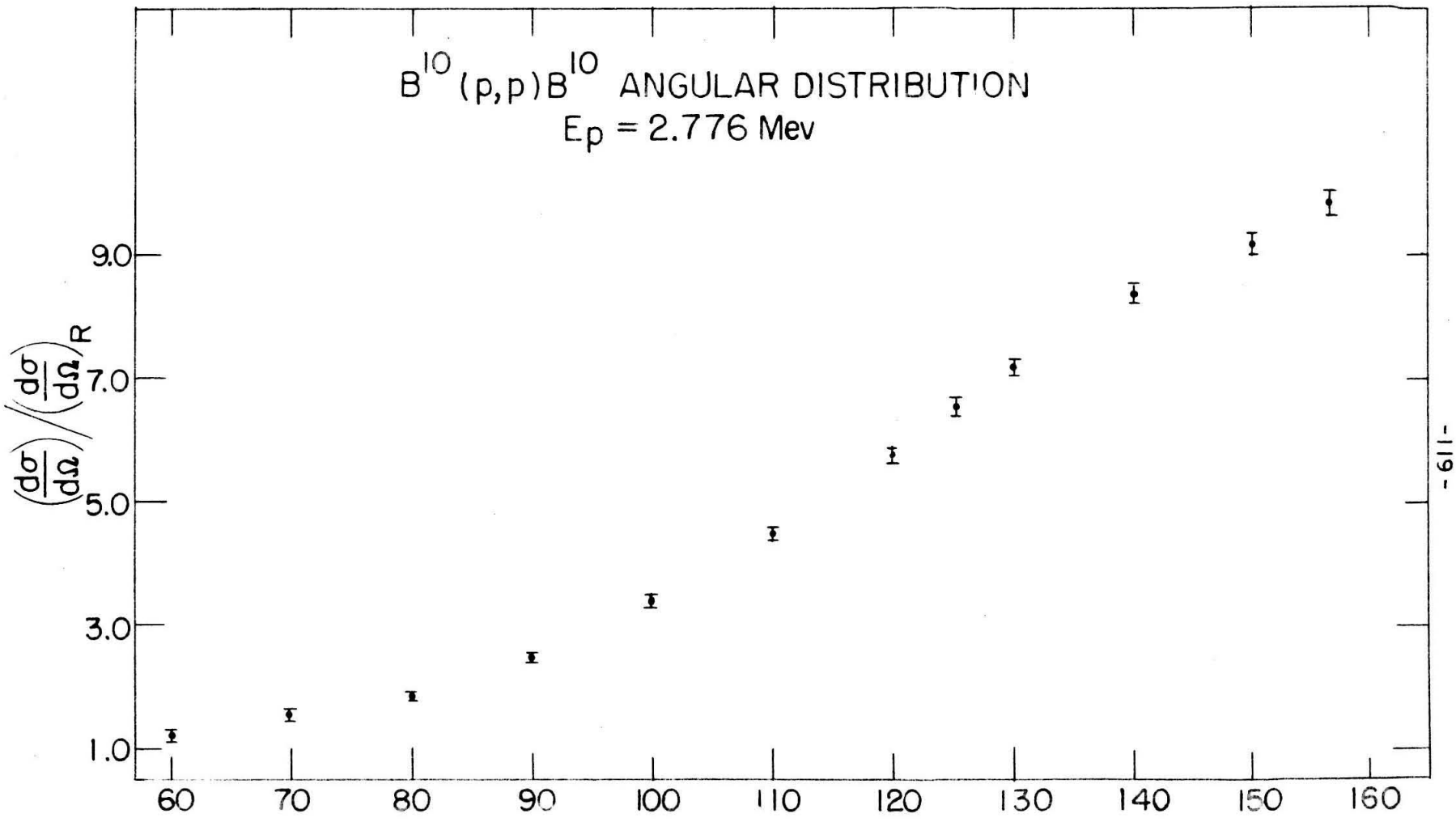
$B^{10}(p,p)B^{10}$ ANGULAR DISTRIBUTION
$E_p = 2.776$ Mev
$\left(\frac{d\sigma}{d\Omega}\right) / \left(\frac{d\sigma}{d\Omega}\right)_R$
9.0
7.0
5.0
3.0
1.0
60
70
80
90
100
110
120
130
140
150
160
CENTER OF MASS SCATTERING ANGLE (DEGREES)

FIGURE 44

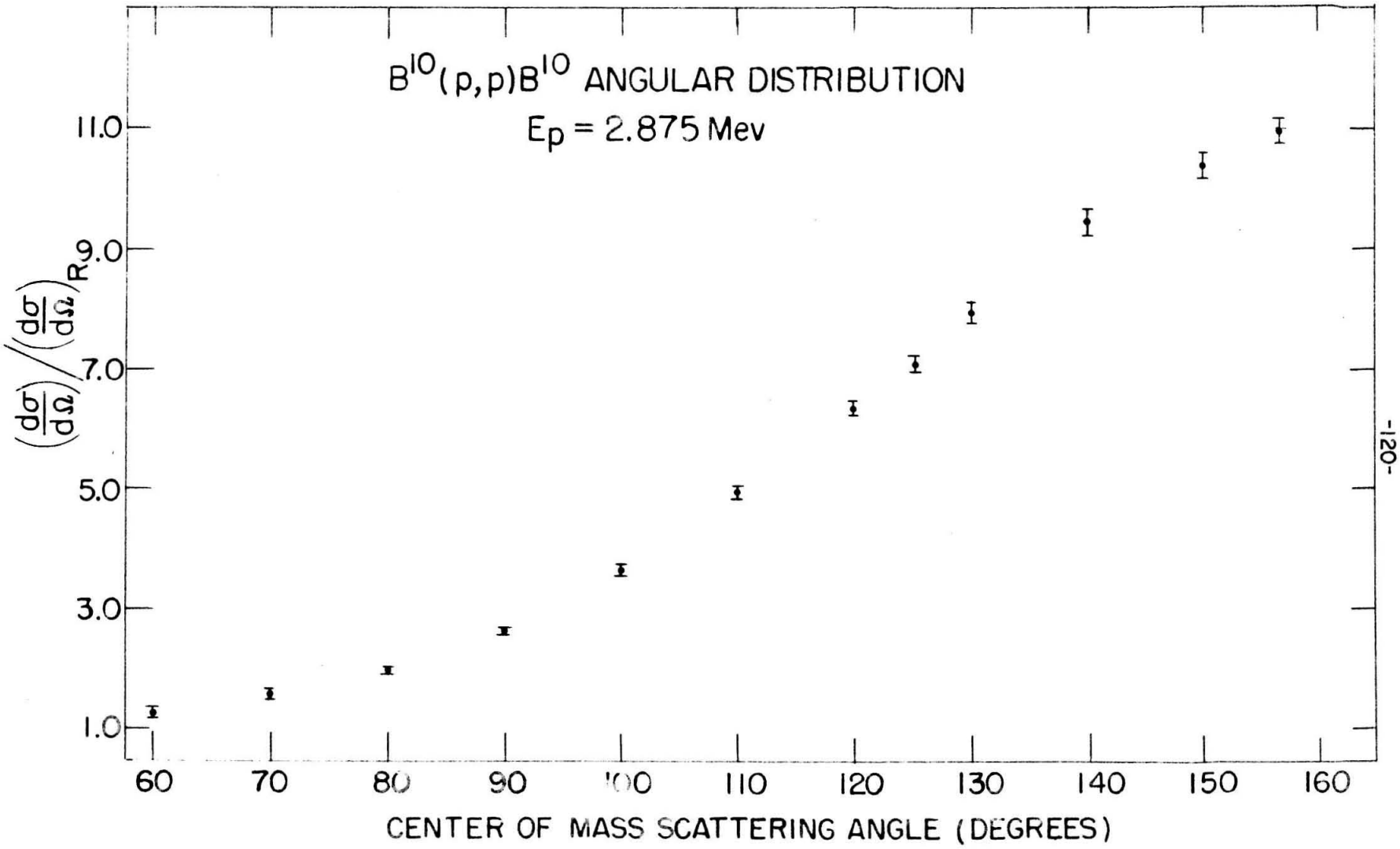
B10(p,p)B10 ANGULAR DISTRIBUTION
Ep = 2.875 Mev
(dσ/dΩ)/(dσ/dΩ)R
11.0
9.0
7.0
5.0
3.0
1.0
60
70
80
90
100
110
120
130
140
150
160
CENTER OF MASS SCATTERING ANGLE (DEGREES)

FIGURE 45

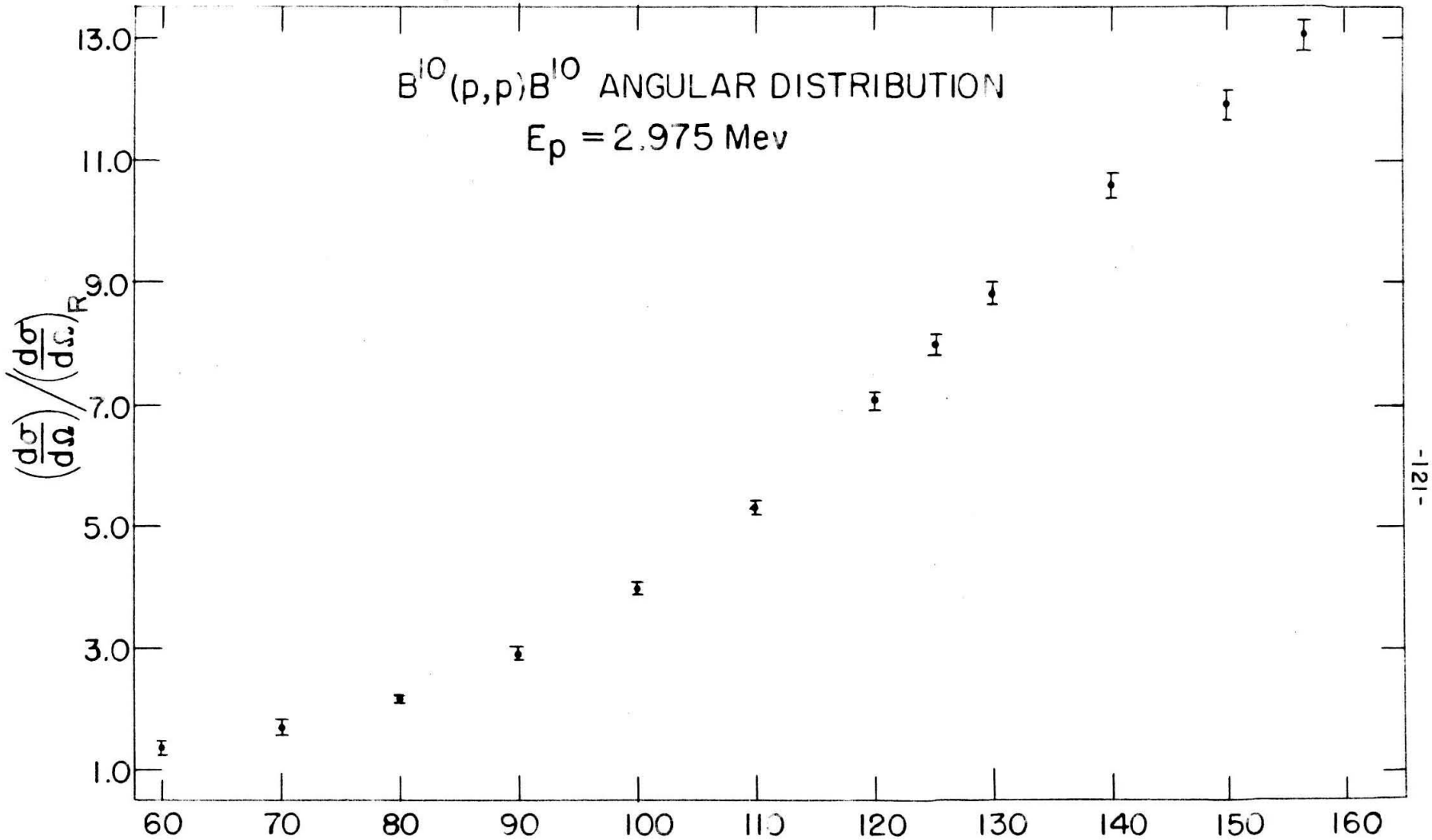
$B^{10}(p,p)B^{10}$ ANGULAR DISTRIBUTION
$E_p = 2.975$ Mev
$\left(\frac{d\sigma}{d\Omega}\right)/\left(\frac{d\sigma}{d\Omega}\right)_R$
13.0
11.0
9.0
7.0
5.0
3.0
1.0
60
70
80
90
100
110
120
130
140
150
160
CENTER OF MASS SCATTERING ANGLE (DEGREES)

FIGURE 46

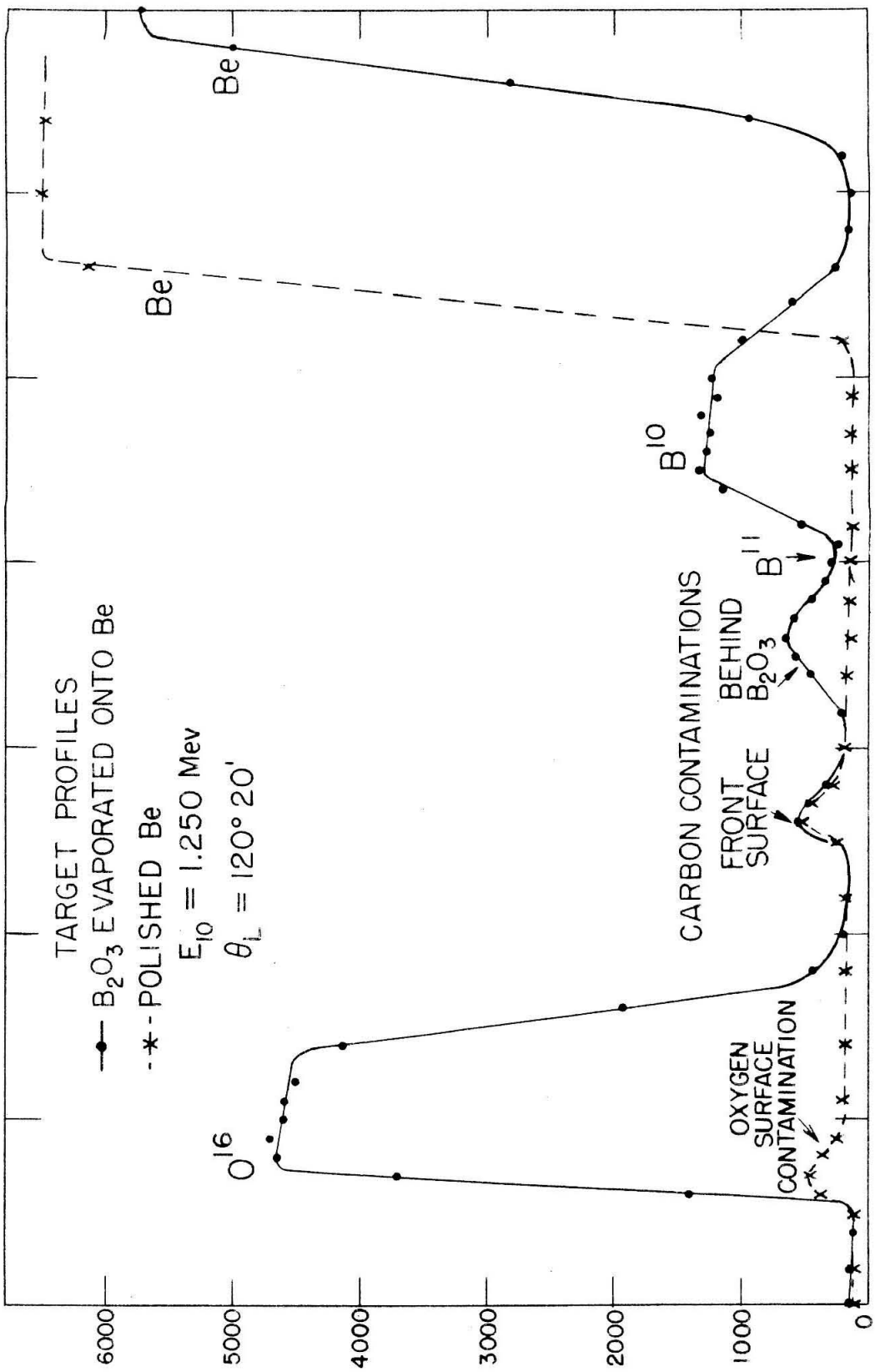
TARGET PROFILES
B_2O_3 EVAPORATED ONTO Be
-*- POLISHED Be
$E_{10} = 1.250$ Mev
$\theta_L = 120° 20'$
O^{16}
Be
Be
B^{10}
B^{11}
CARBON CONTAMINATIONS
FRONT SURFACE
BEHIND B_2O_3
OXYGEN SURFACE CONTAMINATION
COUNTS (ARBITRARY UNITS)
FLUXMETER SETTING (VOLTS)
0
1000
2000
3000
4000
5000
6000
0.61
0.62
0.63
0.64
0.65
0.66
0.67

FIGURE 47

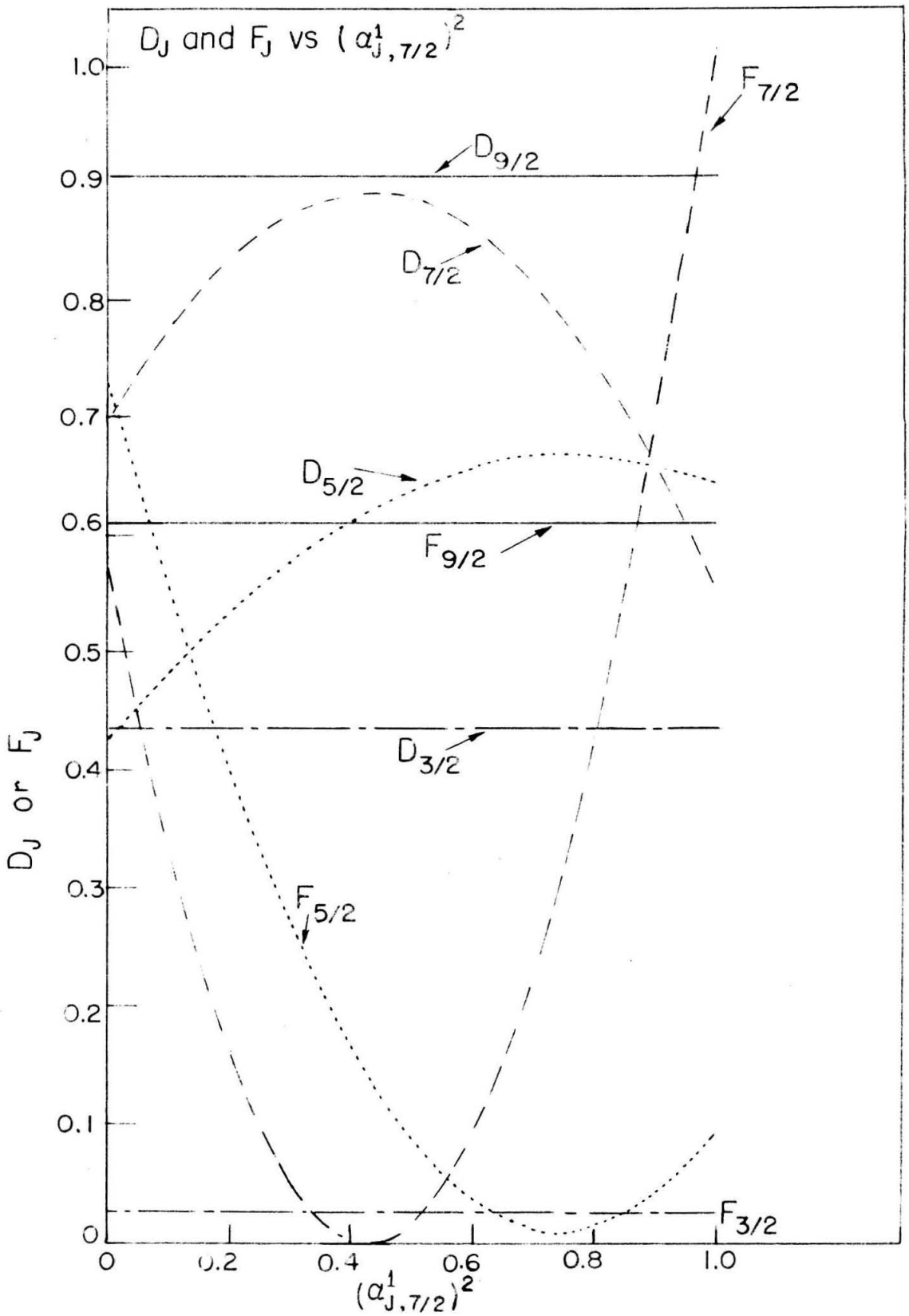
D_J and F_J vs $(\alpha^1_{J,7/2})^2$
$F_{7/2}$
$D_{9/2}$
$D_{7/2}$
$D_{5/2}$
$F_{9/2}$
$D_{3/2}$
$F_{5/2}$
$F_{3/2}$
D_J or F_J
1.0
0.9
0.8
0.7
0.6
0.5
0.4
0.3
0.2
0.1
0
0
0.2
0.4
0.6
0.8
1.0
$(\alpha^1_{J,7/2})^2$
CHANNEL SPIN MIXING PARAMETER

FIGURE 48

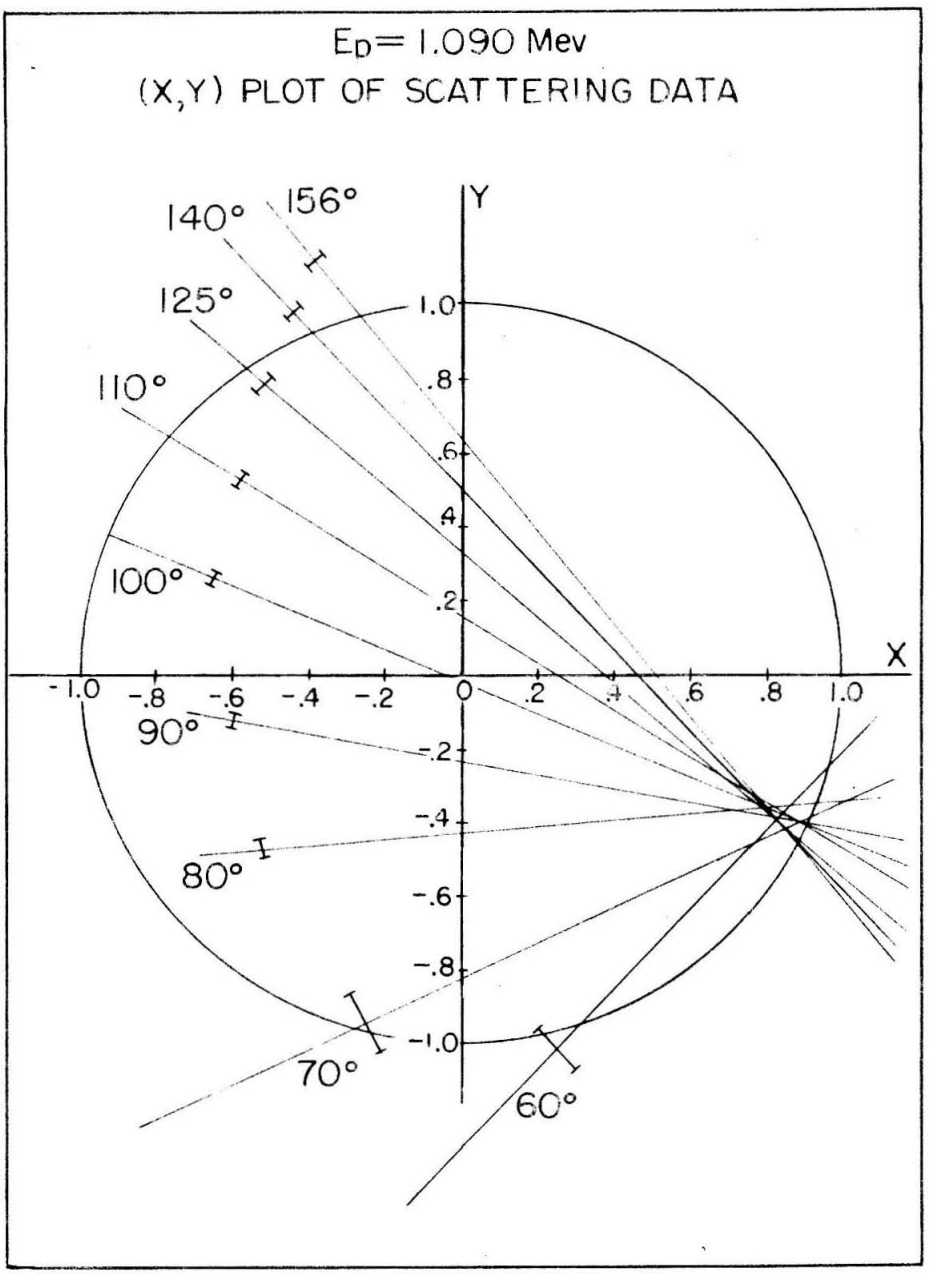
E_D= 1.090 Mev
(X,Y) PLOT OF SCATTERING DATA
140°
156°
125°
110°
100°
90°
80°
70°
60°
Y
X
1.0
.8
.6
.4
.2
-1.0
-.8
-.6
-.4
-.2
0
.2
.4
.6
.8
1.0
-.2
-.4
-.6
-.8
-1.0

FIGURE 49

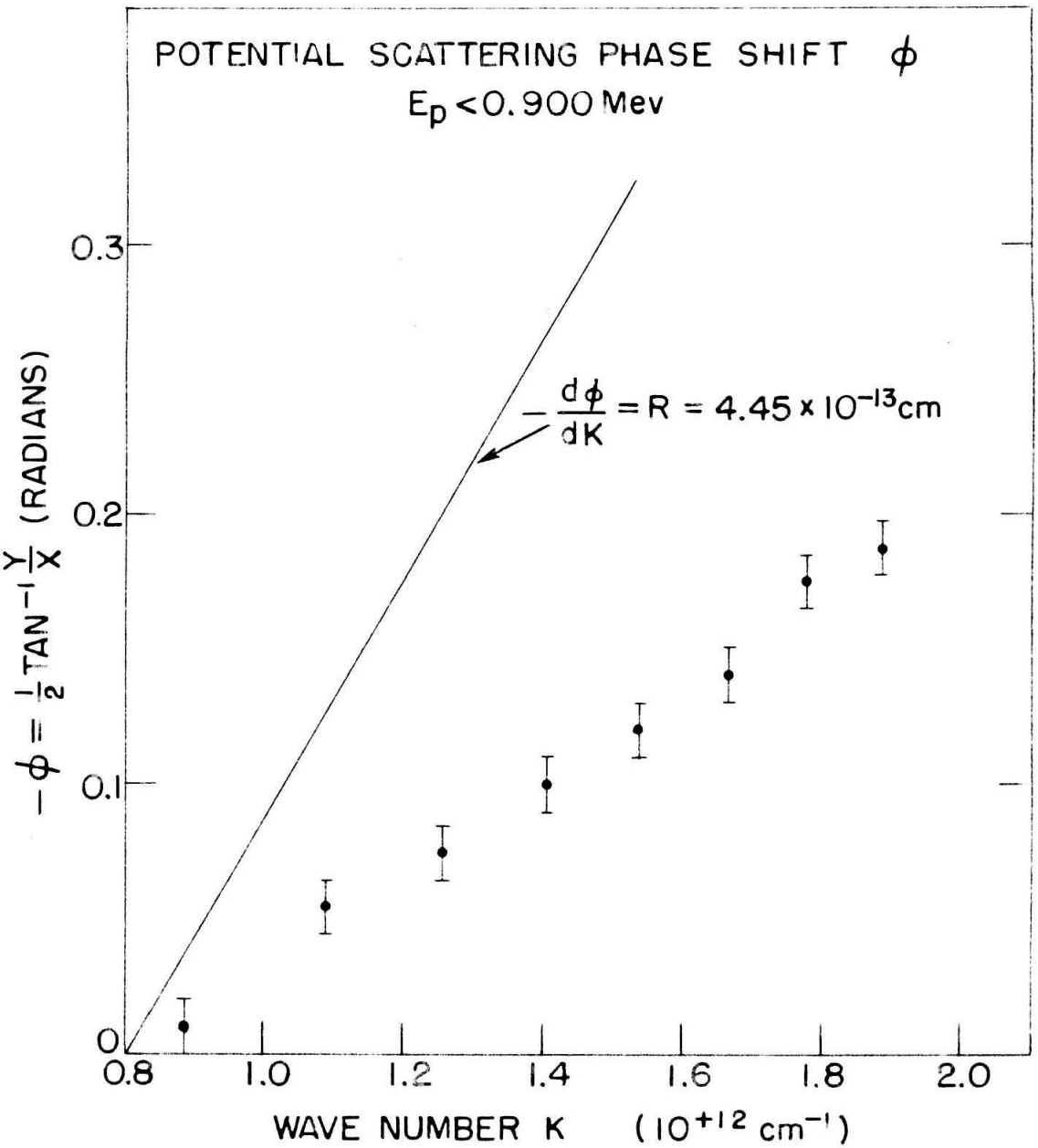
POTENTIAL SCATTERING PHASE SHIFT ϕ
$E_p < 0.900$ Mev
$-\frac{d\phi}{dK} = R = 4.45 \times 10^{-13}$cm
$-\phi = \frac{1}{2} TAN^{-1} \frac{Y}{X}$ (RADIANS)
0.3
0.2
0.1
0
0.8
1.0
1.2
1.4
1.6
1.8
2.0
WAVE NUMBER K (10^{+12} cm^{-1})

FIGURE 50

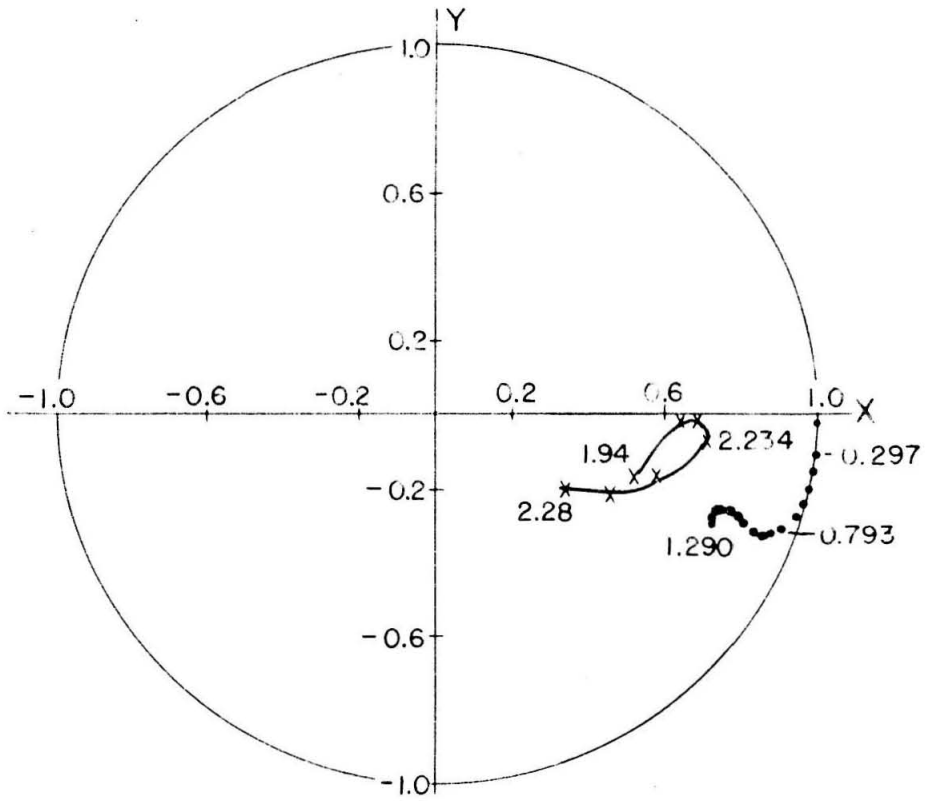

S-WAVE SCATTERING AMPLITUDES
Y vs X

- • $E_p < 1.290$ Mev
- x $1.935 \leq E_p \leq 2.280$ Mev

FIGURE 51

FIGURE 52

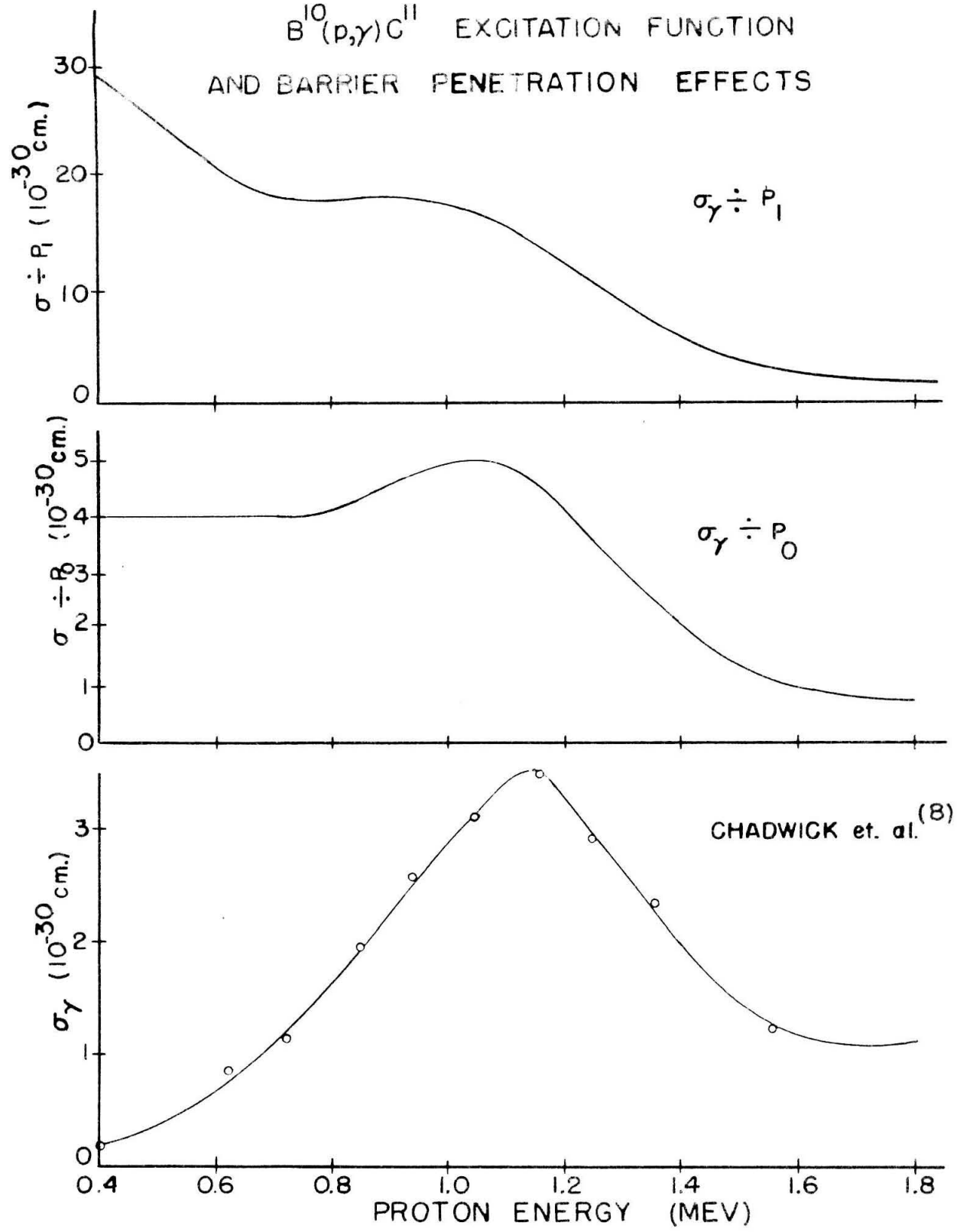
$B^{10}(p,\gamma)C^{11}$ EXCITATION FUNCTION
AND BARRIER PENETRATION EFFECTS
$\sigma \div P_1$ (10^{-30} cm.)
30
20
10
0
$\sigma_\gamma \div P_1$
$\sigma \div P_0$ (10^{-30} cm.)
5
4
3
2
1
0
$\sigma_\gamma \div P_0$
σ_γ (10^{-30} cm.)
3
2
1
0
CHADWICK et. al.(8)
0.4
0.6
0.8
1.0
1.2
1.4
1.6
1.8
PROTON ENERGY (MEV)